



1-1-2015

Dynamic Assessment of Cerebral Metabolic Rate of Oxygen (cmro2) With Magnetic Resonance Imaging

Zachary Bart Rodgers

University of Pennsylvania, zrodgers@mail.med.upenn.edu

Follow this and additional works at: <http://repository.upenn.edu/edissertations>

Recommended Citation

Rodgers, Zachary Bart, "Dynamic Assessment of Cerebral Metabolic Rate of Oxygen (cmro2) With Magnetic Resonance Imaging" (2015). *Publicly Accessible Penn Dissertations*. 1980.
<http://repository.upenn.edu/edissertations/1980>

This paper is posted at ScholarlyCommons. <http://repository.upenn.edu/edissertations/1980>
For more information, please contact libraryrepository@pobox.upenn.edu.

Dynamic Assessment of Cerebral Metabolic Rate of Oxygen (cmro2) With Magnetic Resonance Imaging

Abstract

The brain is almost entirely dependent on oxidative metabolism to meet its energy requirements. As such, the cerebral metabolic rate of oxygen (CMRO₂) is a direct measure of brain energy use. CMRO₂ provides insight into brain functional architecture and has demonstrated potential as a clinical tool for assessing many common neurological disorders.

Recent developments in magnetic resonance imaging (MRI)-based CMRO₂ quantification have shown promise in spatially resolving CMRO₂ in clinically feasible scan times. However, brain energy requirements are both spatially heterogeneous and temporally dynamic, responding to rapid changes in oxygen supply and demand in response to physiologic stimuli and neuronal activation.

Methods for dynamic quantification of CMRO₂ are lacking, and this dissertation aims to address this gap. Given the fundamental tradeoff between spatial and temporal resolution in MRI, we focus initially on the latter. Central to each proposed method is a model-based approach for deriving venous oxygen saturation (Y_v) – the critical parameter for CMRO₂ quantification – from MRI signal phase using susceptibility-based oximetry (SBO).

First, a three-second-temporal-resolution technique for whole-brain quantification of Y_v and CMRO₂ is presented. This OxFlow method is applied to measure a small but highly significant increase in CMRO₂ in response to volitional apnea.

Next, OxFlow is combined with a competing approach for Y_v quantification based on blood T₂ relaxometry (TRUST). The resulting interleaved-TRUST (iTRUST) pulse sequence greatly improves T₂-based CMRO₂ quantification, while allowing direct, simultaneous comparison of SBO- and T₂-based Y_v. iTRUST is applied to assess the CMRO₂ response to hypercapnia – a topic of great interest in functional neuroimaging – demonstrating significant biases between SBO- and T₂-derived Y_v and CMRO₂.

To address the need for dynamic and spatially resolved CMRO₂ quantification, we explore blood-oxygen-level-dependent (BOLD) calibration, introducing a new calibration model and hybrid pulse sequence combining OxFlow with standard BOLD/CBF measurement. Preliminary results suggest Ox-BOLD provides improved calibration “M-maps” for converting BOLD signal to CMRO₂.

Finally, OxFlow is applied clinically to patients with obstructive sleep apnea (OSA). A small clinical pilot study demonstrates OSA-associated reductions in CMRO₂ at baseline and in response to apnea, highlighting the potential utility of dynamic CMRO₂ quantification in assessing neuropathology.

Degree Type

Dissertation

Degree Name

Doctor of Philosophy (PhD)

Graduate Group
Bioengineering

First Advisor
Felix W. Wehrli

Keywords
cerebral blood flow, cerebral metabolism, CMRO₂, magnetic resonance imaging, obstructive sleep apnea, oximetry

**DYNAMIC ASSESSMENT OF CEREBRAL METABOLIC RATE OF OXYGEN (CMRO₂)
WITH MAGNETIC RESONANCE IMAGING**

Zachary B. Rodgers

A DISSERTATION

in

Bioengineering

Presented to the Faculties of the University of Pennsylvania in

Partial Fulfillment of the Requirements for the

Degree of Doctor of Philosophy

2015

Supervisor of Dissertation

Felix W. Wehrli, Ph.D.

Professor of Radiology

Graduate Group Chairperson

Jason A. Burdick, Ph.D.

Professor of Bioengineering

Dissertation Committee

Peter F. Davies, Ph.D., Professor of Pathology and Laboratory Medicine (Chair)

Victor A. Ferrari, M.D. Professor of Medicine

Ravinder Reddy, Ph.D., Professor of Radiology

Hee Kwon Song, Ph.D., Associate Professor of Radiology

**DYNAMIC ASSESSMENT OF CEREBRAL METABOLIC RATE OF OXYGEN (CMRO₂)
WITH MAGNETIC RESONANCE IMAGING**

COPYRIGHT

2015

Zachary B. Rodgers

Dedicated to my family:
past, present, and future.

ACKNOWLEDGEMENTS

It is said that the only decision more important than choosing your PhD advisor is choosing your spouse. In our five-year union, my advisor, Dr. Felix Wehrli, has given me a model for the type of scientist I wish to become: at all times brilliant and curious while unceasingly patient and supportive, setting a high bar for all those around him.

I owe thanks to many members of the Wehrli lab for their help and support: to Michael Langham for teaching me about MRI when I knew nothing and for continuing to be an invaluable source of scientific discussion and inspiration along the way, to Erin Englund for her collaboration, friendship, and hundreds of cups of coffee, to Cheng Li for his astonishing patience and selflessness in sharing his enormous knowledge, and to Alan Seifert for always being one step ahead and reporting back from the other side.

Thank you to the many other wonderful and smart people I have had the pleasure of working with: Varsha Jain, Jeremy Magland, Richard Schwab, Sarah Leinwand, John Detre, Yulin Ge, Suliman Barhoum, Yongxia Zhou, Maria Fernández-Seara, and many others. And a special thanks to Holly Flachs and Kelly Sexton, for making me laugh and keeping everything running smoothly.

I also thank my dissertation committee, Peter Davies, Ravinder Reddy, Hee Kwon Song, and Victor Ferrari, for their guidance and support. Thank you to the HHMI Interfaces Program and the Medical Scientist Training Program, especially Dr. Ann Tiao and Maggie Krall, for your guardianship and advocacy.

Of course, nothing would be possible without the love, support, and encouragement of my parents, Debbie and Bill. And finally, thank you to my fiancée and best friend, Archana. You keep me looking forward to each day, knowing that the best is yet to come.

ABSTRACT

DYNAMIC ASSESSMENT OF CEREBRAL METABOLIC RATE OF OXYGEN (CMRO₂) WITH MAGNETIC RESONANCE IMAGING

Zachary B. Rodgers

Felix W. Wehrli, Ph.D.

The brain is almost entirely dependent on oxidative metabolism to meet its energy requirements. As such, the cerebral metabolic rate of oxygen (CMRO₂) is a direct measure of brain energy use. CMRO₂ provides insight into brain functional architecture and has demonstrated potential as a clinical tool for assessing many common neurological disorders.

Recent developments in magnetic resonance imaging (MRI)-based CMRO₂ quantification have shown promise in spatially resolving CMRO₂ in clinically feasible scan times. However, brain energy requirements are both spatially heterogeneous and temporally dynamic, responding to rapid changes in oxygen supply and demand in response to physiologic stimuli and neuronal activation.

Methods for dynamic quantification of CMRO₂ are lacking, and this dissertation aims to address this gap. Given the fundamental tradeoff between spatial and temporal resolution in MRI, we focus initially on the latter. Central to each proposed method is a model-based approach for deriving venous oxygen saturation (Y_v) – the critical parameter for CMRO₂ quantification – from MRI signal phase using susceptibility-based oximetry (SBO).

First, a three-second-temporal-resolution technique for whole-brain quantification of Y_v and CMRO₂ is presented. This OxFlow method is applied to measure a small but highly significant increase in CMRO₂ in response to volitional apnea.

Next, OxFlow is combined with a competing approach for Y_v quantification based on blood T_2 relaxometry (TRUST). The resulting interleaved-TRUST (iTRUST) pulse sequence greatly

improves T_2 -based $CMRO_2$ quantification, while allowing direct, simultaneous comparison of SBO- and T_2 -based Y_v . iTRUST is applied to assess the $CMRO_2$ response to hypercapnia – a topic of great interest in functional neuroimaging – demonstrating significant biases between SBO- and T_2 -derived Y_v and $CMRO_2$.

To address the need for dynamic and spatially resolved $CMRO_2$ quantification, we explore blood-oxygen-level-dependent (BOLD) calibration, introducing a new calibration model and hybrid pulse sequence combining OxFlow with standard BOLD/CBF measurement. Preliminary results suggest Ox-BOLD provides improved calibration “M-maps” for converting BOLD signal to $CMRO_2$.

Finally, OxFlow is applied clinically to patients with obstructive sleep apnea (OSA). A small clinical pilot study demonstrates OSA-associated reductions in $CMRO_2$ at baseline and in response to apnea, highlighting the potential utility of dynamic $CMRO_2$ quantification in assessing neuropathology.

TABLE OF CONTENTS

ACKNOWLEDGEMENTS.....	iv
ABSTRACT	v
TABLE OF CONTENTS	vii
LIST OF TABLES	x
LIST OF FIGURES	xi
LIST OF ABBREVIATIONS.....	xiii
PREFACE	xv
 Chapter 1: Introduction.....	 1
1.1. Cerebral Metabolism.....	1
1.1.1. The Unique Energy Requirements of the Brain	1
1.1.2. A Brief History of Measuring Brain Activity.....	2
1.1.3. Why Quantify CMRO ₂ ?	5
1.1.3.1. <i>Limitations of BOLD fMRI</i>	5
1.1.3.2. <i>Potential Clinical Applications of CMRO₂ Measurement</i>	6
1.2. CMRO₂ Quantification.....	7
1.2.1. Overview of Brain Oxygen Delivery and Consumption	7
1.2.2. Fick Principle for CMRO ₂ Quantification	9
1.2.3. Non-MR-Based Methods.....	10
1.2.3.1. <i>Optical Methods</i>	10
1.2.3.2. <i>PET</i>	11
1.2.4. MR-Based Methods	12
1.2.4.1. <i>MRI Contrast and CMRO₂</i>	12
1.2.4.2. <i>Extravascular T₂*-Based Methods (Calibrated BOLD)</i>	14
1.2.4.3. <i>Extravascular T₂'-Based Methods (qBOLD)</i>	19
1.2.4.4. <i>Intravascular T₂-Based Methods</i>	22
1.2.4.5. <i>Intravascular Susceptibility-Based Methods</i>	25
1.2.4.6. <i>Dynamic Quantification of CMRO₂</i>	30
1.3. Outline of Dissertation Chapters.....	30
 Chapter 2: High Temporal Resolution Quantification of Global Cerebral Metabolic Rate of Oxygen Consumption in Response to Apneic Challenge	 32
2.1. Abstract.....	32
2.2. Introduction	32
2.3. Methods	35
2.3.1. CMRO ₂ Quantification via the Fick Principle.....	35
2.3.2. Principles of Susceptometry-Based Global CMRO ₂ Quantification	36
2.3.3. Combination of SBO and PC-MRI for CMRO ₂ Quantification (OxFlow)	38
2.3.4. Pulse Sequence Modifications for Improved Temporal Resolution.....	39
2.3.5. In Vivo Magnetic Resonance Imaging Studies.....	41
2.3.5.1. <i>Validation of Critical Methodological Assumptions</i>	42
2.3.5.2. <i>Quantification of CMRO₂ in Response to Apneic Challenge</i>	42
2.3.6. Data Processing.....	43
2.4. Results	45
2.5. Discussion	50

2.6. Conclusions.....	54
2.7. Appendix: Non-Steady-State Application of the Fick Principle.....	54
Chapter 3: Rapid T₂- and Susceptometry-Based CMRO₂ Quantification with Interleaved TRUST (iTRUST)	56
3.1. Abstract.....	56
3.2. Introduction	57
3.3. Theory	61
3.3.1. Susceptometry-Based Quantification of Y _v (SBO)	61
3.3.2. Combination of SBO and PC-MRI for CMRO ₂ Quantification (OxFlow)	62
3.3.3. TRUST and Interleaved TRUST (iTRUST)	63
3.4. Methods	65
3.4.1. Human Subject Protocols.....	65
3.4.2. Validation Study	66
3.4.3. Simulations.....	67
3.4.4. Apnea Study.....	67
3.4.5. Hypercapnia Study.....	68
3.4.6. Image Analysis	68
3.5. Results	70
3.6. Discussion	76
3.6.1. Validation of iTRUST.....	76
3.6.2. T ₂ -Based CMRO ₂ Temporal Resolution	77
3.6.3. Hypercapnia Study.....	78
3.6.4. Applications of iTRUST	80
3.7. Conclusions.....	81
3.8. Appendix: Analysis of Flow-Dependent Error in SBO.....	82
Chapter 4: BOLD Calibration with Interleaved Susceptometry-Based Oximetry and Phase-Contrast Flow Quantification.....	84
4.1. Abstract.....	84
4.2. Introduction	84
4.3. Methods	88
4.3.1. Y _v -Based Model	88
4.3.2. Ox-BOLD Pulse Sequence	90
4.3.3. In Vivo Imaging Experiments	93
4.3.3.1. <i>Single-Slice Ox-BOLD Validation</i>	93
4.3.3.2. <i>Gas-Mixture Breathing Experiments</i>	93
4.3.4. Data Analysis	94
4.4. Results	95
4.4.1. Interleaved Sequence Assessment.....	95
4.4.2. Single-Slice Ox-BOLD M-Quantification	95
4.4.3. Multi-Slice Ox-BOLD M-Quantification.....	96
4.5. Discussion	99
4.5.1. Prior Applications of Y _v to BOLD Calibration.....	100
4.5.2. Assessment of Calibration Results	100
4.5.3. Y _v -Based Model Assumptions	101
4.6. Conclusions.....	103

Chapter 5: Cerebral Metabolic Rate of Oxygen in Obstructive Sleep Apnea at Rest and In Response to Breath-Hold Challenge.....	104
5.1. Abstract.....	104
5.2. Introduction	104
5.3. Methods	107
5.3.1. Susceptometry-Based Quantification of Y_v (SBO)	107
5.3.2. Combination of SBO and PC-MRI for $CMRO_2$ Quantification (OxFlow)	108
5.3.3. Subjects	110
5.3.4. Experimental Procedures	111
5.3.4.1. Volitional Apnea Paradigm	111
5.3.4.2. MR Imaging Protocol.....	112
5.3.5. Data Processing	113
5.3.6. Statistical Analysis	114
5.4. Results	115
5.4.1. Subject Demographic and Polysomnography Group Characteristics	115
5.4.2. Baseline Differences Between OSA Subjects and Controls	115
5.4.3. Apneic Response in OSA Subjects and Controls	118
5.4.4. Relationship Between $CMRO_2$ and AHI	118
5.4.5. Age and BMI Effects Analysis	119
5.5. Discussion	120
5.5.1. Interpretation of Apnea Paradigm Data.....	120
5.5.2. Study Limitations and Future Directions	122
5.6. Conclusions.....	125
Chapter 6: Conclusions and Future Directions	126
6.1. Conclusions.....	126
6.2. Future Directions	128
6.2.1. OxFlow Technical Improvements	128
6.2.2. Technical Investigations	128
6.2.3. Clinical Investigations.....	129
BIBLIOGRAPHY.....	131

LIST OF TABLES

Table 1.1: MR-based \dot{V}_V/CMRO_2 quantification methods and their respective features	14
Table 2.1: Individual subject and group values for various extracted parameters at rest and in response to volitional apnea	48
Table 3.1: Hypercapnia paradigm parameter values derived from pulse oximetry, capnography, and iTRUST MRI in 10 subjects.....	76
Table 4.1: Whole-brain-averaged parameter values from hypercapnia and hyperoxia M-calibration experiments	98
Table 5.1: Group demographic and polysomnography data	111
Table 5.2: Summary of baseline and apneic response parameters in OSA subjects and controls	118

LIST OF FIGURES

Figure 1.1: Early demonstration of uncoupling between blood flow and CMRO_2 upon neuronal activation by PET imaging	3
Figure 1.2: Early demonstration of the BOLD effect in humans.....	4
Figure 1.3: Hemoglobin dissociation curve illustrating the relationship between oxygen partial pressure and percent hemoglobin oxygen saturation	8
Figure 1.4: Schematic illustration of brain oxygen extraction in the capillaries	9
Figure 1.5: Schematic diagram illustrating the various physiologic contributions relating neuronal activity to BOLD signal	15
Figure 1.6: Schematic diagram illustrating how vessel size and diffusion distance determine diffusion dephasing versus static dephasing effects.....	20
Figure 1.7: Calibration curve relating Y_v to measured T_2 and Hct for $t_{\text{CPMG}}=10$ ms	23
Figure 1.8: Illustration of a blood vessel approximated by the infinite cylinder model	28
Figure 2.1: High temporal resolution CMRO_2 quantification pulse sequence	39
Figure 2.2: SSSBF:tCBF ratio determination in three subjects	45
Figure 2.3: Error due to Keyhole reconstruction	46
Figure 2.4: Apnea paradigm representative subject images and time course data	47
Figure 2.5: Apnea paradigm cohort time course data	49
Figure 3.1: TRUST vs. SBO-derived Y_v in 10 healthy subjects at rest.....	60
Figure 3.2: BRISK vs. Keyhole Cartesian view-sharing	62
Figure 3.3: iTRUST pulse sequence and example images.....	65
Figure 3.4: TRUST, OxFlow, and iTRUST parameter values acquired sequentially for four minutes each in three resting subjects.....	70
Figure 3.5: Scatter plot of iTRUST Y_v - T_2 values fitted using all four (0, 40, 80, and 160 ms) vs. only two (0 and 80 ms) eTEs from the same data	71

Figure 3.6: Simulation of expected Y_v - T_2 error vs. the number of eTEs used for T_2 fitting	72
Figure 3.7: iTRUST parameter values in response to a 60-second breath-hold in a single subject	73
Figure 3.8: Subject-averaged time-course plots of physiologic parameters measured via pulse oximetry (Y_a , HR) and capnography (EtCO ₂ , RR).....	74
Figure 3.9: iTRUST-derived parameter values in response to five minutes of 5% CO ₂ gas-mixture breathing	75
Figure 4.1: Schematic diagram comparing the traditional calibration models to the Y_v -based calibration model.....	90
Figure 4.2: Single-slice Ox-BOLD pulse sequence diagram.....	91
Figure 4.3: Multi-slice Ox-BOLD pulse sequence diagram	92
Figure 4.4: Single-slice Ox-BOLD data from an example subject.....	96
Figure 4.5: Multi-slice Ox-BOLD data from an example subject	97
Figure 4.6: Zoomed-in parametric M-maps from the various calibration methods.....	98
Figure 4.7: M-value histograms for each calibration method	99
Figure 5.1: MRI pulse sequences for rapid quantification of global CMRO ₂	109
Figure 5.2: MRI protocol for quantifying CMRO ₂ at rest and in response to apnea	112
Figure 5.3: Apnea paradigm data in a representative OSA subject (male, 63 years old)	116
Figure 5.4: Group-averaged apnea paradigm data in OSA subjects and controls	117
Figure 5.5: Relationship between CMRO ₂ and AHI	119

LIST OF ABBREVIATIONS

%HbO ₂	percent hemoglobin oxygen saturation
ASL	arterial spin labeling
ATP	adenosine triphosphate
AVO ₂ D	arteriovenous oxygen difference
BMI	body mass index
BOLD	blood-oxygen-level-dependent
C _a	arterial oxygen content
CBF	cerebral blood flow
CBV	cerebral blood volume
CBV _a	arterial cerebral blood volume
CBV _v	venous cerebral blood volume
CMRO ₂	cerebral metabolic rate of oxygen
CPAP	continuous positive airways pressure
CPMG	Carr-Purcell-Meiboom-Gill
CSF	cerebrospinal fluid
CVR	cerebrovascular reactivity
dHb	deoxygenated hemoglobin
EEG	electroencephalography
EPI	echo-planar imaging
EtCO ₂	end-tidal carbon dioxide
eTE	effective echo time
EtO ₂	end-tidal oxygen
fMRI	functional magnetic resonance imaging
GRE	gradient-recalled echo
Hb	hemoglobin
Hct	hematocrit
HR	heart rate
iTRUST	interleaved T ₂ -relaxation-under-spin-tagging
MR	magnetic resonance
MRI	magnetic resonance imaging
NIRS	near-infrared spectroscopy
NMR	nuclear magnetic resonance
OEF	oxygen extraction fraction
oHb	oxygenated hemoglobin
OSA	obstructive sleep apnea
PC-MRI	phase-contrast magnetic resonance imaging
pCASL	pseudo-continuous arterial spin labeling
PET	positron emission tomography
piO ₂	interstitial partial pressure of oxygen
PLD	post-label delay
pO ₂	partial pressure of oxygen
QSM	quantitative susceptibility mapping
RF	radiofrequency
ROI	region of interest
RR	respiratory rate

SBO	susceptometry-based oximetry
SDR	static dephasing regime
SNR	signal-to-noise ratio
RMSE	root-mean-square error
SSS	superior sagittal sinus
SSSBF	superior sagittal sinus blood flow
tCBF	total cerebral blood flow
TE	echo time
TRUST	T ₂ -relaxation-under-spin-tagging
Y _a	arterial oxygen saturation
Y _v	venous oxygen saturation

PREFACE

Chapter 2 has been published as: Rodgers ZB, Jain V, Englund EK, Langham MC, and Wehrli FW. High temporal resolution MRI quantification of global cerebral metabolic rate of oxygen consumption in response to apneic challenge. JCBFM, 2013;33(10):1514-1522. DOI: 10.1038/jcbfm.2013.110.

Chapter 3 has been published as: Rodgers ZB, Englund EK, Langham MC, Magland JF, and Wehrli FW. Rapid T_2 - and susceptometry-based $CMRO_2$ quantification with interleaved TRUST (iTRUST). Neuroimage, 2015;106:441-450. DOI: 10.1016/j.neuroimage.2014.10.061.

Chapter 4 has been published as: Rodgers ZB, Englund EK, Fernández-Seara MA, and Wehrli FW. BOLD calibration with interleaved susceptometry-based oximetry. Proceedings of the 23rd Annual Meeting of ISMRM, Toronto, Canada, p. 597.

Chapter 5 has been accepted for publication in the Journal of Cerebral Blood Flow and Metabolism as: Rodgers ZB, Leinwand SE, Keenan BT, Kini LG, Schwab RJ, and Wehrli FW. Cerebral metabolic rate of oxygen ($CMRO_2$) in obstructive sleep apnea at rest and in response to breath-hold challenge.

Zachary B. Rodgers

July 28, 2015

Chapter 1: Introduction

1.1. Cerebral Metabolism

The mechanism through which the brain converts energetic substrates into thoughts and actions is one of the central questions in human biology. This section discusses the unique energy requirements of the brain, the early efforts to visualize brain energy use, and the motivations for quantifying the cerebral metabolic rate of oxygen (CMRO₂).

1.1.1. The Unique Energy Requirements of the Brain

Among human organs, the brain is distinct in its requirement for a large, uniform, and uninterrupted supply of oxygen. Although comprising only 2% of total body mass, the brain accounts for approximately 20% of the body's total oxygen consumption (1). Furthermore, the brain is almost entirely dependent on oxidative metabolism of glucose to meet its energy requirements, and is therefore especially susceptible to hypoxia and ischemia. If circulation to the brain is stopped, such as following cardiac arrest, loss of consciousness occurs in seconds, and brain tissue is irreversibly damaged in as little as three minutes (2).

Since the brain is almost entirely dependent on oxygen to meet its energy needs, CMRO₂ provides a direct, quantitative measure of the brain energy requirements, and an important marker of tissue viability and function. While the precise cellular mechanisms relating neuronal signaling and cerebral metabolism are still an area of active investigation, it is known that approximately 80% of cerebral metabolism at rest is devoted to active signaling processes, i.e., the propagation of action potentials and the restoration of those potentials after neurotransmission (3). Recent observation that these resting-state signals are spatiotemporally correlated across distinct brain regions – the so-called “default mode network” (4) – has heightened interest in understanding the relationship between neuronal signaling and cerebral metabolism.

Because CMRO_2 is remarkably well conserved in normal physiology, there is much interest in understanding physiologic and pathologic states in which CMRO_2 is affected. Although, alterations in CMRO_2 have been suggested in several common neurologic disorders, these changes are relatively small given the critical importance of oxygen in maintaining tissue viability. Furthermore, while cerebral metabolism is increased in response to mental and motor activity, these changes tend to be highly localized, informing on the structural and functional organization of the brain, but at the same time making measurement of these metabolic changes challenging. For these reasons, developing methods for quantification and imaging of brain activity and metabolism remains a major goal and challenge of neuroscience research.

1.1.2. A Brief History of Measuring Brain Activity

One of the major challenges in studying brain function is that the brain is relatively inaccessible to direct measurement. The electrical signals produced by the discharge of neuronal action potentials provide perhaps the closest measure of brain activity. These signals were first observed by Richard Caton in 1875, using galvanometric measurements in animals during chewing and visual stimulation (5). This work was expanded to humans with the invention of the electroencephalography (EEG) by Hans Berger in 1929 (6), which allowed non-invasive measurement of brain electrical activity through the scalp. Unfortunately, EEG and magnetoencephalography (7) – a complementary technique based on measurement of magnetic fields – have very limited sensitivity, spatial resolution, and penetration. However, these electrical changes are also associated with changes in blood flow and metabolism, providing alternative means of assessing brain activity and function.

Despite producing relatively small changes in brain oxygen metabolism, motor and mental processes are associated with large changes in cerebral blood flow (CBF). In fact, these CBF changes are large enough to be observed by the naked eye, as demonstrated in 1881 by Italian physiologist Angelo Mosso, who observed increased regional pulsations in the brains of patients performing mental tasks while undergoing neurosurgery (8). In 1890, Charles Roy and Charles

Sherrington hypothesized that such CBF responses were related to increases in metabolic demand (9). However, quantitative methods for testing such hypotheses did not yet exist.

A major breakthrough came in 1945, when Seymour Kety and Carl Schmidt introduced the first method for quantifying CBF and CMRO_2 in humans based on the Fick Principle (10-12). In the 1950s through 1970s, Kety and his student, Louis Sokoloff, led the development of autoradiographic methods to create quantitative images of CBF and CMRO_2 in animals (13). The advent of positron emission tomography (PET) allowed extension of this autoradiographic work to humans, where it was used to detect regional activations associated with specific mental functions, for example, language processing (14). Seminal work by Peter Fox and Marcus Raichle (15,16) demonstrated that upon neuronal activation, local CBF increases in excess of CMRO_2 (Figure 1.1).

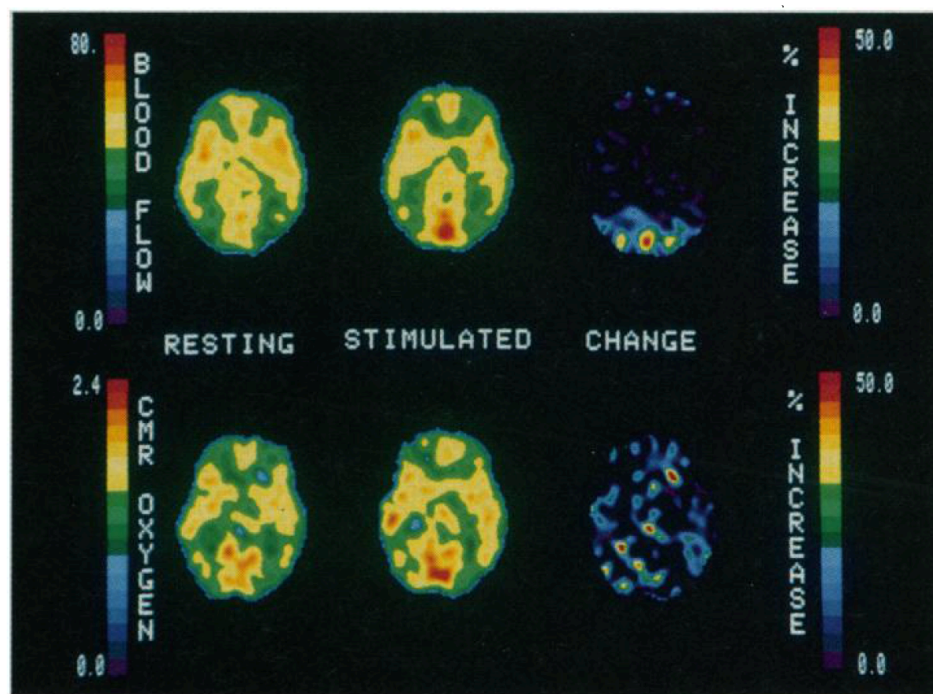


Figure 1.1: Early demonstration of uncoupling between blood flow and CMRO_2 upon neuronal activation by PET imaging. Despite a large increase in occipital blood flow, corresponding CMRO_2 changes are below the level of detection. This mismatch between flow and metabolism provides the basis for the BOLD fMRI technique. Figure adapted from (15).

This mismatch provides the foundation for the blood-oxygen-level-dependent (BOLD) functional magnetic resonance imaging (fMRI) method, which allows observation of brain activity based on MRI-measured changes in local blood oxygenation. The BOLD fMRI effect was first observed by Seiji Ogawa in rats in 1990 (17) and subsequently demonstrated in humans by Ogawa (18) (**Figure 1.2**) and several other groups (19-21).

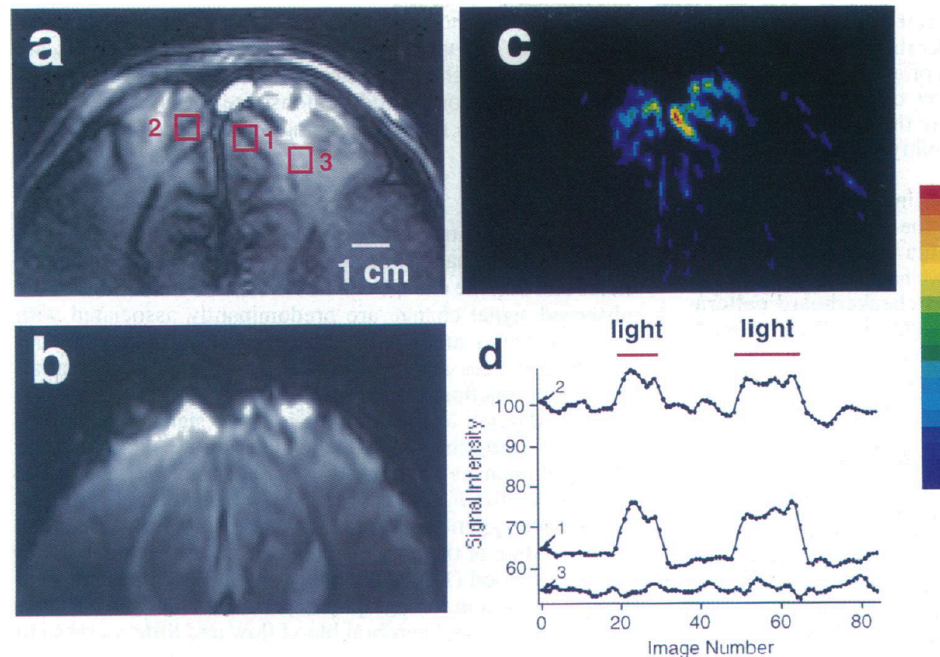


Figure 1.2: Early demonstration of the BOLD effect in humans. (A) T_1 -weighted axial image with several regions of interest (ROIs) indicated by square boxes; (B) T_2^* -weighted BOLD image at the same slice location; (C) Pseudocolor map of BOLD image intensity changes in response to visual stimulation and (D) corresponding time-course plots of signal intensities from ROIs in (A), indicating restriction of BOLD effect to ROIs (1 and 2) in the visual cortex. Figure from (18).

Unlike PET-based metabolic imaging, BOLD fMRI does not require injection of radioactive tracers, can be performed on standard clinical imaging systems, and provides higher spatial and temporal resolution. In the past 20 years, use of BOLD fMRI has grown exponentially and provided enormous insights into the spatiotemporal functional organization of the brain.

1.1.3. Why Quantify CMRO₂?

1.1.3.1. Limitations of BOLD fMRI

Though the contribution of BOLD fMRI to basic neuroscience cannot be overstated, the technique has fundamental limitations. The relative simplicity of the technique belies the enormous complexity of interpreting the underlying physiologic meaning of BOLD data.

BOLD signal changes are predominantly vascular in origin, driven by changes in CBF and cerebral blood volume (CBV) more so than metabolism. The relationship between BOLD signal and its vascular and metabolic determinants is a complex one, modified by a number of physiologic and external factors. Therefore, BOLD signal must always be quantified in terms of changes relative to a baseline state; it cannot be used to quantify baseline cerebral metabolism. These relative BOLD signal changes can vary significantly within (22) and across (23) subjects, reducing power to detect group differences. Group comparisons can also be confounded by vascular effects unrelated to metabolic differences, for instance, in studies of aging (24,25).

As a measure of brain activity, CMRO₂ has several theoretical advantages compared to BOLD fMRI signal. Unlike BOLD, CMRO₂ can be measured in absolute physiologic units, and may provide more power to detect group differences in longitudinal and clinical studies. Although simultaneous fMRI and intracortical EEG in animals has shown BOLD signal changes to correlate with underlying neuronal activity (26), BOLD signal onset latency is an order of magnitude greater compared to underlying electrical signals (27). Furthermore, BOLD signal originates from the post-capillary venous vasculature, which may be far from the site of activation (28). In contrast, the CMRO₂ response is expected to exhibit closer spatiotemporal correlation with neuronal activation. CMRO₂ imaging would thus provide a more precise and accurate tool for studying the temporal dynamics of neurologic function and spatial organization of brain functional systems.

1.1.3.2. Potential Clinical Applications of CMRO₂ Measurement

CMRO₂ measurement and mapping could be of significant benefit to the diagnosis and management of many common neurologic diseases. PET is the current gold standard for metabolic brain imaging; however, its cost, complexity, and invasiveness significantly limit its application. Compared to PET, MRI is inexpensive, non-invasive, and relatively ubiquitous in modern hospitals. Potential clinical applications of MR-based CMRO₂ quantification include the study of stroke, brain tumors, Alzheimer's disease (AD), and obstructive sleep apnea (OSA).

In stroke, blood flow and oxygen delivery are regionally compromised. While some tissue is irreversibly damaged, surrounding tissue in the "ischemic penumbra" region is potentially salvageable. Identifying this tissue is critical to decision making in acute stroke management, as administration of tissue plasminogen activator, a clot-dissolving agent, carries a high risk of acute bleeding. It is believed that imaging of CMRO₂ and oxygen extraction fraction (OEF), the fraction of total delivered oxygen extracted from the blood, may provide a better measure of tissue viability than existing MRI methods based on diffusion/perfusion mismatch (29,30).

It has long been known that tumors exhibit hypoxia due to preferential use of anaerobic glycolysis even in the presence of sufficient oxygen, an observation known as the Warburg effect (31). Thus, hypoxia provides a biomarker of tumor presence, and the degree of hypoxia may provide a prognostic and diagnostic measure for decision making in cancer management (32). MR-based CMRO₂ mapping could provide a more direct and less invasive means of assessing tumor hypoxia than the current method of fluorodeoxyglucose (FDG) PET.

Though the etiology of AD pathology has long been ascribed to the deposition of beta amyloid plaques and neurofibrillary tangles, recent studies suggest vascular dysfunction plays a significant role in the development of AD and other dementias (33). AD has been associated with regional reductions in CMRO₂ with preserved blood flow using PET (34), as well as reduced global cerebrovascular reactivity (CVR) in response to breath-hold measured with Doppler ultrasound (35). Magnetic resonance (MR)-based methods have been widely used in studying

structural changes in AD, and CMRO₂ methodology would add an important functional component to these studies.

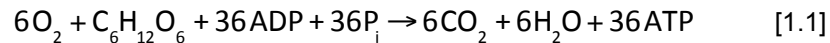
Although OSA is defined by structural and functional failure of the upper airway to maintain patency during sleep, it is also associated with extensive neurologic comorbidities of poorly understood etiology. OSA has been associated with gray matter loss in regions associated with ischemic sensitivity, such as the hippocampus (36). Detection of impaired CVR in OSA (37-39), suggests that blunting of the normal apneic cerebrovascular response may allow hypoxic damage to occur during OSA-associated nocturnal apneas. Preliminary data suggests that OSA is also associated with changes in CMRO₂, both at rest and dynamically in response to breath-hold challenge (40).

1.2. CMRO₂ Quantification

This section outlines the physiology of brain oxygen delivery and consumption – the basis for quantifying CMRO₂. Current methods for CMRO₂ quantification are discussed and compared, with particular focus on the various MR-based methods and their respective tradeoffs between spatial and temporal resolution.

1.2.1. Overview of Brain Oxygen Delivery and Consumption

In aerobic metabolism, oxygen acts as the final electron acceptor of the electron transport chain, driving the formation of adenosine triphosphate (ATP), the main energy substrate in the body:



Oxidative phosphorylation of glucose (and additionally ketone bodies during starvation) is the sole mechanism through which the brain can produce ATP for any appreciable amount of time. While nonoxidative glucose consumption (glycolysis) plays an important role in providing rapid energy during functional activation (15,41), it is considerably less efficient than aerobic metabolism, producing only 2 ATP molecules per glucose molecule compared to 36 ATP. Thus, it is believed

that increased energy demand during even transient brain activation states is met largely through oxidative metabolism (42).

Oxygen is not produced endogenously and must be continuously transported to the brain via the blood. This is achieved by passive diffusion of oxygen across the alveolar and capillary membranes of the lungs, where it binds to hemoglobin in erythrocytes, and, to a much lesser extent, is dissolved in blood plasma. The degree of binding of oxygen to hemoglobin is governed by the partial pressure of oxygen, represented by the hemoglobin dissociation curve (**Figure 1.3**).

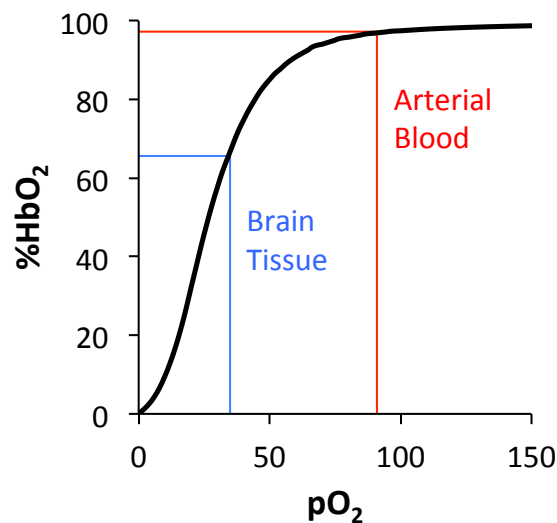


Figure 1.3: Hemoglobin (Hb) dissociation curve illustrating the relationship between oxygen partial pressure (pO_2) and percent hemoglobin oxygen saturation ($\%HbO_2$). Normal values for arterial blood and brain tissue are indicated. The sigmoidal shape of the curve results from cooperative binding of oxygen at the four heme sites of the Hb tetramer, and facilitates unloading of oxygen from blood to brain tissue along the pO_2 gradient.

In normal physiologic and atmospheric conditions, the oxygen partial pressure (pO_2) in the arterial blood is 80-100 mmHg, resulting in an arterial oxygen saturation (Y_a) of approximately 98 percent hemoglobin oxygen saturation ($\%HbO_2$). Because pO_2 in the brain (and other end-organs) is much lower, oxygen is released in these tissues from hemoglobin and diffuses along a decreasing pO_2 gradient: across the capillary membrane, through the cellular membrane of neurons and glial brain cells, and finally into the mitochondria where aerobic metabolism takes

place. The oxygen depleted venous blood, with about 1/3 of its hemoglobin desaturated, is returned to the heart and lungs. This process of oxygen extraction is schematically illustrated in **Figure 1.4**. The different magnetic properties of oxygenated and deoxygenated hemoglobin provide the foundation for MR-based quantification of blood oxygen saturation and $CMRO_2$, discussed in **Section 1.2.4**.

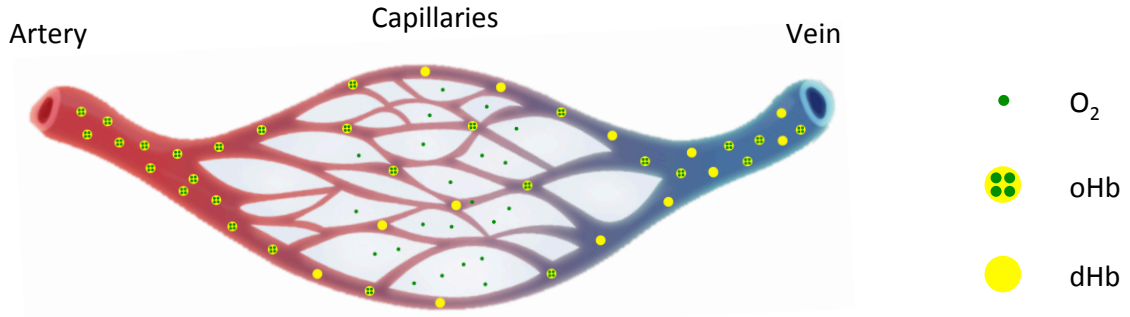


Figure 1.4: Schematic illustration of brain oxygen extraction in the capillaries. oHb is oxygenated hemoglobin and dHb is deoxygenated hemoglobin.

1.2.2. Fick Principle for $CMRO_2$ Quantification

Assuming all oxygen extracted from the blood is used for ATP production, the Fick Principle (**Equation 1.2**) can be used to quantify $CMRO_2$ (10-12):

$$CMRO_2 = C_a \cdot CBF \cdot (Y_a - Y_v) \quad [1.2]$$

where Y_a and Y_v are the arterial and venous oxygen saturation in %HbO₂, CBF is the cerebral blood flow in μmol per minute per 100 g of brain tissue, C_a is the arterial oxygen content of fully saturated arterial blood (i.e., blood with $Y_a = 100$ %HbO₂) in μmol of O₂ per mL blood, giving $CMRO_2$ in μmol per minute per 100 g of brain tissue. C_a is a Hb-dependent constant:

$$C_a = 0.620559 \cdot Hb \quad [1.3]$$

where Hb is in g/dL and the scaling factor is calculated from a hemoglobin molar mass of 64458 g/mol (43). Y_a can be measured continuously with a digital pulse oximeter, leaving Y_v and CBF to be quantified from the MR imaging experiment. $Y_a - Y_v$ is often called the arteriovenous oxygen difference (AVO_2D). Brain oxygen extraction is frequently reported in terms of the OEF, which is equal to AVO_2D/Y_a . OEF and AVO_2D values are very similar for Y_a in the normal range, and are sometimes used interchangeably.

Kety and Schmidt (11,12) were the first to quantify $CMRO_2$ using the Fick Principle. To quantify CBF, they integrated the differential concentration of nitrous oxide (N_2O) in the arterial and venous blood during continuous inhalation of N_2O gas. Y_a and Y_v were measured directly via co-oximetry of arterial and venous blood. Though accurate and well validated, the technique is highly invasive, requiring catheterization of the femoral artery and jugular vein. It also provides only a single steady-state global measurement of Y_v , CBF, and $CMRO_2$. However, this landmark work laid the foundation for the vast array of cerebral blood flow, oxygenation, and metabolism measurement and mapping techniques introduced in the subsequent 60 years.

1.2.3. Non-MR-Based Methods

1.2.3.1. Optical Methods

Several optical methods exist for quantification of cerebral blood flow and oxygen saturation. These methods take advantage of the fact that oxyhemoglobin (oHb) and deoxyhemoglobin (dHb) absorb light at different wavelengths.

Jugular bulb oximetry (JBO) involves intravenous insertion of a fiber optic probe and determination of Y_v from the absorption spectrum of different wavelengths of light. JBO can be combined with transcranial Doppler (44) measurement of CBF for quantification of $CMRO_2$. While the approach has the advantage of allowing continuous bedside monitoring, the catheter insertion is invasive and prone to serious complications such as carotid artery puncture (45), and the technique is prone to errors due to poor catheter tip placement and calibration (46).

Optical methods can also be applied to regional measurement of blood flow and oxygenation. Near-infrared spectroscopy (NIRS) (47) involves application of light with wavelength 650-1100 nm, which can penetrate the scalp, skull, and brain to a depth of several centimeters. The measured absorption spectra are used to estimate relative concentrations of oHb and dHb, which are then used to derive Y_v . A complementary optical technique for CBF measurement, diffuse correlation spectroscopy (DCS) (48), measures the scattering of near-infrared light in tissue. NIRS and DCS can be combined to quantify local $CMRO_2$ (49); however, the low penetration depth of light inherently limits the approach to measurement of cortical regions near the skull surface. Thus, the technique is best suited to studies involving neonates (50), whose skulls are thinner, or in animals, where smaller brain sizes and use of cranial windows improves light penetration.

1.2.3.2. PET

PET involves the injection or inhalation of exogenous, positron-emitting radioactive tracers with specific chemical properties. The emitted positrons annihilate with surrounding electrons to produce equal energy 511 keV photons that are emitted in opposite directions and detected by the PET scanner. The position of these detection events can be used to tomographically compute the spatial distribution of annihilation events, and, thus, the spatial distribution of the tracer.

PET-based quantification of $CMRO_2$ (51-53) uses intravenous injection of $H_2^{15}O$ water to quantify CBF and separate inhalation of radioactive $^{15}O_2$ gas to quantify OEF, which together can be used to quantify $CMRO_2$. Although the method is considered the gold standard for $CMRO_2$ mapping, it has a number of significant limitations. It is highly invasive, requiring both arterial and venous punctures, as well as exposure to radiation. Due to the complexity and cost of the protocol, and the need for an on-site cyclotron to produce the ^{15}O tracers, only a handful of sites around the world are equipped to conduct PET-based $CMRO_2$ studies. While the generated $CMRO_2$ maps are of high quality, the spatial resolution is somewhat coarse ($\approx 5 \text{ mm}^3$). Furthermore, the acquisition time is on the order of tens of seconds, limiting applications in functional experiments.

1.2.4. MR-Based Methods

1.2.4.1. MRI Contrast and CMRO₂

Unlike PET, MRI is inherently non-invasive and relatively ubiquitous in modern medical centers. MRI is based on nuclear magnetic resonance (NMR), the process by which atomic nuclei absorb and re-emit electromagnetic radiation. In MRI, a strong magnetic field is used to polarize nuclear spin magnetic moments. Application of radiofrequency (RF) pulses matching a particular nuclei's resonant (Larmor) frequency causes rotation of those moments into the plane perpendicular to the main field, and precession of the moments about the main field induces a measurable signal in RF coils via electromagnetic induction. This signal will decay with a time constant called the effective transverse relaxation rate (R_2^*). The portion of the signal decay due to static field inhomogeneity can be removed by spin-echo refocusing, thus isolating the transverse relaxation rate (R_2). These two quantities define a third relaxation rate, R_2' , where $R_2' = R_2^* - R_2$. R_2' represents the rate of signal decay due to static magnetic field inhomogeneities, but is only an exponential decay constant when this inhomogeneous field distribution is Lorentzian. These relaxation rates are often defined in terms of relaxation times: $T_2^* = 1/R_2^*$, $T_2 = 1/R_2$, and $T_2' = 1/R_2'$.

Imaging is made possible by the application of magnetic field gradients, which result in spatial information being encoded into the resulting MR signal (54). While MRI is possible with any nuclei possessing non-zero spin magnetic moment, because the human body is mostly composed of hydrogen-containing water molecules, ^1H is the nucleus of choice for most human MRI imaging. The varying chemical and structural properties of tissues have different effects on the time evolution of the MR signal, which can be exploited by different combinations of RF pulses and gradients (pulse sequences) to produce images with widely varying contrast. The tunability and variety of MR contrast has made it an enormously powerful tool for clinical diagnosis and scientific discovery.

A fundamental limitation of NMR and MRI is that the degree of polarization of nuclear magnetic moments is quite small, only a few parts per million, and the exponential time constant for

repolarization (the T_1) is quite long, on the order of seconds for many tissues of interest. For this reason, tradeoffs between signal-to-noise-ratio (SNR), spatial resolution, and temporal resolution must be considered in almost all MRI applications, including CMRO₂ quantification techniques.

While direct detection of oxygen with ^{17}O MRI is possible, enriched ^{17}O is enormously expensive, and the detection sensitivity is low. The Fick Principle offers an alternative approach as CBF can be measured non-invasively using either phase-contrast MRI (PC-MRI) (55) in large cerebral vessels or mapped on a voxel-wise basis with arterial spin labeling (ASL) (56,57). Y_a can be measured with pulse oximetry or assumed to be near 98 %HbO₂ in normal conditions. This leaves quantification of Y_v , which is the crux of MR-based CMRO₂ quantification methods. Y_v is itself of interest in certain applications, for instance, in stroke, where it may provide a marker for potentially salvageable tissue (29,30).

MR-based Y_v quantification takes advantages of the unique magnetic properties of the metalloprotein hemoglobin, first demonstrated by magnetic mass balance experiments conducted by Linus Pauling and Charles Coryell in 1936 (58). In the deoxygenated state, the Fe^{2+} heme iron's six electrons in the five 3d orbitals are distributed across the e_{gg} and t_{2g} orbitals, resulting in four unpaired electrons and a spin $S = 2$. When the heme iron becomes oxygenated, the ligand field separating the t_{2g} and e_{gg} orbitals is increased, making the configuration in which all electrons occupy the three t_{2g} orbitals more energetically favorable, and resulting in an electron spin $S = 0$. Thus, only dHb is paramagnetic, whereas oHb is diamagnetic. dHb paramagnetism causes a linear increase in the magnetic susceptibility of blood, and also has varying effects on the relaxation rates of blood and surrounding tissue.

The paramagnetism of dHb is exploited in a variety of MR-based techniques to quantify Y_v and CMRO₂, as summarized in **Table 1.1** and detailed in the sections that follow. These methods can be categorized based on the tissue compartment in which the effects of dHb are modeled (extravascular vs. intravascular) and the MR contrast method used to quantify these effects (T_2^* , T_2' , T_2 , or susceptibility). Furthermore, the methods are distinguished by whether the

measurements are made on a global, regional, or voxel-wise basis, and the resultant tradeoff between their spatial and temporal resolutions.

Signal Origin	Contrast	Spatial Res.	Method (Ref)	Y_v Temp. Res.	Simul. CBF?
Extravascular	T_2^*	Voxel-wise	Calibrated BOLD (59)	0:03	YES
	T_2'	Voxel-wise	qBOLD (60)	8:30	NO
Intravascular	T_2	Global	TRUST (61)	0:24	NO
		Regional	TRU-PC (62)	2:50	NO
			Projection-based T_2 (63)	0:15	NO
		Voxel-wise	QUIXOTIC (64)	27:30	NO
			VSEAN (65)	6:18	NO
	Susceptibility	Global	OxFlow (66)	0:28	YES
		Regional	Quantitative Venography (67)	15:42	NO
		Voxel-wise	Zhang et al. (68)	60:00	NO

Table 1.1: Summary of MR-based Y_v /CMRO₂ quantification methods and their respective features. ‘Signal origin’ is the tissue compartment in which signal used for Y_v quantification is modeled. ‘Contrast’ is the MRI contrast mechanism used in the Y_v quantification model. ‘Spatial Res.’ is the spatial resolution for Y_v quantification in minutes:seconds. ‘Method (Ref)’ is the name/acronym or authors associated with the published method and the most relevant citation. ‘ Y_v Temp. Res.’ is the reported approximate temporal resolution for a single Y_v measurement (ignoring any requisite planning or calibration scans). ‘Simul. CBF?’ denotes whether the method pulse sequence measures CBF simultaneously with Y_v .

1.2.4.2. Extravascular T_2^* -Based Methods (Calibrated BOLD)

Because CMRO₂ measurement has many potential advantages compared to standard BOLD fMRI (see section 1.1.3.1), the development and application of BOLD fMRI has been paralleled by attempts to resolve CMRO₂ from the BOLD signal. This requires modeling the various physiologic factors that contribute to the BOLD signal, schematically illustrated in **Figure 1.5**. Neuronal activation causes a local increase in both CMRO₂ and CBF; however, the increase in CBF is several times greater than what is required to meet the additional CMRO₂ demand (16), resulting in a counterintuitive decrease in the OEF and thus [dHb], the concentration of deoxyhemoglobin in a voxel. CBF also independently increases the venous cerebral blood volume (CBV_v) fraction, which acting alone would increase [dHb]. Overall, the CBF washout effect

dominates, resulting in a reduction in [dHb] and the characteristic increase in signal intensity in R_2^* -weighted BOLD fMRI images.

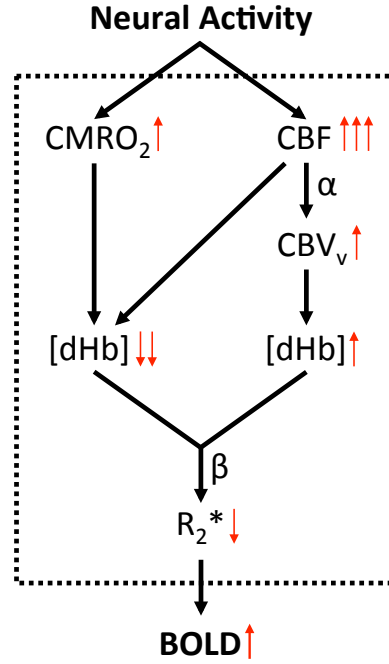


Figure 1.5: Schematic diagram illustrating the various physiologic contributions relating neuronal activity to BOLD signal.

BOLD signal is a simple exponential function of R_2^* and echo time (TE). Because fractional BOLD signal changes are only a few percent, the exponent can be linearized:

$$\frac{\Delta BOLD}{BOLD_0} = -TE \cdot \Delta R_2^* \quad [1.4]$$

where subscript 0 denotes the baseline state and Δ denotes the change from baseline to activation. ΔR_2^* can be expressed as:

$$\Delta R_2^* = A \cdot \left(CBV_v \cdot [dHb]_v^\beta - CBV_{v_0} \cdot [dHb]_{v_0}^\beta \right) \quad [1.5]$$

where subscript v denotes the venous blood compartment, and A is a scaling factor that incorporates effects due to vessel geometry, magnetic field strength, and the susceptibility difference between blood and tissue (69,70).

The supralinearity (i.e., $\beta > 1$) of **Equation 1.5** results from the combined effects of: 1) the linear exponential decay of spins in the vicinity of large venous vessels as predicted by the static dephasing model of Yablonskiy and Haacke (71) and 2) the quadratic exponential decay of spins in the vicinity of small vessels (capillaries) as predicted by the Luz-Meiboom model of fast exchange (72). Monte Carlo simulations based on the distribution of vessel sizes in the brain have suggested a β value of 1.5 at 1.5 T (70). The majority of functional imaging studies in recent years have been conducted at 3.0 T field strength, where β is predicted to be closer to 1.3 (73). However, this traditional physical interpretation of β is oversimplified; for example, it does not account for intravascular BOLD effects, which are especially significant at lower field strengths.

Although non-invasive techniques for direct quantification of CBV exist, most notably vascular-space-occupancy (VASO) MRI (74), they suffer from lower sensitivity, and cannot easily distinguish between arterial and venous CBV. Furthermore, the VASO method requires imaging at a specific blood inversion null point, making whole brain coverage difficult. Thus, total CBV is generally derived from ASL-measured CBF based on the Grubb power relationship relating CBV to CBF (75):

$$\frac{CBV}{CBV_0} = \left(\frac{CBF}{CBF_0} \right)^\alpha \quad [1.6]$$

where α is the Grubb constant. While the original Grubb constant value (0.38) accounts for total CBV changes, because only dHb-containing CBV_v , rather than total CBV, determines BOLD signal, recent work has suggested a lower value of α , 0.18 (76) or 0.23 (77). Although typically treated as a constant, α may potentially vary between subjects and brain regions (78-80).

Combining **Equations 1.4-1.6** and invoking the Fick Principle (with Y_a approximated to equal 100 %HbO₂) gives an expression relating BOLD signal changes to CMRO₂ and CBF:

$$\frac{\Delta BOLD}{BOLD_0} = TE \cdot A \cdot CBV_{v_0} \cdot [dHb]_{v_0}^\beta \cdot \left(1 - \left(\frac{CMRO_2}{CMRO_{2|0}} \right)^\beta \left(\frac{CBF}{CBF_0} \right)^{\alpha-\beta} \right) \quad [1.7]$$

The above equation can be simplified further by defining M, the maximum possible BOLD signal change that would result from total washout of all dHb from a voxel during a maximal CBF response (59,81). In this theoretical situation, the entire term in parentheses would reduce to 1 (as the CBF term would dominate), resulting in the expression known as the Davis model (59):

$$\frac{\Delta BOLD}{BOLD_0} = M \cdot \left(1 - \left(\frac{CMRO_2}{CMRO_{2|0}} \right)^\beta \left(\frac{CBF}{CBF_0} \right)^{\alpha-\beta} \right) \quad [1.8]$$

Despite the aforementioned problems with the definitions of α and β , simulations based on a more complete BOLD signal model suggest that the general form of **Equation 1.8** is valid if the traditional physical interpretations of α and β are relaxed and they are instead treated as fitting constants (82). This heuristic approach suggests lower values for α (0.14) and β (0.91) would be optimal.

With knowledge of M, subsequent measurement of CBF and BOLD during a functional paradigm allows quantification of fractional changes in CMRO₂ by solving **Equation 1.8**. However, M likely varies both across subjects and brain regions (83,84), and must therefore be “calibrated”.

Davis et al. first demonstrated an approach to BOLD calibration via hypercapnic gas-mixture breathing (59). Assuming that hypercapnia does not result in changes in CMRO₂ allows further simplification of **Equation 1.8**:

$$\frac{\Delta BOLD}{BOLD_0} = M \cdot \left(1 - \left(\frac{CBF}{CBF_0} \right)^{\alpha-\beta} \right) \quad [1.9]$$

M is derived from measurement of BOLD and CBF signal during both baseline and hypercapnia.

Application of hypercapnia calibrated BOLD to functional tasks may provide improved intra- and inter-subject reproducibility compared to traditional BOLD signal methods (85). However, the method has several limitations. Breathing hypercapnic gas can induce breathlessness, which may especially be problematic in clinical patients who are distressed or infirm. Furthermore, the assumption of isometabolism has been challenged in several recent papers employing direct CMRO₂ quantification based on T₂ (86,87). Due to the large exponent on the relative CBF changes in **Equation 1.9**, the technique is highly sensitive to noisy ASL-derived CBF data.

Recently, an alternative approach to BOLD calibration based on hyperoxic gas-mixture breathing was proposed (88). Hyperoxia is assumed to cause minimal changes in blood flow (89). Following the derivation of the deoxyhemoglobin dilution model (81) and assuming minimal hyperoxic CBF changes results in the following calibration model:

$$\frac{\Delta BOLD}{BOLD_0} = M \cdot \left(1 - \left(\frac{[dHb]_v}{[dHb]_{v_0}} \right)^{\beta} \right) \quad [1.10]$$

where [dHb]_v is assumed to vary uniformly across the brain and is quantified via capnographic measurement of end-tidal O₂ (EtO₂) before and during hyperoxia. This approach avoids the patient discomfort associated with hypercapnia as well as the sensitivity of the model to errors in ASL-derived CBF (which is assumed to remain constant). **Equation 1.10** does not require invoking the Fick Principle, and therefore does not make the assumption that Y_a equals 100 %HbO₂. However, it has the major disadvantage of requiring an assumed baseline Y_v value in order to derive [dHb]_v from the EtO₂ measurements. While Y_v is quite uniform across the brain

(16), it varies considerably even between healthy subjects (61,66). Finally, hyperoxia is believed to induce a modest reduction in CBF. Although this can be incorporated into the model, it is difficult to measure for individual subjects due to the low sensitivity of ASL to small hyperoxic flow changes and further complicated by the T_1 shortening of blood due to dissolved O_2 .

Even more recently, several groups (90,91) have proposed combining multiple gas-mixture breathing paradigms in order to improve the precision of calibrated BOLD, as well as to allow extension of calibrated BOLD to the quantification of not just fractional $CMRO_2$ changes but also resting state $CMRO_2$. Of course, the need for multiple gas manipulations adds further complexity to the experimental protocol.

Calibrated BOLD is the single current $CMRO_2$ quantification with both voxel-wise spatial resolution and sufficient temporal resolution for application to functional experiments. However, it is fraught with challenges, including a complex experimental setup and the many physiologic assumptions inherent in the signal model and calibration procedures. The technique also suffers from low precision, such that significant spatial averaging is often required to yield physiologically plausible $CMRO_2$ values, negating the advantages of voxel-wise coverage.

1.2.4.3. Extravascular T_2' -Based Methods (qBOLD)

Like calibrated BOLD, T_2' -based methods involve modeling the effects of intravascular dHb on extravascular signal. Rather than invoking the semi-empirical model of **Equation 1.5**, which requires calibration and corresponding physiologic assumptions, the MRI signal behavior is modeled explicitly in terms of known or measurable physical quantities by modeling the MRI signal in the so-called static dephasing regime (SDR). In the presence of magnetic field inhomogeneities, spins accumulate phase at different rates determined by the local magnetic field strength, causing phase incoherence and signal decay. Diffusion of spins between sites of different field strengths will also cause signal decay. In the SDR, it is assumed that static dephasing leads to complete signal decay before diffusion dephasing has an appreciable effect. These various effects are illustrated in **Figure 1.6**.

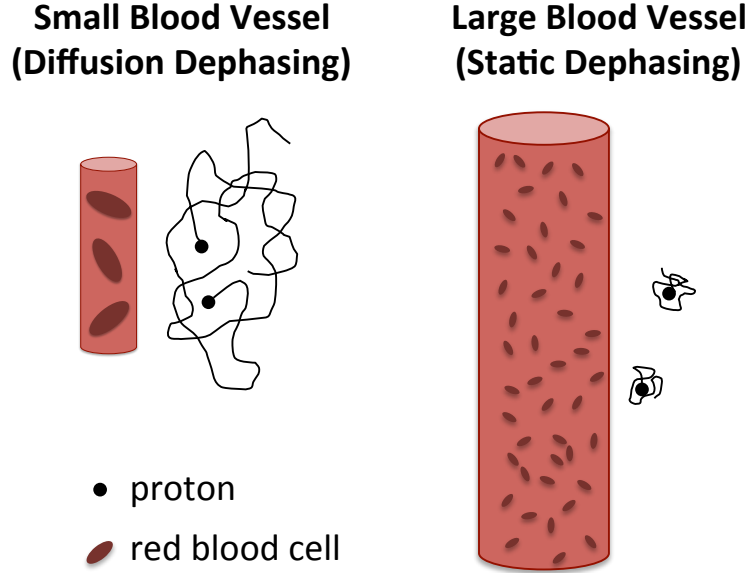


Figure 1.6: Schematic diagram illustrating how vessel size and diffusion distance determine diffusion dephasing versus static dephasing effects. When the vessel radius is small relative to the diffusion distance (left), two protons will dephase relative to one another as they randomly diffuse through a range of magnetic field strengths. When the vessel radius is large relative to the diffusion distance (right), two protons will dephase as a result of the different static magnetic field strengths in their local vicinities, long before diffusion dephasing can occur.

The time behavior of extravascular MR signal in the SDR was first described by Yablonskiy and Haacke (71). By modeling small blood vessels as a network of randomly oriented cylinders, Y_v can be expressed in terms of the spin-echo reversible decay rate, R_2' :

$$R_2' = CBV_v \cdot \gamma \cdot \frac{4}{3} \cdot \pi \cdot \Delta\chi_{do} \cdot Hct \cdot (1 - Y_v) \cdot B_0 \quad [1.11]$$

where $\Delta\chi_{do}$ is the susceptibility difference between fully oxygenated and fully deoxygenated erythrocytes (discussed further in **Section 1.2.4.5**), Hct is the blood hematocrit, and B_0 is the main magnetic field strength. It is noted that **Equation 1.11** has the same functional form as **Equation 1.5**; however, the SDR does not consider diffusion effects, and thus $\beta=1$.

The SDR model also predicts that in a free induction decay experiment, the time dependent MR signal, $S(t)$, exhibits different behavior in the short and long time scales related to the characteristic time, t_c :

$$S(t) = S(0) \cdot \exp \left[-\frac{4}{3} \cdot CBV_v \cdot \left(\frac{t}{t_c} \right)^2 - R_2' \cdot t \right] \quad t < 1.5 \cdot t_c \quad [1.12]$$

$$S(t) = S(0) \cdot \exp[CBV_v] \cdot \exp[-R_2' \cdot t] \quad t > 1.5 \cdot t_c \quad [1.13]$$

CBV_v can be solved from evaluation of **Equations 1.12-1.13**, leaving measurement of R_2' to determine Y_v . Several spin-echo-based pulse sequences have been developed for R_2' mapping. The method was first applied to human studies by An and Lin (92), and later improved upon by He and Yablonskiy (60), who additionally considered the effects of static field inhomogeneities and signal contributions from cerebrospinal fluid (CSF) and intravascular blood, dubbing the method 'quantitative BOLD' (qBOLD). Such methods have shown promise in defining the ischemic penumbra region in acute stroke and post-stroke recovery (93). A recent iteration of the method (94) suggest that a simulation-based "fingerprinting" approach (95) may allow better fitting of acquired data to the qBOLD model.

Although qBOLD achieves quantitative mapping of Y_v without gas calibration, it has several limitations. The signal model defined by **Equations 1.11-1.13**, despite its complexity and subsequent modifications in qBOLD, does not account for contributions from diffusion. The assumption of randomly oriented cylinders critical to the SDR model may be inappropriate near large blood vessels, highly vascularized tumors, or regions of iron deposition. Furthermore, R_2' mapping techniques are based on spin-echo sampling, and thus have relatively long acquisition times compared to echo-planar imaging (EPI)-based R_2^* mapping (BOLD). Thus, qBOLD temporal resolution is poor and strictly limited to measurement of steady-state Y_v and $CMRO_2$.

1.2.4.4. Intravascular T_2 -Based Methods

A variety of T_2 -based methods are based on isolation of venous blood T_2 , which can be related to Y_v through theoretical and empirical models. As blood water protons diffuse through the magnetic field inhomogeneities created by dHb-containing erythrocytes, spin-echo irreversible (T_2) dephasing occurs in the intravascular space. This decay can be estimated by a multi-spin-echo Carr-Purcell-Meiboom-Gill (CPMG) pulse sequence, containing 180 degree pulses with spacing t_{CPMG} . The Luz-Meiboom model for two-site fast exchange (72) can be modified and applied to diffusion of spins between intra- and extra- erythrocyte compartments (96-98) to quantify the R_2 of venous blood:

$$R_{2,blood} = R_{2,plasma} + Hct \cdot \left\{ \Delta R_{2,v} + (1 - Hct) \cdot (\Delta\omega_v)^2 \cdot \tau \cdot \left[1 - \frac{2\tau}{t_{CPMG}} \cdot \tanh\left(\frac{t_{CPMG}}{2\tau}\right) \right] \right\} \quad [1.14]$$

where $R_{2,plasma}$ is the relaxation rate of blood plasma, $\Delta R_{2,v}$ and $\Delta\omega_v$ are the relaxation-rate and susceptibility-shift differences, respectively, between the erythrocytes and plasma for exchanging water in the blood, τ is the exchange time between frequency-shifted sites, and t_{CPMG} is the time spacing between consecutive 180-degree pulses in the CPMG echo train. This complex model can be simplified by combining multiple physical quantities into calibration constants, resulting in a second-order polynomial relating R_2 of blood and Y_v :

$$R_{2,blood} = A + B \cdot (1 - Y_v) + C \cdot (1 - Y_v)^2 \quad [1.15]$$

where A, B, and C are Hct- and CPMG spacing (t_{CPMG})-dependent constants which can be determined empirically from ex vivo blood samples. Such an approach to Y_v quantification was first demonstrated by Wright et al. in the major thoracic vessels (98) and later demonstrated in cerebral veins in response to visual stimulation (96,99). **Figure 1.7** shows an example calibration curve obtained from ex vivo blood samples.

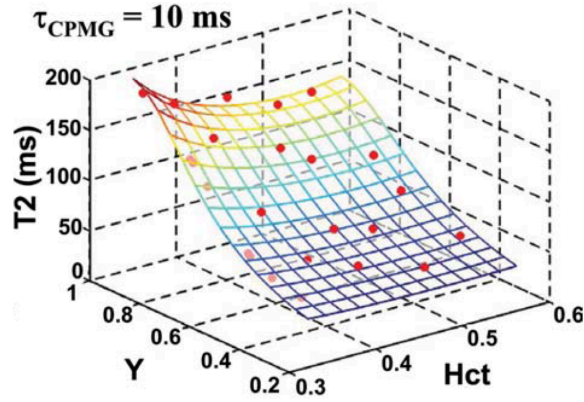


Figure 1.7: Calibration curve relating Y_v to measured T_2 and Hct for $t_{\text{CPMG}}=10$ ms. Each red dot represents an ex vivo blood sample with known Hct and Y_v obtained from gold-standard co-oximetry. Figure adapted from (100).

Determining the values of the calibration constants in **Equation 1.15** is a major challenge for these T_2 -based methods. These constants lack specific physical meaning and must be determined empirically from measurements in ex vivo blood samples using a range of precisely controlled oxygenation and Hct levels. Furthermore, the constants must be derived separately for different field strengths and t_{CPMG} times, ideally using a sequence with a CPMG echo train identical to that used for in vivo T_2 mapping. Care must be taken in the calibration experiment to maintain normal blood chemistry (e.g., temperature and pH) and prevent blood settling.

Another major challenge for T_2 -based methods is the need to isolate pure blood signal, as partial voluming of tissue or CSF will significantly bias measured T_2 and Y_v . Even in the largest vessels, such as the superior sagittal sinus (SSS), blood signal isolation is non-trivial due to the relatively large voxel sizes required by the fast imaging readouts used in CPMG-based T_2 -mapping sequences. Several different approaches have been proposed, as discussed below.

Spin-tagging venous blood isolation (TRUST)

T_2 -Relaxation-Under-Spin-Tagging (TRUST) (61) isolates venous blood signal via application of spin tagging, similar in principle to ASL-based CBF quantification. Subtraction of equivalent images acquired with and without venous blood inverted (tag) isolates pure blood signal.

Application of various amounts of CPMG T_2 weighting prior to imaging allows for quantification of blood T_2 . This method has been applied in both the SSS and internal jugular veins, with very comparable values obtained (101), suggesting that the SSS can be used as a surrogate for global Y_v . Combining TRUST with PC-MRI CBF quantification allows determination of $CMRO_2$ (101).

Since its introduction, TRUST has been improved in terms of speed and reliability (102) and extensively validated (100,103,104). It has been applied widely in physiologic investigations including the effects of hypercapnia (87), hypoxia and hyperoxia (105), caffeine (106), exercise (107), and cognitive training (108), in studies of neonatal development (109) and normal aging (110), and in diseases including multiple sclerosis (111) and mild cognitive impairment (112). Although providing a robust and reliable approach to global Y_v quantification, TRUST temporal resolution for $CMRO_2$ quantification is on the order of minutes, due to the temporally inefficient nature of CPMG-based T_2 -mapping and the need for a separate measurement of CBF. This limits the methods application to steady-state measurement of $CMRO_2$.

Phase-contrast venous blood isolation (TRU-PC, projection-based T_2)

As an alternative to spin tagging, blood signal can also be isolated through complex difference subtraction of images acquired with different first gradient moments (62,63), in a similar manner to PC-MRI blood flow quantification. An advantage of this approach over TRUST is that it does not require spin tagging in a drainage territory corresponding to a particular vein, and can thus be applied to smaller cortical vessels with arbitrary vessel geometry, as demonstrated using the T_2 -Relaxation-Under-Phase-Contrast (TRU-PC) method (62).

A similar technique using a projection-readout was demonstrated to quantify Y_v in as little as 15 seconds (63). However, because the complex difference signal is also dependent on blood flow, multiple averages are required to ensure blood flow effects are removed. This limits application of the technique to situations of steady-state blood flow, and partially negates the advantage of high temporal resolution.

The utility of regional Y_v quantification based on intravascular (as opposed to voxel-wise) measurement is fundamentally limited. Unlike arterial perfusion territories, venous drainage territories corresponding to particular vessels are poorly defined. Thus, determining the Y_v of a given tissue region from the Y_v measured within nearby veins is a major challenge. A recently proposed method for quantitative imaging of venous drainage territories (113) shows promise, though spatial and temporal resolution are significantly limited by the need to spatially encode both venous vessels and corresponding tissue regions separately.

Velocity-selective-excitation venous blood isolation (QUIXOTIC, VSEAN)

Clever application of velocity selective excitation pulses (114) in combination with blood tagging and T_2 -preparation similar to TRUST can be used to specifically isolate signal from venous blood in the post-capillary venous compartment. Two similar techniques, QUantitative Imaging of eXtraction of Oxygen and Tissue Consumption (QUIXOTIC) (64) and Velocity Selective Excitation with Arterial Nulling (VSEAN) (65), use this approach to obtain voxel-wise quantification of Y_v . However, because post-capillary blood comprises only a few percent of total parenchymal volume, these techniques suffer from low sensitivity and SNR. As such, they require multiple averages, and thus have long acquisition times even while being limited to a single acquisition slice. CSF signal contamination is also a concern, and may result in overestimation of Y_v values.

1.2.4.5. Intravascular Susceptibility-Based Methods

While the aforementioned techniques are based on modeling the effect of paramagnetic dHb on transverse relaxation, Y_v can also be more directly quantified by measurement of blood susceptibility itself. This technique exploits the relative paramagnetism of dHb versus oHb, which causes the susceptibility of whole blood relative to surrounding tissue, $\Delta\chi$, to be linearly related to Y_v (115):

$$\Delta\chi = Hct \left(\Delta\chi_{do} (1 - Y_v) + \Delta\chi_{oxy} \right) \quad [1.16]$$

where Hct is venipuncture-derived hematocrit, and $\Delta\chi_{do}$ and $\Delta\chi_{oxy}$ are the experimentally determined volume susceptibility differences between fully oxygenated and deoxygenated erythrocytes and fully oxygenated erythrocytes and water, respectively. Values of $4\pi \times 0.273$ p.p.m and $4\pi \times 0.008$ p.p.m. (SI units) are used for $\Delta\chi_{do}$ and $\Delta\chi_{oxy}$, respectively, based on theoretical calculations (116,117) as well as ex vivo calibration experiments (116,118). Of note, the model in **Equation 1.16** assumes that the susceptibilities of water, plasma, and tissue are the same to within experimental noise, and also assumes a single value for the mean corpuscular hemoglobin content (MCHC), the concentration of hemoglobin per volume of packed red blood cells. MCHC is known to vary in certain diseases, particularly anemia. Thus, a more complete model is obtained by substituting $MCHC_{norm}/Hb$ in place of Hct in **Equation 1.16**, where Hb is the individual subject's measured Hb, and $MCHC_{norm}$ is the MCHC value assumed in the derivation of the $\Delta\chi_{do}$ and $\Delta\chi_{oxy}$ constants, which, for the values used in this work (118), was 33.3 g/dL, corresponding to a Hct/Hb ratio of 0.03.

Although blood susceptibility cannot be measured directly, it induces a local field offset, ΔB , which can be measured with an MRI multi-echo gradient-recalled echo (GRE) field mapping sequence as:

$$\Delta B = \Delta\phi / \gamma\Delta TE \quad [1.17]$$

where $\Delta\phi$ is the difference in phase accrual between echoes spaced apart by ΔTE in the blood versus surrounding reference tissue, and γ is the proton gyromagnetic ratio.

Thus, solving for Y_v hinges on determining $\Delta\chi$ from the measured ΔB . This relationship can be described in terms of a convolution in the image domain:

$$\Delta B = d \otimes \chi \quad [1.18]$$

where d is the dipole kernel, or a point-wise multiplication in the Fourier domain:

$$F(\Delta B) = D \cdot X \quad [1.19]$$

where D is the dipole kernel in the Fourier domain:

$$D = \frac{1}{3} - \frac{k_z^2}{k^2} \quad [1.20]$$

Because D contains zeros on a pair of conical surfaces at 54.6 degrees relative to the z-direction, inversion of the dipole kernel is ill-posed (119). Regularization or conditioning is necessary in order to find a unique solution for $\Delta\chi$ given ΔB (reviewed in (120)), the challenge of which forms the central focus of the growing field of quantitative susceptibility mapping (QSM).

Susceptometry-based oximetry (OxFlow)

Although inversion of **Equation 1.18** is ill-posed in the general case, it can be solved for certain simple susceptibility distributions, including ellipsoids, and, of particular relevance to blood vessels, cylinders. By modeling a venous vessel of interest as a pseudo-infinite cylinder (i.e., with length \gg width) and accounting for field cancellation due to the Lorentz sphere effect, the relationship between ΔB and $\Delta\chi$ is given by **Equation 1.21** (121,122):

$$\Delta B = \frac{1}{6} \Delta\chi B_0 (3\cos^2\theta - 1) \quad [1.21]$$

where θ is the vessel angle with respect to B_0 . Combining **Equations 1.16, 1.17, and 1.21** allows for determination of Y_v by measurement of $\Delta\phi$:

$$Y_v = 1 - \frac{6(\Delta\phi / \Delta TE)}{\gamma B_0 \Delta\chi_{do} Hct (3\cos^2\theta - 1)} + \frac{\Delta\chi_{oxy}}{\Delta\chi_{do}} \quad [1.22]$$

Theoretical modeling suggests this infinite cylinder model is quite accurate for vessels with angles less than 30 degrees relative to B_0 (123). The model is schematically illustrated in **Figure 1.8**.

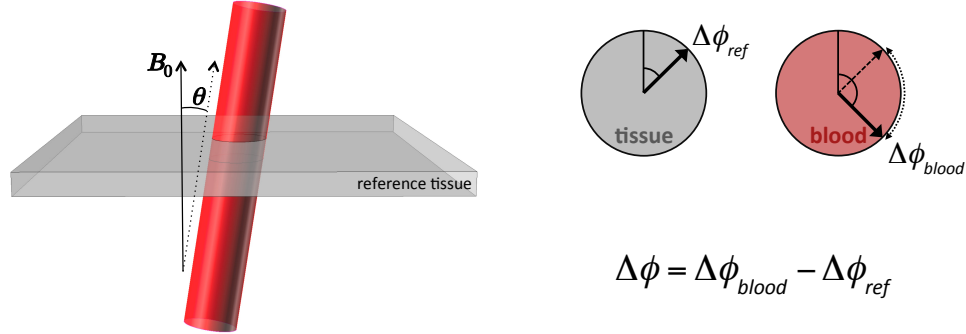


Figure 1.8: Schematic illustration of a blood vessel approximated by the infinite cylinder model. Due to paramagnetic dHb, MR signal in the blood has additional phase ($\Delta\phi_{blood}$) compared to surrounding reference tissue ($\Delta\phi_{ref}$). The phase difference ($\Delta\phi$) and vessel angle (θ) are the two imaging-derived parameters used to compute Y_v in **Equation 1.22**.

In addition to providing a surrogate for global Y_v (63,101), the SSS is long, relatively straight, and nearly parallel to the B_0 field when the subject is lying supine in an MRI scanner, making it an excellent candidate for application of the infinite cylinder model (**Equation 1.21**). Application of this susceptometry-based oximetry (SBO) approach to Y_v quantification in the SSS has been validated both theoretically (123) and with anatomical phantom models (66).

Because it is based on a simple 2D GRE phase mapping sequence, SBO is very fast compared to T_2 -based methods such as TRUST, and can be naturally interleaved with GRE-based PC-MRI for simultaneous quantification of Y_v and CBF, and, thus, $CMRO_2$. This combined blood Oxygenation and Flow (OxFlow) pulse sequence has been used to quantify $CMRO_2$ at rest (66) as well as in response to hypercapnia in both adults (124) and neonates with congenital heart disease (125).

The simple, first principle model relating $\Delta\phi$ to Y_v in SBO is a major advantage over the complex, ex vivo calibration model required in TRUST and other T_2 -based Y_v techniques. However, this

model is also a limitation, as it restricts SBO to vessels that are sufficiently long, straight, and parallel to the B_0 field. Regional venous vessels with appropriate geometry are limited, making the technique ideally suited for global Y_v quantification in the SSS. A second limitation of SBO is that static magnetic field inhomogeneity from non-dHb sources (e.g., air-tissue interfaces) must be removed. This can be accomplished with polynomial fitting (126), but will perform poorly in situations of severe background field variation (e.g., near metal orthodontics).

Quantitative susceptibility mapping (Quantitative Venography, technique by Zhang et al.)

The second subset of susceptibility-based Y_v quantification techniques involve 3D phase mapping of the brain and dipole inversion using QSM techniques. This has been done by: 1) focusing on only the intravascular signal to determine Y_v of large and medium sized (MRI-resolvable) veins (67), and 2) modeling the susceptibility effects of the small venous blood compartment of tissue to determine voxel-wise Y_v (68). The first approach produces a venogram of Y_v values in the venous vascular tree, whereas the second gives voxel-wise Y_v maps similar to the qBOLD technique. In both methods, ASL is used to measure CBF. Acquisition times for the 3D field maps are several minutes, thus, both techniques are limited to measurement of baseline physiology or steady-state stimuli.

Though technically remarkable, these methods have significant practical limitations. As with T_2 -based techniques for small vessel Y_v quantification, the venogram approach requires relating vessel-specific Y_v values to voxel-wise CBF values, for which there is currently no feasible approach. Though the voxel-wise method avoids this problem, due to the small blood volume fraction of tissue, the induced changes in susceptibility are approximately two orders of magnitude smaller than the corresponding susceptibility shifts measured using intravascular methods. In fact, the intravascular blood susceptibility model (**Equation 1.16**) ignores such shifts in tissue susceptibility entirely. Furthermore, the voxel-wise method requires imaging during both baseline and an assumed isometabolic stimulus (with caffeine used in (68)) in order to separate blood and non-blood susceptibility effects.

1.2.4.6. Dynamic Quantification of CMRO₂

Measurement and mapping of steady-state CMRO₂ has proven useful in studies of human physiology, and demonstrated promise as a potential biomarker in neurologic disease. However, the brain must respond to dynamic changes in oxygen supply and demand that occur on the order of seconds, including physiologic stimuli such as acute hypoxia as well as neuronal activation during functional tasks. Better methodology for dynamic quantification of CMRO₂ – both whole brain quantification and mapping – is needed. Such methods would provide insight into how neuronal signaling events unfold over time, and the temporal dynamics of neurometabolic-hemodynamic coupling. It could also provide a tool to study diseases of altered neurometabolism and neurovascular reactivity.

In assessing the existing methods for MR-based CMRO₂ quantification, there are clear tradeoffs between robustness, spatial coverage, and temporal resolution. Simultaneous quantification of Y_v and flow is critical for any dynamic technique, and currently possible only with calibrated BOLD and SBO. Only calibrated BOLD has sufficient temporal resolution to measure dynamic functional changes and also provide voxel-wise spatial resolution. Unfortunately, it relies on complex theoretical and experimental models, and only relative values are possible without multiple calibration states. On the other end of the spectrum, OxFlo provides a robust and relatively rapid means of whole-brain CMRO₂ quantification. It has been used to study physiologic and pathologic processes that are expected to affect the whole brain uniformly and thus do not require mapping, for example, the response to hypercapnia. However, even OxFlo is an order of magnitude slower than BOLD, thus limiting its ability to probe the dynamic neurometabolic response to acute stimuli or functional activation.

1.3. Outline of Dissertation Chapters

This dissertation describes the development and application of novel MR-based CMRO₂ quantification methods capable of dynamic assessment of cerebral metabolism. In **Chapter 2**, a simple, susceptibility-based OxFlo method for whole-brain CMRO₂ quantification with three-

second temporal resolution is described, validated, and applied to demonstrate a small but significant increase in CMRO_2 in response to volitional breath-hold apnea. In **Chapter 3**, this rapid OxFlow method is combined with the robust and reproducible, but much slower TRUST technique. The resulting interleaved TRUST (iTRUST) pulse sequence achieves significantly improved T_2 -based CMRO_2 temporal resolution, and permits direct, simultaneous comparison of susceptibility- and T_2 -based Y_v quantification. iTRUST is used to investigate the highly debated hypercapnic CMRO_2 response to better interpret conflicting results from recent studies. In **Chapter 4**, the potential for improved calibrated BOLD via direct quantification of global Y_v is described and demonstrated using a novel pulse sequence combining OxFlow with traditional multi-slice, double-echo ASL/BOLD. Using hyperoxia and hypercapnia gas-mixture breathing protocols, the technique is demonstrated in comparison to the traditional Davis model approach. Finally, in **Chapter 5**, the methods outlined in **Chapter 2** are translated in a small clinical pilot study of OSA patients and controls. OSA-associated differences in both baseline CMRO_2 and the CMRO_2 apneic response are reported and discussed.

Chapter 2: High Temporal Resolution Quantification of Global Cerebral Metabolic Rate of Oxygen Consumption in Response to Apneic Challenge

2.1. Abstract

We present a technique for quantifying global CMRO₂ in absolute physiologic units at three-second temporal resolution and apply the technique to quantify the dynamic CMRO₂ response to volitional apnea. Temporal resolution of three seconds was achieved via a combination of view-sharing and SSS-based estimation of tCBF rather than tCBF measurement in the neck arteries. These modifications were first validated in three healthy adults and demonstrated to produce minimal errors in image-derived blood flow and Y_v values. The technique was then applied in 10 healthy adults during an apnea paradigm of three repeated 30 s breath-holds. Subject-averaged baseline tCBF, AVO₂D, and CMRO₂ were 48.6 ± 7.0 mL/100g/min (mean \pm SD), 29.4 ± 3.4 %HbO₂, and 125.1 ± 11.4 μ mol/100g/min, respectively. Subject-averaged maximum changes in tCBF and AVO₂D were $43.5 \pm 9.4\%$ and $-32.1 \pm 5.7\%$, respectively, resulting in a small ($6.0 \pm 3.5\%$) but statistically significant ($P = 0.00044$, two-tailed t-test) increase in average end-apneic CMRO₂. This method can be used to investigate neurometabolic-hemodynamic relationships in normal physiology, to better define the biophysical origins of the BOLD signal, and to quantify neurometabolic responsiveness in diseases of altered neurovascular reactivity.

2.2. Introduction

Because cerebral metabolism is almost entirely oxidative, continuous O₂ delivery to the brain is critical and tightly regulated. The CMRO₂, defined as the brain oxygen consumption rate per unit tissue mass, is a direct measure of oxidative metabolism, in contrast to indirect measures such as perfusion or BOLD MRI signal. Therefore, CMRO₂ is an ideal parameter for investigating relationships between neuronal activity, blood flow, and cerebral metabolism in normal physiology

and diseases of cerebrometabolic dysfunction. In fact, alterations in cerebral oxygen metabolism are associated with many of the most common neurologic disorders, including mild cognitive impairment (112), Alzheimer's disease (34), Parkinson's disease (127), and multiple sclerosis (111).

In recent years, significant progress has been made toward non-invasive MR-based methods for absolute CMRO₂ quantification. Much attention has focused on developing methods to quantify CMRO₂ absolutely (in physiologic units) and on a voxel-wise basis. As overviewed in **Chapter 1**, such voxel-wise methods model the effect of deoxygenated hemoglobin on either brain tissue T₂' (60), T₂ (64), or BOLD signal (90) to quantify the voxel-wise Y_v, which can be combined with ASL CBF measurement to yield CMRO₂. In contrast, methods that quantify oxygen extraction globally model the effect of dHb on the intravascular T₂ (63,101) or MR signal phase (66,128) of large veins to quantify intravascular Y_v, which combined with PC-MRI-based quantification of CBF yields CMRO₂. Although these intravascular methods lack the ability to measure local changes in oxygen metabolism, many physiologic states and neurologic disorders are global in nature, and therefore assessable via measurement of global CMRO₂. Furthermore, voxel-wise absolute CMRO₂ techniques require many minutes for each CMRO₂ measurement and therefore cannot quantify changes in response to dynamic physiologic challenges or neurologic stimuli. By sacrificing spatial specificity, intravascular methods enable CMRO₂ quantification in clinically feasible scan-times and at much higher temporal resolutions – seconds rather than minutes – compared to voxel-wise approaches.

Based on the infinite cylinder model (121,122), SBO is a simple and robust method for intravascular CMRO₂ quantification. Unlike T₂ relaxation-based methods for quantifying intravascular Y_v, the paramagnetic cylinder model approach does not require prior calibration to specific scanners, sequences, or blood Hb/Hct values (Hb and Hct are input parameters theoretically included in the model). It also has equal accuracy and precision across all Y_v values and is scalable with field strength. These features make the model suitable for application to a

variety of clinical populations and experimental conditions, including longitudinal and multi-center studies. The simplicity of this approach also enables rapid CMRO₂ quantification in response to stimuli. For example, in recent work (124), CMRO₂ was measured at 25-second temporal resolution in response to hypercapnia by application of a SBO method and found to be constant during hypercapnic steady state. Though 25-second temporal resolution represents a drastic improvement over previous approaches, changes in cerebral oxygen supply and demand take place on the order of seconds, and thus require yet improved temporal resolution to be fully resolved. Calibrated BOLD-based methods can assess relative CMRO₂ changes in seconds (85), however, such methods cannot quantify CMRO₂ in absolute physiologic units. Furthermore, these BOLD-based methods require calibration via gas-mixture breathing, complicating application to human subjects, and are based on the assumption that the response to such gases is isometabolic, itself a topic of debate (117).

Higher temporal resolution CMRO₂ quantification would provide valuable insight into global neuronal activity during various dynamic stimuli. For instance, it could be applied to validate whether the aforementioned gas-mixture breathing stimuli used in calibrating the BOLD fMRI signal, including hypercapnic (59,81) and hyperoxic (88) gas-mixture breathing as well as breath-hold (129), are in fact isometabolic and over what time frame (i.e., whether a delay exists in reaching an isometabolic steady state). Validating these assumptions is critical given the extensive use of fMRI in biomedical research and the growing interest in making BOLD fMRI more quantitative. Further, applying the dynamic CMRO₂ method to neuronal activation tasks could help elucidate the biophysical mechanisms underlying the BOLD response, including the relative CMRO₂ contribution to the BOLD post-stimulus undershoot, a topic of significant contention (130).

Breath-hold apnea is another important area of investigation where high temporal resolution CMRO₂ measurement is essential. Apnea is involved in a number of important diseases, such as asthma, chronic obstructive pulmonary diseases, and OSA. The normal physiologic response to

apnea maintains cerebral oxygen delivery via reduced cardiac output, peripheral vasoconstriction, and cerebral vasodilation (131). However, it has been suggested that in OSA the repeated nocturnal apneic events caused by upper airway mechanical failure may result in blunting of this normal response (37,132,133), potentially explaining the extensive neurologic pathology associated with the disease. Exploration of this hypothesis requires better methods for quantifying the cerebrometabolic apneic response. While non-MR methods such as Doppler ultrasound (37) or NIRS (133) have been applied to study the neurometabolic response to apnea in subjects with OSA, these techniques measure changes in either CBF or tissue O_2 saturation (S_tO_2), but not $CMRO_2$, which requires simultaneous quantification of CBF and tissue oxygen extraction. $CMRO_2$ is maintained across healthy subjects both at baseline (66) and in response to certain physiologic stimuli such as hypercapnia (124), suggesting that it is a more significant index for assessing neurovascular dysfunction than either blood flow or oxygenation alone. Developing methods to better assess the normal $CMRO_2$ response to apnea and its potential alteration in OSA could improve understanding of OSA neuropathology and provide insight into OSA treatment.

In this section, we present and validate a method for dynamic $CMRO_2$ quantification with three-second temporal resolution, which extends the SBO approach previously described (66) to dynamic stimuli. This temporal resolution is achieved by using view-sharing to reduce the number of phase-encode lines by four-fold and by combining the Y_v and flow quantification portions of the sequence. After validating the assumptions inherent in these temporal-resolution-improving measures, the technique was applied to a cohort of healthy individuals during a volitional apnea paradigm, both to demonstrate the method's sensitivity and to characterize the normal apneic $CMRO_2$ response.

2.3. Methods

2.3.1. $CMRO_2$ Quantification via the Fick Principle

The cerebral metabolic rate of oxygen is estimated by combining venous and arterial oxygen saturation and tCBF measurements using the Fick Principle (10-12):

$$CMRO_2 = C_a \cdot tCBF \cdot (Y_a - Y_v) \quad [2.1]$$

where $CMRO_2$ is the cerebral metabolic rate of oxygen consumption in μmol per minute per 100 g brain tissue, $tCBF$ is the total cerebral blood flow in mL per 100 g brain tissue per minute, Y_a and Y_v are the arterial and venous oxygen saturation in %HbO₂, and C_a is the arterial oxygen content in μmol of O₂ per mL blood, a product of the measured hemoglobin concentration (Hb) and the O₂ carrying capacity of hemoglobin. C_a varies for each subject, and is given by:

$$C_a = 0.620559 \cdot Hb \quad [2.2]$$

where Hb is the venipuncture-derived hemoglobin in g/dL and the scaling factor is based on a hemoglobin molar mass of 64458 g/mol (43). Y_a can be measured continuously with a digital pulse oximeter, leaving Y_v and $tCBF$ to be quantified from MRI.

2.3.2. Principles of Susceptometry-Based Global $CMRO_2$ Quantification

SBO exploits the relative paramagnetism of deoxygenated versus oxygenated hemoglobin, which causes the susceptibility of whole blood relative to surrounding tissue, $\Delta\chi$, to be linearly related to Y_v (115):

$$\Delta\chi = Hct \left(\Delta\chi_{do} (1 - Y_v) + \Delta\chi_{oxy} \right) \quad [2.3]$$

where Hct is the venipuncture-derived hematocrit, and $\Delta\chi_{do}$ and $\Delta\chi_{oxy}$ are the experimentally determined volume susceptibility differences between fully oxygenated and deoxygenated erythrocytes and fully oxygenated erythrocytes and water, respectively. Values of $4\pi \times 0.273$ and $4\pi \times 0.008$ p.p.m. (SI units) are used for $\Delta\chi_{do}$ and $\Delta\chi_{oxy}$, based on ex vivo calibration experiments (116,118).

Although this blood susceptibility cannot be measured directly, it induces a local field offset, ΔB , which can be measured with an MRI multi-echo GRE field mapping sequence as:

$$\Delta B = \Delta\phi / \gamma\Delta TE \quad [2.4]$$

where $\Delta\phi$ is the difference in phase accrual between echoes spaced apart by ΔTE in the blood versus surrounding reference tissue, and γ is the proton gyromagnetic ratio. Quadratic fitting is used to remove contributions to $\Delta\phi$ from static field inhomogeneities (126).

Solving for Y_v thus hinges on determining $\Delta\chi$ from the measured ΔB , an inversion problem that is mathematically ill-posed in the general case (119). However, by modeling the vessel of interest as a pseudo-infinite, circular cylinder, and accounting for field cancelation due to the Lorentz sphere phenomenon (121,122), the relationship between ΔB and $\Delta\chi$ can be calculated analytically:

$$\Delta B = \frac{1}{6} \Delta\chi B_0 (3\cos^2 \theta - 1) \quad [2.5]$$

where θ is the vessel angle with respect to the main magnetic field, B_0 . Combining **Equations 2.3-2.5** allows determination of Y_v by measurement of $\Delta\phi$:

$$Y_v = 1 - \frac{6(\Delta\phi / \Delta TE)}{\gamma B_0 \Delta\chi_{do} Hct (3\cos^2 \theta - 1)} + \frac{\Delta\chi_{oxy}}{\Delta\chi_{do}} \quad [2.6]$$

Because the SSS is long, relatively straight, and virtually parallel to the B_0 field with the subject lying supine, it is an excellent candidate for application of the infinite cylinder model. Application of the model to the SSS has been validated both theoretically (123) and with anatomical phantom models (66). Furthermore, the SSS is the largest cerebral vein, and it has been shown that oxygen saturation levels in the SSS are comparable to global cerebral Y_v levels measured in the internal jugular vein (63,101), making the SSS an appropriate surrogate for global cerebral Y_v . Direct susceptibility-based measurement of Y_v in the internal jugular vein is difficult due to the often severe susceptibility artifacts caused by the proximity of air spaces such as the oral cavity and trachea.

2.3.3. Combination of SBO and PC-MRI for CMRO₂ Quantification (OxFlow)

Non-gated PC-MRI is used to quantify tCBF. The method utilizes motion-sensitizing gradient waveforms to encode information about velocity into the phase of the MR signal. Specifically, the pulse sequence involves two interleaves, both having null zeroth gradient moment along the direction of blood flow but nonzero first gradient moment. The latter determines the sensitivity of the accrued phase difference between the two interleaves, $\Delta\phi$, to the velocity of the flowing spins as:

$$\Delta\phi = \gamma\Delta M_1 v \quad [2.7]$$

where ΔM_1 is the difference in the first moment between the two interleaves and is dictated by a user-defined parameter VENC, defined as:

$$VENC = \gamma\Delta M_1 / \pi \quad [2.8]$$

VENC represents the velocity that causes a net phase accrual of π radians and therefore the maximum velocity that can be resolved without phase aliasing, and is typically chosen to be approximately 30% higher than the maximum velocity expected. Flow is quantified from velocity maps via multiplication of average vessel blood flow velocity by vessel cross-sectional area. In order to quantify CMRO₂ per unit brain mass, flow must be normalized to total brain volume, which is quantified with a T₁-weighted 3D magnetization-prepared rapid GRE (T₁ MP-RAGE) pulse sequence (134).

In previous work, these phase-based techniques for quantifying Y_v and tCBF have been combined to quantify global CMRO₂ at rest (66) and during hypercapnic gas breathing (124). In this approach, Y_v is measured in the SSS and tCBF is measured simultaneously in the internal carotid and vertebral arteries of the neck using a two-slice-interleaved multi-echo GRE sequence. Four interleaves are required for each phase encoding, two to generate susceptibility weighted

phase difference maps and two to generate velocity encoded phase maps, resulting in a temporal resolution of 25 seconds.

2.3.4. Pulse Sequence Modifications for Improved Temporal Resolution

Modification of the susceptibility-based CMRO₂ technique to achieve three-second temporal resolution (**Figure 2.1**) was accomplished via two changes to the original approach:

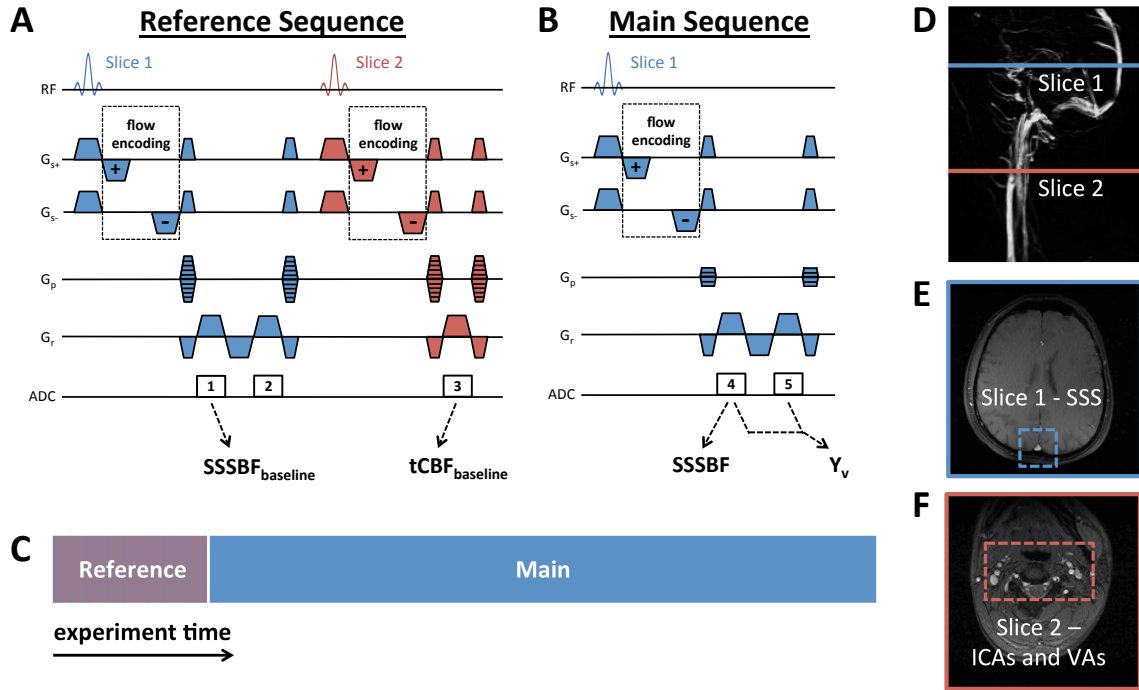


Figure 2.1: High temporal resolution CMRO₂ quantification pulse sequence. (A) A two-slice-interleaved fully phase-encoded reference sequence is run immediately before (B) the single-slice main sequence with 4x phase-encode reduction; (C) Experimental schematic illustrating relative timing of the reference and main sequence; (D) Sagittal maximum intensity projection image indicating slice locations corresponding to the pulse sequence diagram with magnitude images highlighting (E) the SSS in the head slice and (F) the internal carotid arteries (ICAs) and vertebral arteries (VAs) in the neck slice. Figure from (135).

1. Combining of sequence interleaves: Rather than using two interleaves with different echo times to generate the Y_v weighted phase-difference map, a multi-echo readout enables generation of a phase-difference map from data acquired in a single interleave. Any phase accrued due to velocity encoding will equally affect both echoes of the multi-echo readout, as both echoes have

the same polarity. Thus, the velocity and susceptometry interleaves can be combined. As a consequence of this modification, SSS blood flow (SSSBF) is quantified rather than tCBF from the neck arteries. However, tCBF can be accurately estimated by calibrating SSSBF based on the SSSBF:tCBF ratio measured at baseline with a two-slice-interleaved version of the sequence. This reference sequence (**Figure 2.1a**) is run immediately before starting the main (SSS-only) high temporal resolution CMRO₂ sequence (**Figure 2.1b**), which is continued for the remainder of the scan. This modification yields a two-fold temporal resolution increase.

2. Keyhole (136) reconstruction with reduced phase encoding lines: The number of phase-encode lines in the main (SSS-only) CMRO₂ sequence is reduced by a factor of four from 208 to 52, and outer k-space is filled with data acquired from the same fully-phase encoded reference sequence used for calibrating SSSBF to tCBF (outer k-space data from echoes 1 and 2 in **Figure 2.1a** is added to continuously updated central k-space data from echoes 4 and 5 in **Figure 2.1b**). Unlike the main sequence, the reference sequence retains full phase encoding to facilitate Keyhole image reconstruction and allow higher fidelity quantification of the SSSBF:tCBF ratio. This modification yields a four-fold temporal resolution increase.

The resultant pulse sequence (**Figure 2.1a-b**) has the following parameters: FOV = 208×208 mm² (head slice), 176×176 mm² (neck slice), voxel size = 1×1×5 mm³ (head slice), 0.85×0.85×5 mm³ (neck slice), TR/TE1/ΔTE = 28.85/5.5/7.04 ms, bandwidth = 521 Hz/pixel, flip angle = 15 degrees, VENC = 60 cm/s (head), 80 cm/s (neck), temporal resolution = 12 s (reference sequence), 3 s (main sequence). The modifications described combine to provide an eight-fold improvement in temporal resolution without reducing theoretical SNR. In fact, because two phase-difference maps are simultaneously generated at every time point (one for each flow encoding) and subsequently averaged, SNR should theoretically improve by approximately $\sqrt{2}$.

The modifications described depend on several crucial assumptions that must be validated:

1. In order to determine tCBF from the SSSBF:tCBF ratio at baseline, the SSSBF:tCBF ratio must remain constant throughout the experiment. Because the SSS receives venous blood from most

of the cortex, this assumption should be valid, especially during global physiologic challenges such as apnea or gas-mixture breathing.

2. Keyhole reconstruction assumes that dynamic information is band-limited in k-space (i.e., image changes are low spatial-frequency processes). To satisfy this assumption, the diameter of any features of interest must be approximately greater than the Keyhole reduction factor times the static resolution, or 4 mm for the 1 mm resolution and 4x Keyhole reduction factor used in the sequence described. The SSS is approximately 10 mm in diameter, and thus should fulfill this requirement.

3. Keyhole reconstruction assumes anatomic correspondence between the reference images and the main sequence images, and therefore requires that there be no movement over the course of the experiment. This is achievable at the level of the SSS because it is easy to keep the head stationary in the MR scanner, even during a challenging paradigm such as volitional apnea.

In addition to improving temporal resolution, another motivation for velocity measurement in the SSS only is that the neck vessels are more prone to movement, especially during physiologic paradigms such as apnea, violating assumption 3, and are also relatively smaller, violating assumption 2.

2.3.5. In Vivo Magnetic Resonance Imaging Studies

Human subject studies were approved by the Institutional Review Board of the University of Pennsylvania. Ten healthy volunteers (6 males, 4 females, ages 29 ± 4 years) were recruited and participated after giving written informed consent. The subjects were judged to be healthy on the basis of their medical history. The particular population demographic was chosen to ensure maximal subject compliance to the physiologic paradigms. In all studies, images were acquired on a 3T Siemens Tim Trio system (Siemens Medical Solutions, Erlangen, Germany) using a 12-channel head coil and 2-channel neck coil. A vendor-provided GRE axial localizer scan was used to select the location of the vessels of interest (SSS, internal carotid arteries, and vertebral

arteries) and estimate θ , the tilt angle of the SSS with respect to B_0 , from the coordinates of the centroid of the vessel for quantification of Y_v as in **Equation 2.6**.

2.3.5.1. Validation of Critical Methodological Assumptions

Three of the volunteers (2 males, 1 female, ages 25 ± 1 years) completed a tube-breathing paradigm involving 2.5 minutes of normal breathing baseline, 2.5 minutes of breathing through 10 feet of plastic tubing with an attached mouthpiece to induce changes in flow and Y_v , and 2.5 minutes of normal breathing recovery. Tube-breathing was chosen in this validation study because it induces a mixed hypercapnic/hypoxic state, similar in nature to breath-hold but sustainable over a long enough duration to acquire multiple data points at both slice locations with full phase encoding (137). The fully phase-encoded, two-slice-interleaved reference sequence was run during the entire paradigm, allowing quantification of the SSSBF:tCBF ratio over the course of the paradigm to test whether it remains constant during an apnea-like physiologic paradigm (assumption 1). Using full phase-encoding also allows comparison of SSSBF and Y_v values obtained from retrospectively Keyhole reconstructed data, where various amounts of outer k-space are replaced at each time point with the corresponding data from the first time point, as if only the central k-space had originally been acquired, as is the case when running the main sequence. This tests whether changes in parameter values are sufficiently bandlimited in k-space to be accurately determined when using Keyhole sampling and image reconstruction (assumption 2). Finally, because the paradigm requires both manipulation of the tube mouthpiece and significantly increased respiration, it challenges the subject's ability to remain static (assumption 3).

2.3.5.2. Quantification of $CMRO_2$ in Response to Apneic Challenge

Volunteers completed an apnea paradigm involving three repeated blocks of a 30 s normal breathing baseline period, a 30 s breath-hold apnea period, and a 90 s normal breathing recovery period. Before being scanned, subjects were instructed that all breath-holds should be completed at functional residual capacity, in other words, at normal end expiration. After running the

reference sequence, the main sequence was run for the length of the 7.5-minute paradigm as in **Figure 2.1c**, allowing quantitation of Y_v and tCBF at three-second temporal resolution. Y_a was measured continuously during the paradigm with a digital pulse oximeter placed on the right middle finger. Except in cases of abnormal cardiac anatomy, blood pumped to the brain and periphery originates from the same mixed pool in the left ventricle and therefore has the same Y_a . Thus, digital pulse oximetry will reflect cerebral Y_a . To correct for the known temporal delay in the measured Y_a when using digital pulse oximetry, the Y_a curve was shifted forward in time for each subject so that arterial resaturation occurs 7.5 seconds after cessation of breath-hold, matching the known circulatory transport delay between the lungs and brain (138) to within the temporal resolution of the MR pulse sequence (3 s). Breath-hold at normal end expiration was chosen to keep breath-holds as consistent as possible across repeats and subjects, ensuring that inspiration would occur immediately at the end of the breath-hold period. Subjects were verbally coached during the imaging experiment to “breathe in”, “breathe out”, and “stop breathing” six, three, and zero seconds before the start of each apnea period, respectively, to ensure exact timing of the breath-holds. All subjects were able to successfully complete each of the breath-holds as confirmed by direct observation and pulse oximetry data. Following the breath-hold paradigm, a T_1 -weighted MP-RAGE image data set (voxel size = $1 \times 1 \times 1 \text{ mm}^3$) was acquired for normalization of tCBF to brain volume. Total brain volume was obtained using a semiautomated region-growing algorithm in ITK-SNAP (139). After completion of the MR imaging experiment, each subject gave a venous blood sample, which was sent for complete blood count laboratory analysis to obtain a blood hemoglobin and hematocrit value.

2.3.6. Data Processing

In all experiments, binary masks were generated for the carotid and vertebral arteries and SSS by thresholding of complex difference images, which robustly isolates the signal from flowing blood. Y_v was quantified in the SSS from **Equation 2.6** with $\Delta\phi$ equal to the average phase difference between the reference tissue and the SSS ROI. Flow was quantified in the neck arteries and SSS

by multiplying average velocity by cross sectional area for each corresponding vessel ROI, summing over the four neck arteries to get tCBF.

In the tube-breathing experiments, images were retrospectively Keyhole-reconstructed at Keyhole reduction factors of 2, 4, 8, and 16 by discarding all but the central 104, 52, 26, or 13 lines of k-space, respectively, and replacing outer k-space with corresponding data from the first image of the data set. In the apnea paradigm experiments, corresponding data acquired from the reference sequence was used to fill missing outer k-space data from the main sequence run for the duration of the paradigm.

All time-course data from the apnea experiments was averaged over the three repeated blocks of the paradigm to remove physiologic noise not related to the paradigm and improve SNR. Average baseline parameter values were quantified from the first 24 seconds (8 data points) of the baseline period to exclude breathing effects from the coached inspiration and expiration during the final 6 seconds (2 data points) of the baseline period. Data from only the final 15 seconds (5 data points) of the apnea period were used to generate end-apnea parameter values to eliminate residual breathing effects and because physiologic changes due to apnea are not expected to occur instantaneously.

2.4. Results

Tube-breathing produced a similar response across the three subjects. Time-course plots of Y_v , tCBF, and SSSBF in a representative subject (**Figure 2.2a**) demonstrate the expected increase in blood flow and venous oxygen saturation caused by hypercapnia that develops during the tube-breathing portion of the paradigm. Coefficients of variation of the SSSBF:tCBF ratio (assumed to remain constant for a given subject to allow tCBF estimation from SSSBF) across all time points ($N = 45$) were 0.094, 0.075, and 0.084 for the three subjects. The SSSBF:tCBF ratio for each subject averaged across the normal breathing baseline and recovery (30 data points) and tube-breathing (15 data points) portions of the paradigm is shown in **Figure 2.2b**. Welch's t-tests for equal means between these two groups of SSSBF:tCBF values yields non-significant P-values (> 0.40) for all subjects.

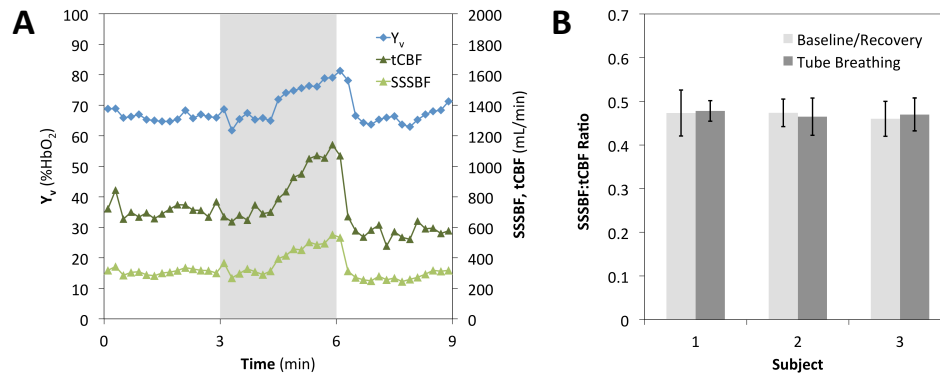


Figure 2.2: SSSBF:tCBF ratio determination in three subjects. (A) Time-course plot of Y_v , tCBF, and SSSBF in response to 3 minutes of tube-breathing (gray bar); (B) Histograms grouped by subject showing the SSSBF:tCBF ratio averaged over the baseline/recovery ($N = 30$ per subject) and tube-breathing ($N = 15$ per subject) portions of the paradigm with errors bars indicating ± 1 SD. Figure from (135).

Figure 2.3 demonstrates the effects of Keyhole reconstruction on the accuracy of derived parameters as observed from the tube-breathing experiment. In **Figure 2.3a**, time-course plots of Y_v and SSSBF derived from images with full phase encoding are compared to the same plots generated from images retrospectively Keyhole-reconstructed with a range of Keyhole reduction factors. Note the greater errors when larger Keyhole reduction factors are used. In **Figure 2.3b**, these errors are plotted versus number of phase-encode lines used in the Keyhole reconstruction. Values are averaged over the tube-breathing portion of the paradigm only, where errors should be greatest as observed in **Figure 2.3a**. For the Keyhole reduction factor of 4 used in the CMRO₂ quantification sequence, mean error and root-mean-square error (RMSE) had magnitudes less than 0.04 for both Y_v and SSSBF for all subjects.

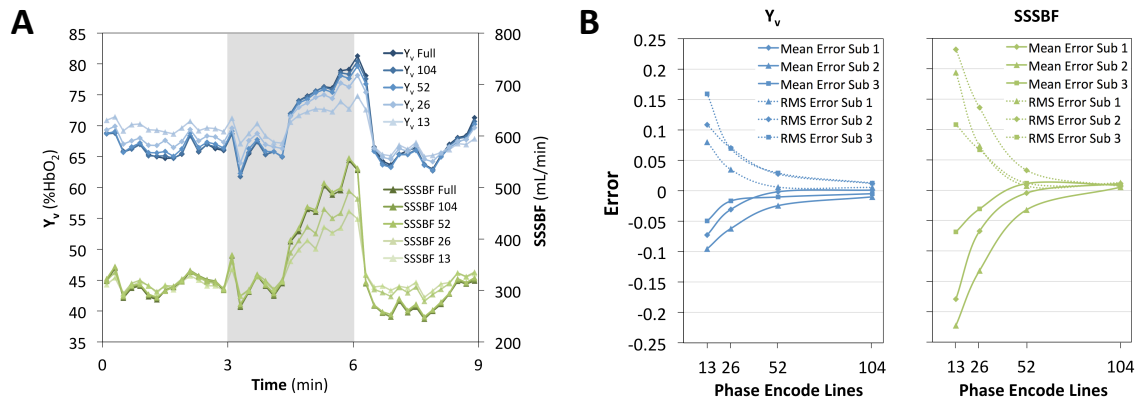


Figure 2.3: Error due to Keyhole reconstruction. (A) Time-course plot of Y_v and SSSBF in response to tube-breathing (gray bar) derived from images reconstructed with full phase encoding (208 phase encode lines) and retrospective Keyhole reconstruction with 104, 52, 26, or 13 phase encode lines used; (B) Percent mean error and RMSE in Y_v and SSSBF during tube-breathing using different numbers of phase encode lines for retrospective Keyhole reconstruction. 'Sub' stands for 'subject'. Figure from (135).

Figure 2.4 displays data from the apnea paradigm experiment in a typical subject. Changes in flow and Y_v in response to apnea are visualized in the corresponding velocity and phase difference maps (**Figure 2.4a**). Time-course plots of the measured parameters (**Figures 2.4b-c**) demonstrate an increase in Y_v and tCBF and a decrease in Y_a in response to apnea (gray bar). From these data, AVO_2D is quantified and plotted alongside the tCBF, the product of which yields $CMRO_2$ (**Figures 2.4d-e**).

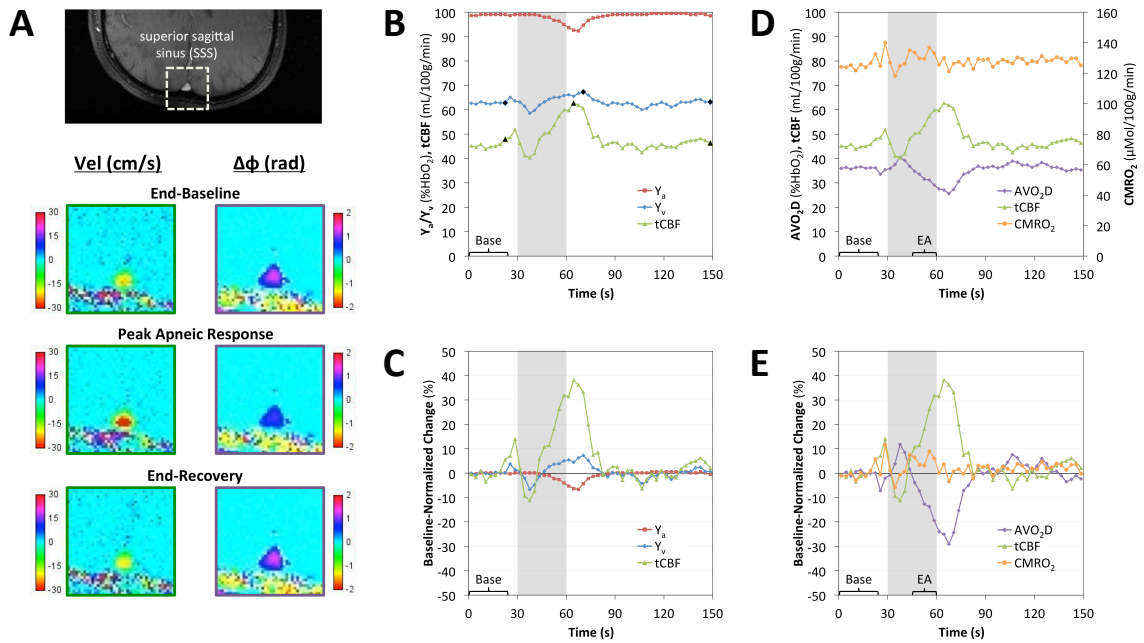


Figure 2.4: Apnea paradigm representative subject images and time course data. (A) Magnitude image with the SSS outlined and corresponding velocity and phase difference ($\Delta\phi$) maps from specific time points (denoted by black symbols in B); (B) Time-course plot of pulse oximetry measured Y_a and image-derived Y_v and tCBF absolute parameter values with black symbols corresponding to images in A; (C) percent changes in Y_a , Y_v , and tCBF parameter values normalized to average baseline value; (D) tCBF, AVO_2D , and $CMRO_2$ absolute parameter values and (E) percent changes in parameter values normalized to baseline. Gray bars indicate the apnea period. All values in time-course plots are averaged across the three repeats of the paradigm. The bracketed sections 'Base' and 'EA' indicate the data used for computing average baseline values and end-apnea values for each subject. Figure from (135).

Table 2.1 lists parameters extracted from the time-course data for each subject, both at baseline and in response to apnea. The average baseline Y_v , tCBF, and $CMRO_2$ values were 68.6 ± 3.0 %HbO₂, 48.6 ± 7.0 mL/100g/min, and 125.1 ± 11.4 μ mol/100g/min, respectively, consistent with previous findings (66). As previously observed (66), oxygen delivery (the product of C_a and tCBF) was negatively correlated with oxygen extraction (AVO_2D) at baseline ($r = -0.76$, $P = 0.011$, two-tailed t-test). Maximum percent changes in tCBF and AVO_2D were $43.5 \pm 9.4\%$ and $-32.1 \pm 5.7\%$, respectively, resulting in a small ($6.0 \pm 3.5\%$) but significant ($P = 0.00044$, two-tailed t-test) increase in $CMRO_2$ between baseline and end-apnea (final 15 s of apnea period).

Parameter		Subject										Mean	SD
		1	2	3	4	5	6	7	8	9	10		
tCBF (mL/100g/min)	Baseline	52.3	51.7	43.8	54.8	45.4	37.5	55.8	58.0	39.9	46.4	48.6	7.0
	Maximum	83.6	70.1	62.0	82.9	62.8	52.1	73.9	91.4	55.8	64.8	69.9	12.9
	Change (%)	60.0	35.6	41.3	51.1	38.2	38.9	32.5	57.6	40.0	39.7	43.5	9.4
Y_v (%HbO ₂)	Baseline	66.0	69.0	68.2	72.3	62.7	67.3	72.5	71.0	67.2	69.5	68.6	3.0
	Maximum	73.6	72.4	77.0	76.1	67.3	73.0	76.0	79.8	72.3	74.0	74.2	3.4
	Change (%)	11.6	5.0	12.9	5.2	7.3	8.5	4.9	12.4	7.6	6.4	8.2	3.1
Y_a (%HbO ₂)	Baseline	99.4	99.3	98.0	97.0	98.9	97.2	98.2	98.2	96.1	97.3	98.0	1.1
	Minimum	92.7	94.7	96.3	90.7	92.3	94.0	93.3	96.3	91.7	93.2	93.5	1.9
	Change (%)	-6.8	-4.6	-1.7	-6.5	-6.7	-3.3	-5.0	-1.9	-4.6	-4.2	-4.5	1.8
AVO_2D (%HbO ₂)	Baseline	33.4	30.2	29.8	24.7	36.2	29.9	25.7	27.1	28.9	27.8	29.4	3.4
	Minimum	20.0	22.3	19.4	15.7	25.7	21.5	17.3	16.5	22.3	19.2	20.0	3.1
	Change (%)	-40.0	-26.2	-35.0	-36.4	-29.1	-28.2	-32.8	-39.2	-22.8	-30.9	-32.1	5.7
$CMRO_2$ (μ mol/100g/min)	Baseline	142.2	135.8	118.8	122.0	125.5	104.9	140.0	123.5	117.4	120.6	125.1	11.4
	End-Apnea	147.1	155.8	122.6	130.3	132.5	107.2	147.4	130.1	126.9	126.9	132.7	14.1
	Change (%)	3.5	14.7	3.3	6.9	5.6	2.2	5.3	5.3	8.1	5.2	6.0	3.5

Table 2.1: Summary of individual subject and group (mean and SD) values of various extracted parameters at rest and in response to volitional apnea. Ave. Baseline (average value over the first 24 s of the baseline period), Maximum/Minimum (highest/lowest value reached over the entire paradigm), End-Apnea ($CMRO_2$ only: average value over the final 15 s of the apnea period); Change (percent change between Ave. Baseline and corresponding Maximum (Y_v , tCBF), Minimum (Y_a , AVO_2D), or End-Apnea ($CMRO_2$) parameter value. Table from (135).

The subject-averaged apneic response is displayed in the time-course plots of **Figure 2.5**. It is evident that flow increases during apnea and then undershoots before returning to baseline while oxygen extraction decreases during apnea and then overshoots before returning to baseline. The slightly larger magnitude of the flow increase compared to the AVO_2D decrease causes a small increase in $CMRO_2$ during apnea followed by a transient undershoot before return to baseline.

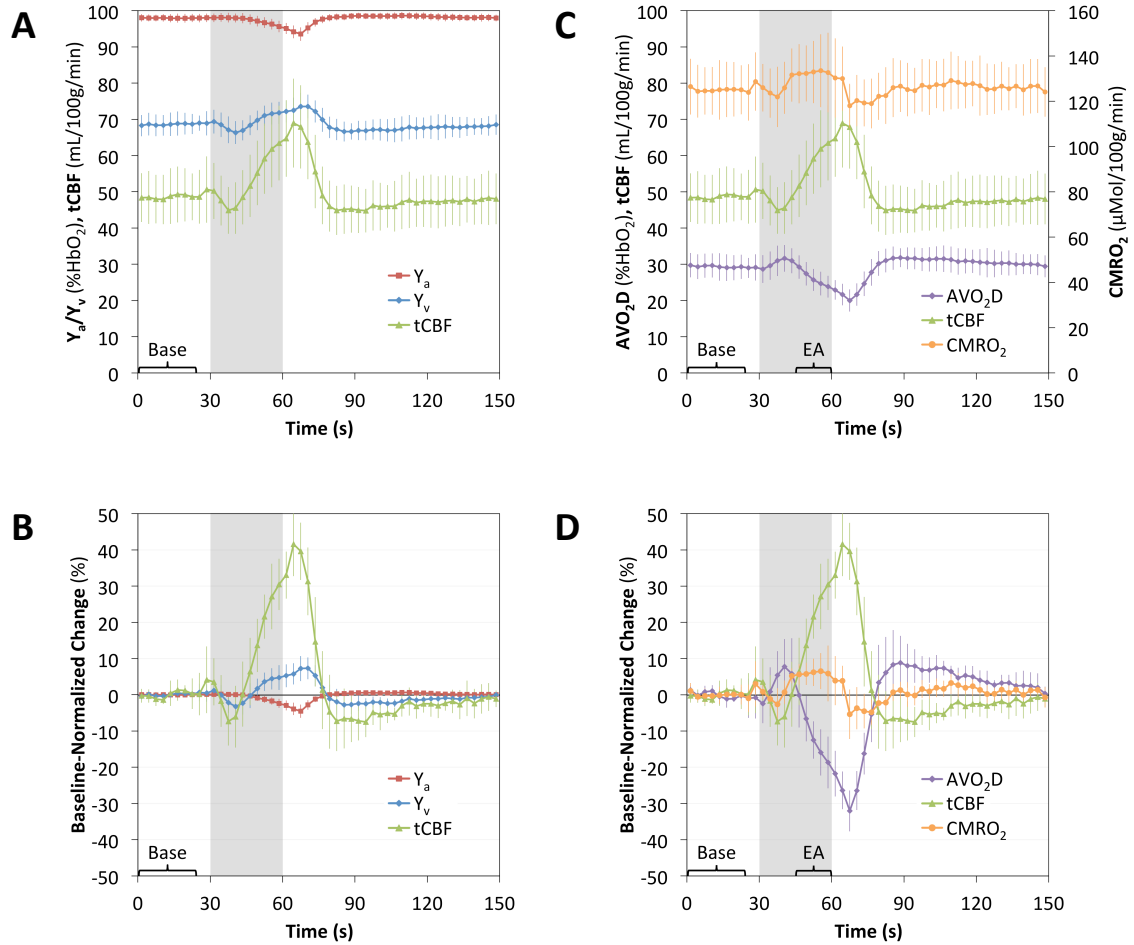


Figure 2.5: Apnea paradigm cohort time course data. (A) Time-course plot of cohort-averaged Y_a/V_v , Y_v/V_v , and tCBF absolute parameter values and (B) percent changes in parameter values normalized to average baseline; (C) tCBF, AVO_2D , and $CMRO_2$ absolute parameter values and (D) percent changes in parameter values normalized to average baseline. Error bars indicate ± 1 SD. Gray bars indicate the apnea period. All values in time-course plots are averaged across the three repeated blocks of the paradigm. The bracketed sections 'Base' and 'EA' indicate the data used for computing average baseline values and end-apnea values. Figure from (135).

2.5. Discussion

We have introduced an MR-based method for absolute quantification of CMRO₂ in humans with three-second temporal resolution. Key methodological assumptions were validated in a tube-breathing paradigm. The sensitivity of the technique to detect dynamic changes in cerebral blood flow, oxygen extraction, and CMRO₂ was assessed in response to a dynamic volitional apnea paradigm in a cohort of young healthy adults.

Results from the tube-breathing experiment (**Figures 2.2 and 2.3**) suggest application of the technique in the SSS produces only small systematic errors. Coefficients of variation of the SSSBF:tCBF ratio across all time-points of the paradigm were small (< 0.10) for each subject. Furthermore, Welch's t-tests for equal means comparing the SSSBF:tCBF ratio for tube-breathing and non-tube-breathing portions of the experiment were nonsignificant for all subjects ($P > 0.40$). Therefore, it appears that SSSBF closely parallels tCBF in response to tube-breathing. This result is expected considering that the SSS accounts for nearly half of tCBF and because a global physiologic paradigm such as tube-breathing would not be expected to have a regional bias. Because of the similarity between tube-breathing and apnea, the results support estimation of tCBF based on SSSBF for quantifying CMRO₂ in response to apnea or other global physiologic challenges.

Systematic errors due to Keyhole reconstruction were observed to decrease expectedly as the Keyhole reduction factor was decreased. Mean errors and RMSEs in flow and Y_v were less than 0.04 for all subjects and less than 0.02 averaged across subjects when using a reduction factor of 4.

In response to apnea, we observed a small ($6.0 \pm 3.5\%$) but significant ($P = 0.00044$, two-tailed t-test) increase in CMRO₂. Apnea has been used in the past as an assumed isometabolic stimulus in BOLD fMRI studies, both for calibrating the BOLD signal to quantify relative CMRO₂ changes (129) and as an isometabolic standard in studies investigating the BOLD post-stimulus undershoot (140). Our results suggest that apnea may be slightly pro-metabolic. Increased

CMRO₂ in response to apnea could represent a physiologic mechanism for buffering the brain energy supply in anticipation of prolonged apnea, which eventually would lead to exhaustion of energy stores and neuronal cell death. This would be consistent with other observations of the normal apneic response, such as reduced cardiac output, peripheral vasoconstriction, and cerebral vasodilation, which serve to maintain oxygen stores in the brain at the expense of the periphery.

Previous studies quantifying CMRO₂ using the Fick Principle have focused on baseline physiology or steady-state stimuli only. Specific considerations must be made in applying the Fick Principle during dynamic stimuli. For instance, there is a possibility that the amount of oxygen stored in brain tissue changes during apnea, due to either changes in CBV or pO₂. In applying the Fick Principle to large feeding or draining vessels, it is not possible to distinguish between changes in O₂ storage and true O₂ consumption (i.e., via aerobic metabolism). Potential errors in CMRO₂ due to O₂ storage effects are considered in the Appendix (**Section 2.7**), and shown to be negligible.

To our knowledge, no previous studies have directly quantified CMRO₂ during apnea, though studies of the CMRO₂ response to various gas mixtures provide insight into the present work. In recent work, a similar CMRO₂ technique employing SBO has shown that CMRO₂ does not change during hypercapnic steady state (124). However, apnea represents a mix of both hypercapnia and hypoxia, and never reaches a steady state. Data from the periods between steady states were not recorded in the prior study, and the temporal resolution used (25 s) would be unable to distinguish the transient changes in CMRO₂ detected in the present study. Studies of the CMRO₂ response to hypercapnia using T₂-based methods for Y_v quantification have yielded mixed results, with T₂-based intravascular approaches reporting both no change (141) and a 13.4 ± 2.3% decrease (87) in CMRO₂ in response to moderate hypercapnia. The latter T₂-based approach was recently applied to detect a 5.0 ± 2.0% average increase in CMRO₂ in response to mild (14% inspired FiO₂) steady state hypoxia (105), a difference of 18.4% compared

to the CMRO₂ response to hypercapnia using the same methodology. Given that apnea is a mixed hypercapnic/hypoxic stimulus, that similar SBO techniques as the one used in the present study have found hypercapnia to be isometabolic (124), and that T₂-based approaches support a large CMRO₂ difference between hypoxia and hypercapnia, the small apneic CMRO₂ increase observed in this study is not unexpected. Nevertheless, extrapolations based on steady-state gas-mixture breathing are of limited relevance to apnea, which is inherently non-steady state, involving continuously increasing levels of both hypercapnia and hypoxia.

Application of the proposed technique during administration of breathing gases (CO₂ and O₂) would better establish the relative contributions of hypercapnia and hypoxia to the observed apneic CMRO₂ response. Such studies would also suggest the extent to which hypercapnia and hypoxia are isometabolic, not only at steady state, but in the transition to steady state. Such information is critical given the use of CO₂ and O₂ in calibrating BOLD fMRI, as there is growing interest in making BOLD fMRI more quantitative through respiratory calibration.

The ability of the method to capture details of the temporal dynamics of the apneic response is especially well illustrated by the group-averaged time-course plots (**Figure 2.5**), which illustrate not only the neurovascular effects of apnea, but also the more subtle effects of respiration. Coached inspiration from six to three seconds prior to apnea causes reduced intrathoracic pressure and increased right atrial venous return, changes reflected by the small observed increase in CBF just prior to apnea initiation. In contrast, coached expiration during the final three seconds before apnea has the opposite effect, and the end-expiratory breath-hold state reached upon apnea initiation is also known to result in decreased cerebral venous blood flow (142). Indeed, CBF was observed to transiently decrease during the beginning of the apnea period, taking nearly half the apnea period for the flow increase due to apnea-induced hypoxia and hypercapnia to overcome the small flow reduction caused by the end expiration-induced reduction in cerebral venous blood flow. Finally, immediately after apnea cessation, another transient, sharp increase in flow is observed, likely also arising from the large initial inspiration at

the end of the apnea period. While opposite magnitude changes in the AVO_2D difference were observed during the same aforementioned inspiratory and expiratory periods, they are of lesser magnitude, and, therefore, flow driven $CMRO_2$ changes are recorded.

It is difficult to ascertain whether these transient $CMRO_2$ changes are real or arise from a temporary mismatch between the true (arterial) $tCBF$, and the SSS blood flow used to quantify $tCBF$ in the described technique. Inspiration and expiration during other free-breathing portions of the paradigm is not temporally matched across subjects and paradigm repeats, and is therefore averaged out of the time course data.

One possible limitation of the proposed method is the necessity of measuring Y_a with pulse oximetry. No arterial vessels of suitable geometry for application of the infinite cylinder model exist in the head or neck region. Furthermore, the SNR of SBO phase difference maps is proportional to the accrued phase, which is small in highly oxygenated arterial blood. Accurate Y_a quantification is critical as even a small underestimation in the Y_a drop would mitigate the observed increase in $CMRO_2$ in response to apnea. However, if underestimation of Y_a were the cause of the observed apneic $CMRO_2$ increase, one would expect the percent changes in Y_a and $CMRO_2$ in response to apnea to be positively correlated across subjects, however, this correlation was small, negative, and insignificant ($r = -0.18$, $P = 0.62$, two-tailed t-test).

An alternative approach to fast $CMRO_2$ quantification is the use of projection-based T_2 measurement, which achieves Y_v quantification in 15 s, is independent of vessel orientation, and is not sensitive to field inhomogeneities (63). However, the method assumes that flow remains constant over the course of each 15 s measurement. It is therefore not suitable for a paradigm, such as apnea, in which significant flow changes occur over seconds. Furthermore, the model used for determining $\%HbO_2$ values from T_2 measurements must be empirically calibrated to specific Hct values, with errors due to deviations in Hct becoming especially large for higher blood oxygen saturation levels.

2.6. Conclusions

In conclusion, we have introduced and validated an approach for rapid quantification of CMRO₂ with three-second temporal resolution, and applied it to characterize the CMRO₂ response to apnea. Potential clinical applications include investigation of diseases of altered neurometabolic response, for instance, obstructive sleep apnea. More broadly, by providing a simple, robust, and quantitative method for assessing CMRO₂ in response to physiologic stimuli, the technique can be used to investigate neurometabolic-hemodynamic relationships in a variety of normal physiologic and pathologic conditions.

2.7. Appendix: Non-Steady-State Application of the Fick Principle

In applying the Fick Principle to non-steady state stimuli such as volitional apnea, one must consider the potential confounding effects of dynamic changes in the amount of O₂ stored in the brain secondary to changes in either CBV or interstitial oxygen tension (piO₂).

Changes in CBF will cause a concomitant expansion of arterial and venous cerebral blood volume (CBV_a and CBV_v) (143) such that flow quantified in the large arteries or veins will not reflect instantaneous capillary flow. Because the OxFLOW method described measures CBF on the venous side in the SSS, only changes in CBV_v, and not CBV_a, will affect the relationship between measured CBF and instantaneous capillary flow. In response to apnea, we observed a flow increase of about 30% during the 15 s end-apnea period (**Figure 2.5**). Assuming a Grubb power law relationship (75) between CBV_v and CBF with $\alpha=0.18$ (76), and a baseline CBV_v of approximately 2% (60,144) (or 2 mL/100g tissue with blood and tissue approximated as having density equal to water), the calculated CBV_v change is $(1.30^{0.18}-1) \times 2 \approx 0.1$ mL/100g, or an average rate of 0.4 mL/100g/min over the 15 s end-apnea period. In other words, approximately 0.4 mL/100g/min of the blood flowing through the capillary bed was directed toward CBV_v expansion and not measured as tCBF. Given that this is less than 1% of tCBF, even at baseline, and that CMRO₂ is linear with tCBF, a reasonable upper bound for the underestimation of CMRO₂ during the end-apnea period is 1.3 μ mol/100g/min (1% of the average end-apnea CMRO₂). This

would correspond to a true average end-apnea CMRO₂ change of 7.1%, only slightly larger than the measured change of 6.0%.

Another potential mechanism of O₂ storage is the increase in piO₂ that accompanies increased CBF (145). Additional dissolved oxygen in the interstitial space would temporarily be stored rather than metabolized in cells, resulting in overestimation of the instantaneous CMRO₂. In response to apnea, CMRO₂ increased by 7.6 μmol/100g/min (**Table 2.1**), which is 1.9 μmol/100g after integration over the 15 s end-apnea period or 0.048 mL/100g applying the Ideal Gas Law at 37°C. Assuming an interstitial oxygen solubility of 0.003 mL/100g and interstitial volume fraction of 20% (146), Henry's Law predicts a piO₂ change of 80 mmHg would be required for additional O₂ storage in the interstitium to entirely account for the observed CMRO₂ change.

There is limited literature examining the piO₂ change associated with breath-hold; however, approximate values can be inferred from hypercapnia studies in animals. A study in Rhesus monkeys measured a 7 mmHg piO₂ increase in response to 5% CO₂ gas-mixture breathing (147). In humans, CBF changes in response to 5% CO₂ are of similar magnitude to those observed in response to 30 s apnea in the present study (43.5%) (87,124). In a study of rats exposed to hypercapnia (145), the derived relationship between piO₂ and CBF changes suggests a 43.5% increase in CBF would produce a piO₂ increase of about half that amount (22%), corresponding to a 7 mmHg increase from a baseline piO₂ of 30 mmHg. In both of these animal experiments, the expected piO₂ change is less than 10% of what would be required to drive an apparent 6.0% CMRO₂ increase. Furthermore, these inferred piO₂ changes likely represent upper bounds, as apnea-associated hypoxia will independently lower piO₂, opposing changes associated with increased CBF. Finally, if the observed CMRO₂ increase was driven by piO₂ changes, one would expect the maximum ΔtCBF and ΔCMRO₂ to be positively correlated across subjects, which was not the case ($\Delta\text{CMRO}_2 = -0.11 \times \Delta\text{tCBF} + 10.6$, $r^2 = 0.08$). In summary, O₂ storage effects are expected to have a negligible impact on CMRO₂ quantified via the Fick Principle, even during non-steady state stimuli such as apnea.

Chapter 3: Rapid T₂- and Susceptometry-Based CMRO₂

Quantification with Interleaved TRUST (iTRUST)

3.1. Abstract

SBO and TRUST are two promising methods for quantifying CMRO₂, a critical parameter of brain function. We present a combined method, interleaved TRUST (iTRUST), which achieves rapid, simultaneous quantification of both susceptibility- and T₂-based CMRO₂ via insertion of a flow-encoded, dual-echo GRE (OxFlow) module within the T₁ recovery portion of the TRUST sequence. In addition to allowing direct comparison between SBO- and TRUST-derived Y_v values, iTRUST substantially improves TRUST temporal resolution for CMRO₂ quantification and obviates the need for a separate blood flow measurement following TRUST acquisition. iTRUST was compared directly to TRUST and OxFlow alone in three resting subjects at baseline, exhibiting close agreement with the separate techniques and comparable precision. These baseline data as well as simulation results support the use of two instead of the traditional four T₂ preparation times for T₂ fitting, allowing simultaneous quantification of susceptibility- and T₂-based Y_v (and CMRO₂) with three- and six-second temporal resolution, respectively. In 10 young healthy subjects, iTRUST was applied during a 5% CO₂ gas-mixture breathing paradigm. T₂-based Y_v values were lower at baseline relative to susceptibility (mean ± SD of 62.3 ± 3.1 vs. 66.7 ± 5.1 %HbO₂, P < 0.05), but increased more in response to hypercapnia. As a result, T₂-based CMRO₂ decreased from 140.4 ± 9.7 at baseline to 120.0 ± 9.5 μmol/100g/min during hypercapnia, a significant -14.6 ± 3.6% decrease, whereas susceptibility-based CMRO₂ changed insignificantly from 123.4 ± 18.7 to 127.9 ± 25.7, a 3.3 ± 9.7% change (P = 0.31). These differing results are in accord with previous studies applying the parent OxFlow or TRUST sequences individually, thus supporting the reliability of iTRUST but also strongly suggesting that a systematic bias exists between the susceptibility- and T₂-based Y_v quantification techniques.

3.2. Introduction

The human brain comprises only 2% of total body mass, but accounts for approximately 20% of total body oxygen consumption (1). Because the brain is almost entirely dependent on aerobic metabolism to meet its energetic demands, irreversible ischemic damage will result in minutes if oxygen delivery is disrupted. Unlike surrogate markers of metabolism such as CBF or BOLD fMRI signal, CMRO₂ provides a direct measure of brain oxygen consumption. CMRO₂ changes significantly over the course of neonatal development (109) and aging (110), and is altered in many of the most common neurologic diseases, including mild cognitive impairment (112) and Alzheimer's disease (34), Parkinson's disease (127), and multiple sclerosis (111). However, CMRO₂ is relatively stable across healthy subjects at baseline (66,101), and in response to physiologic challenges such as hypercapnia (87,124,141), hypoxia and hyperoxia (105), and apnea (135). Thus, CMRO₂ is an important quantity for understanding brain function in health and disease.

The gold standard for CMRO₂ quantification is triple-oxygen PET imaging (53), yet the technique is rarely applied in humans due to the radiation exposure and complexity of the protocol. Moreover, long scan times restrict PET to measuring resting-state CMRO₂. MRI provides a non-invasive, non-contrast alternative. During the past two decades, BOLD fMRI has been applied extensively to study neuronal activation in health and disease (148,149). However, BOLD signal does not provide a direct measure of brain oxygen metabolism, but rather reflects a complex interplay between CBF, CBV, and tissue properties such blood vessel diameter, in addition to CMRO₂ (150).

Recently, a number of MR-based approaches for direct quantification of cerebral Y_v have been proposed (60-67,90-92,98,99,121,122,128,141,151). In combination with PC-MRI or ASL CBF quantification, these techniques allow determination of CMRO₂ via the Fick Principle (10-12):

$$CMRO_2 = C_a \cdot tCBF \cdot (Y_a - Y_v) \quad [3.1]$$

where C_a is the arterial oxygen content of blood in $\mu\text{mol}/100\text{mL}$ and Y_a is the arterial oxygen saturation in $\%\text{HbO}_2$, which can be measured with pulse oximetry. Total CBF (tCBF) is typically reported in units of $\text{mL blood}/100\text{g brain tissue}/\text{minute}$, giving CMRO_2 in units of $\mu\text{mol}/100\text{g}/\text{minute}$.

Measurement of Y_v poses the most significant technical challenge in CMRO_2 determination. Techniques for Y_v quantification can be categorized based on the contrast mechanism – venous blood magnetic susceptibility (66,67,121,122,128), T_2 (61-65,98,99,141,151), T_2' (60,92), or T_2^* (BOLD) (64,91) – as well as spatial specificity – large-vessel/whole-brain (61,63,66,98,99,121,122,128,141,151), small-vessel/regional (62,67), or parenchymal/voxel-wise (60,64,65,90-92). Regional and voxel-wise approaches are clearly desirable due to the heterogeneous nature of brain functional activation and pathology. However, these techniques have scan times on the order of several minutes, precluding dynamic measurements, and tend to suffer from low SNR, requiring significant spatial averaging to achieve acceptable precision and thus negating the utility of regional or voxel-wise measurement. In comparison, techniques for whole-brain Y_v quantification are fast, robust, and easy to implement.

The two best-established methods for global Y_v quantification are TRUST (61) and SBO (SBO) (66). Both methods involve quantification of intravascular Y_v in the SSS, the largest cerebral venous drainage vessel, which, in combination with PC-MRI quantification of tCBF, can be used to determine CMRO_2 via **Equation 3.1**. In the case of TRUST, tCBF measurement requires a separate PC-MRI acquisition (101). However, because PC-MRI and SBO are both GRE sequences, they can be naturally combined into a single sequence, which we term OxFlow. This hybrid sequence was originally implemented via a two-slice-interleaved approach with CMRO_2 quantification temporal resolution of 25 seconds (66). Recently, addition of view-sharing and SSS-based estimation of tCBF improved OxFlow temporal resolution to three seconds, allowing study of the regulation of CMRO_2 in response to dynamic physiologic paradigms such as breath-hold apnea (135). Compared to OxFlow, TRUST has inherently lower temporal resolution, compounded by the need for a separate PC-MRI measurement to quantify CMRO_2 . Furthermore,

the relationship between T_2 , Y_v , and Hct is non-linear, and must be calibrated to both pulse sequence parameters and field strength. However, unlike SBO, TRUST is vessel geometry independent, less sensitive to partial volume effects, and does not require background phase removal.

A particularly important application of $CMRO_2$ quantification is investigating the metabolic response to hypercapnia. Hypercapnia is relevant to a number of common diseases, including asthma, chronic obstructive pulmonary disease, obstructive sleep apnea, and congestive heart failure. Furthermore, knowledge of the $CMRO_2$ response to hypercapnia is of substantial importance to functional imaging, where hypercapnia is routinely used for 'calibrating' the fMRI signal (59,81), often under the assumption that hypercapnia is isometabolic (i.e., does not affect $CMRO_2$). However, the $CMRO_2$ response to a hypercapnic stimulus remains controversial (117), with previous studies reporting a wide range of results from reduced, to unchanged, to increased $CMRO_2$. An early MRI study using T_2 -based to Y_v quantification reported an isometabolic response (141); however, $CMRO_2$ responses to mild and moderate hypercapnia were in different directions (5.0% and -6.8%, respectively) and based on a calibration plot derived from room temperature blood samples (152), potentially impacting the accuracy of in vivo T_2 quantification (116). Subsequently, both OxFlow and TRUST have been applied to study the $CMRO_2$ response to hypercapnia using similar cohorts and experimental protocols involving a 5% CO_2 gas-mixture delivery (87,124). While OxFlow data supported an isometabolic CO_2 response, the TRUST study found a significant $13.4 \pm 2.3\%$ (mean \pm standard error, $N = 14$) decrease in $CMRO_2$. This discrepancy is disconcerting given both the importance of understanding the $CMRO_2$ response to hypercapnia as well as the increasing application of TRUST and OxFlow in studying $CMRO_2$ responses to other stimuli and disease states. A recent study directly comparing resting TRUST- and SBO-derived Y_v values in the same cohort (153) found SBO and TRUST Y_v values to be correlated across subject, with TRUST Y_v values slightly lower (mean \pm SD of 63.2 ± 4.1 vs. 65.9 ± 3.3 %HbO₂, $P < 0.01$) (**Figure 3.1**). However, this baseline difference does not by itself explain

the discrepancy in the hypercapnia results, which depends on the relative change in Y_v in response to the stimulus.

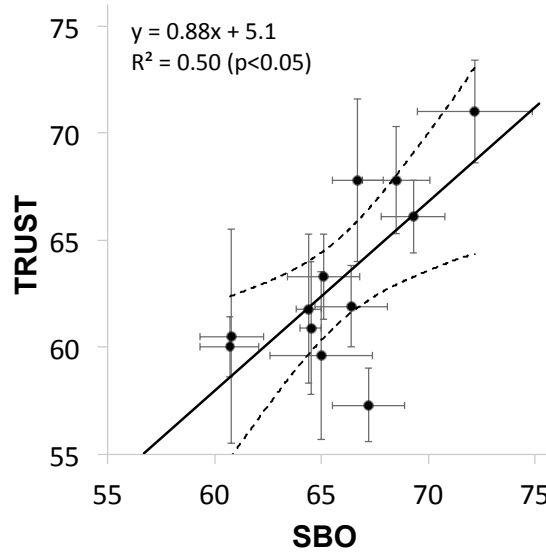


Figure 3.1: TRUST vs. SBO-derived Y_v in 10 healthy subjects (age 33 ± 6) at rest. Error bars indicate intrascan standard deviations over 10 repeated measures. The dashed lines denote the 95% confidence interval for the linear fit. Figure adapted from (153).

In this work, we propose a combined technique – termed interleaved TRUST (iTRUST) – whereby an OxFlow module is interleaved within the T_1 recovery period of the TRUST sequence. This approach has two distinct benefits. First, it obviates the need for separate, non-simultaneous measurement of tCBF following the TRUST acquisition, substantially improving TRUST temporal resolution for $CMRO_2$ quantification. Second, it allows for direct comparison of Y_v quantified via magnetic susceptibility and T_2 measurement of blood. Further temporal acceleration of TRUST is achieved by using fewer tag-control image pairs for T_2 fitting. Both the combination of the techniques as well as the use of fewer T_2 fitting points is validated in simulations and in vivo. The sensitivity of the technique to detect dynamic changes is demonstrated in response to breath-hold apnea. Finally, iTRUST is applied in a cohort of young healthy individuals during a CO_2 gas-mixture breathing paradigm with the goal of further investigating the potential disagreement between the TRUST and OxFlow techniques with regard to the hypercapnic $CMRO_2$ response.

3.3. Theory

3.3.1. Susceptometry-Based Quantification of Y_v (SBO)

SBO exploits the relative paramagnetism of deoxygenated versus oxygenated hemoglobin, which causes the susceptibility of blood relative to surrounding tissue, $\Delta\chi$, to be linearly related to Y_v :

$$\Delta\chi = Hct \left(\Delta\chi_{do} (1 - Y_v) + \Delta\chi_{oxy} \right) \quad [3.2]$$

where $\Delta\chi_{do}$ and $\Delta\chi_{oxy}$ are the experimentally determined volume susceptibility differences between fully oxygenated and deoxygenated erythrocytes and fully oxygenated erythrocytes and water, respectively. Values of $4\pi \times 0.273$ and $4\pi \times 0.008$ p.p.m. (SI units) are used for $\Delta\chi_{do}$ and $\Delta\chi_{oxy}$, based on ex vivo calibration experiments (116,118).

Blood susceptibility induces a local field offset, ΔB , which can be measured with a field mapping sequence as:

$$\Delta B = \Delta\phi / \gamma \Delta TE \quad [3.3]$$

where $\Delta\phi$ is the difference in phase accrual between echoes spaced apart by ΔTE in the blood versus surrounding reference tissue. By modeling the vessel of interest as an infinitely long, circular cylinder, the relationship between ΔB and $\Delta\chi$ can be calculated analytically:

$$\Delta B = \frac{1}{6} \Delta\chi B_0 (3 \cos^2 \theta - 1) \quad [3.4]$$

where θ is the vessel angle with respect to the main magnetic field, ΔB . Combining **Equations 3.2-3.4** allows determination of Y_v by measurement of $\Delta\phi$.

The SSS, the largest cerebral venous drainage vessel, is relatively long and straight when the subject is lying supine in the scanner, and therefore can be effectively approximated by the infinite cylinder model, despite its non-circular cross-section (66,123). The SSS has also been

shown to have a Y_v nearly identical to that in the internal jugular vein (63,101), making it an excellent surrogate for global venous Y_v . Furthermore, while field mapping of the internal jugular vein is complicated by the presence of trachea-induced susceptibility artifacts, the field local to the SSS is relatively homogenous.

3.3.2. Combination of SBO and PC-MRI for CMRO₂ Quantification (OxFlow)

SBO can be combined with PC-MRI blood flow quantification to allow simultaneous measurement of Y_v , tCBF, and, therefore, CMRO₂, from a single sequence. By adding flow-encoding to the same dual-echo GRE used for Y_v quantification, SSS blood flow (SSSBF) and Y_v can be quantified from data acquired in the same TR period. SSSBF can then be retrospectively up-scaled to tCBF based on a single measurement of the SSSBF:tCBF ratio at baseline (135).

In this study, OxFlow was implemented with a BRISK k-space sampling scheme, with one-quarter k-space acquired at each time point (154,155). BRISK provides reduced motion sensitivity compared to previous view-sharing implementations of OxFlow using Keyhole k-space sampling (135,136) (**Figure 3.2**).

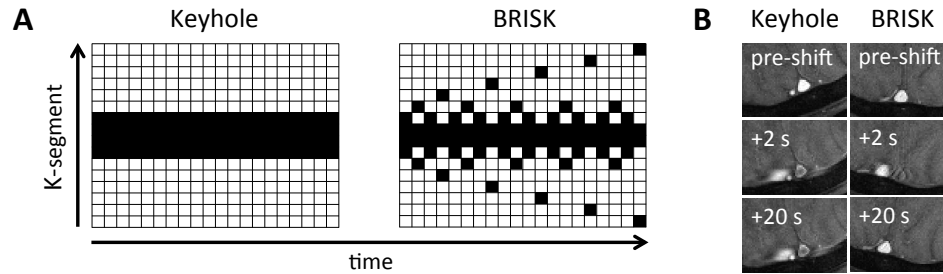


Figure 3.2: BRISK vs. Keyhole Cartesian view-sharing. (A) Keyhole and BRISK temporal k-space sampling strategies. In Keyhole, only inner k-space is continuously updated, with outer k-space supplied from a separately acquired, fully sampled reference image. In BRISK, the most inner k-space segments are updated most frequently, and full k-space images are reconstructed via interpolation, using the nearest acquired data for each segment. (B) Axial magnitude images of the SSS, before, 2 seconds (1 time point) after, and 20 seconds (10 time points) after a deliberate head shift. Because Keyhole assumes outer k-space does not change, it is highly sensitive to motion, whereas BRISK updates outer k-space periodically and thus resolves motion artifacts after several time points.

BRISK images were reconstructed by interpolating across time points using the nearest acquired data at each k-space segment, effectively resulting in a sliding window reconstruction with minimum window width of three seconds (inner 1/8th of k-space) and maximum window width of 60 seconds (outer 5/8th of k-space). Other OxFlow sequence parameters include: TR/TE₁/TE₂ = 14.2/6.5/11.5 ms, VENC = 40 cm/s, reconstructed matrix = 192×192, and resolution = 1.0×1.0×5.0 mm.

3.3.3. TRUST and Interleaved TRUST (iTRUST)

The TRUST pulse sequence uses a non-selective MLEV-16 CPMG T₂ preparation of varying effective echo time (eTE) – 0, 40, 80, and 160 ms – following either an 8 ms adiabatic hyperbolic secant pulse (bandwidth = 2214 Hz, thickness = 100 mm) to invert the blood magnetization (tag), or application of an equivalent off-resonance pulse without gradient (control). Similar in principle to ASL, tag-control subtraction of each eTE image pair isolates the venous blood signal. A non-selective 90° spoiler RF pulse is applied to reset the magnetization before each tag-control module (102). A two-compartment exchange model is used to relate Y_v to T₂:

$$1/T_2 = A + B \cdot (1 - Y_v) + C \cdot (1 - Y_v)^2 \quad [3.5]$$

where A, B, and C are Hct- and CPMG spacing (t_{CPMG})-dependent constants which have been determined from ex vivo blood samples (100). T₂ is quantified by mono-exponential fitting of SSS tag-control difference signals vs. eTE as:

$$\Delta S = S_0 e^{eTE \cdot (1/T_1 - 1/T_2)} \quad [3.6]$$

where S₀ is the difference signal at eTE = 0 and a T₁ value of 1.613 seconds is assumed for venous blood (102).

The TRUST sequence used in the present work follows that described in recent literature (102), with a TR of three seconds used to provide an optimal tradeoff between scan duration, accuracy, and precision, allowing a single Y_v value to be quantified every 24 seconds. Important differences

relative to the published sequence include insertion of a slice-selective saturation pulse 200 ms before EPI readout (prior to T_2 preparation) in order to better suppress static tissue signal (63,151), and use of a flow-compensated EPI readout with TE of 8 ms ($5/8^{\text{th}}$ partial Fourier readout). Flow compensation prevents flow velocity-dependent signal variations between tag and control images, which could lead to errors in the difference signals, especially in situations of rapidly changing flow (46). An alternative approach to avoiding these effects is use of a shorter TE achieved via parallel imaging (102), though this reduces SNR. Other TRUST sequence parameters include: $t_{\text{CPMG}} = 10$ ms, reconstructed matrix = 64×64 , and resolution = $3.4 \times 3.4 \times 5.0$ mm.

More than half of the duration of the TRUST sequence consists of dead time, required to allow blood signal to undergo sufficient T_1 recovery following global saturation before the next T_2 preparation. In iTRUST, this time is utilized to run an OxFlo module at the same location as the TRUST readout slice (**Figure 3.3**), beginning 350 ms after the saturation in order to capture the tissue signal approximately at its steady-state longitudinal magnetization. Besides the added OxFlo module, iTRUST is otherwise identical to TRUST.

It is important to note that the RF pulses played out during the OxFlo module only affect spins in the imaging slice, whereas spins relevant to T_2 -quantification are located outside the imaging slice in the labeling slab. Furthermore, because the OxFlo module is run during both tag and control, any effect on spins in the subsequently acquired EPI images used for T_2 quantification should be identical, and hence removed by tag-control subtraction. Likewise, the OxFlo GRE acquisition itself is unaffected by the TRUST sequence because it is acquired only after global magnetization reset.

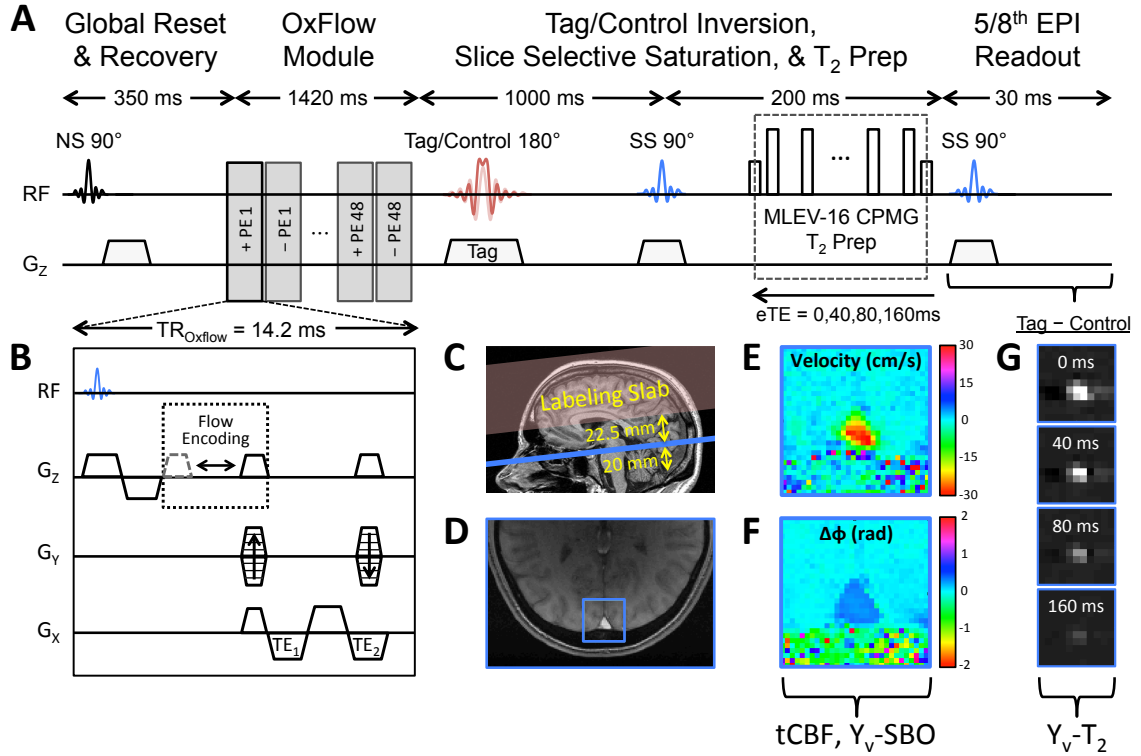


Figure 3.3: iTRUST pulse sequence and example images. (A) TRUST sequence diagram with (B) inset depicting the OxFLOW module inserted within the T₁ recovery period of the TRUST sequence. (C) Sagittal scout image indicating the relative positions of the labeling slab (red) and imaging slice (blue). (D) Magnitude image with square ROI indicating the position of the SSS. (E) Velocity map and (F) phase difference map of the SSS ROI from (D). (G) TRUST difference images for each eTE. Note that the spin histories of the OxFLOW module and TRUST sequence should not interact as they are isolated by the global spin reset and the spatial separation of the imaging slice and labeling slab. Figure from (86).

3.4. Methods

3.4.1. Human Subject Protocols

All human subject imaging protocols were approved by the University of Pennsylvania's Institutional Review Board, and subjects provided written informed consent prior to participation. Studies were performed on 10 healthy subjects (age 29 ± 5 years, range 24-42, six males and four females) using a 3T Siemens Tim Trio system (Siemens Medical Solutions, Erlangen, Germany) with a 12-channel (validation study and apnea study) or 32-channel (hypercapnia

study) receive-only head coil. A vendor-provided time-of-flight axial localizer scan was used for slice selection, and retrospectively to determine θ in **Equation 3.4**. Before each OxFlow or iTRUST acquisition, a two-slice-interleaved PC-MRI pulse sequence was run at the level of the internal carotid and vertebral arteries in the neck and the SSS in the head in order to determine the subject's SSSBF:tCBF ratio. OxFlow, TRUST, and iTRUST pulse sequences were programmed in SequenceTree (156).

At the end of each scanning session, a 1-mm-isotropic 3D T_1 -weighted MPRAGE (134) data set was acquired so that tCBF could be normalized per unit brain mass in each subject. Total brain volume was obtained using the BET tool in FSL (157), and converted to mass based on an average brain density of 1.05 g/mL (158). Total intracranial mass (gray matter, white matter, and CSF) rather than total parenchymal mass (gray matter and white matter) was used for normalization to facilitate comparison of CMRO₂ values with prior studies that did the same (66,101). It has recently been shown that inclusion of CSF volumes in flow normalization may bias toward underestimation of CMRO₂ in older individuals (110), though this is not a concern in the present study due to the relatively young age of the subjects.

3.4.2. Validation Study

To test whether the combination of OxFlow and TRUST causes a bias in the measurements of either sequence, equivalent OxFlow, TRUST, and iTRUST sequences were run back to back for four minutes each in three subjects (age 29 ± 3 years, range 26-34, two males and one female). This protocol corresponds to 10 repetitions of TRUST and iTRUST with 24-second temporal resolution, and 80 repetitions of OxFlow with three-second temporal resolution. For the OxFlow only sequence, TR was increased to 31.25 ms to use the entire three-second time frame with sequence parameters otherwise equal to the iTRUST-inserted OxFlow module.

For each subject, T_2 -based Y_v (Y_v-T_2) was derived from TRUST and iTRUST data, and SBO-based Y_v (Y_v-SBO) and tCBF from iTRUST and OxFlow data. Differences in parameter values across subjects were compared between techniques – TRUST vs. iTRUST for Y_v-T_2 , OxFlow vs.

iTRUST for Y_v -SBO and tCBF – to determine any potential bias in the interleaved approach relative to the separate techniques. Further, T_2 values obtained from the iTRUST data were recalculated using only the 0 and 80 ms eTE image pairs to determine any bias caused by using fewer eTEs. T_2 fitting with two eTEs has previously been demonstrated at 7T field strength (159), where the short T_2 value of blood precludes the use of longer T_2 preparations.

3.4.3. Simulations

The use of fewer eTE image pairs was further explored by simulating TRUST difference signals with a blood T_2 value of 72 ms, corresponding to typical physiologic values of $Y_v = 65\% \text{HbO}_2$ and $\text{Hct} = 0.40$, with noise added corresponding to the typically observed SNR range of our acquired TRUST data (SNR = 20-80). This SNR range is similar to that reported in previous studies (102). Exponential fitting was performed and Y_v values were determined from the published calibration curve (100) using all four (0, 40, 80, 160 ms), three (0, 40, and 80 ms), or two (0 and 80 ms) eTEs. RMSE relative to the true Y_v of 65 %HbO₂ was quantified as a function of SNR and number of eTEs used.

3.4.4. Apnea Study

To evaluate the sensitivity of the iTRUST technique to detect dynamic changes in flow, Y_v -SBO, and Y_v - T_2 , a breath-hold challenge was conducted in one healthy subject (age 28 years, male). iTRUST was run with two eTEs (0 and 80 ms) during a paradigm consisting of two minutes baseline, one-minute breath-hold after inhalation, and two minutes recovery. Y_v -SBO and tCBF were quantified every three seconds. Y_v - T_2 values were quantified with sliding-window reconstruction using all adjacent difference image pairs, yielding six-second temporal resolution from 12-second data windows. The mean and standard deviation of the difference between time matched Y_v - T_2 and Y_v -SBO values was quantified across all time points, and compared by paired two-sample Student's t-tests.

3.4.5. Hypercapnia Study

In 10 subjects, iTRUST comprising only two eTEs (0 and 80 ms) was applied during a hypercapnia paradigm to determine whether differences exist in the $CMRO_2$ as determined via T_2 - versus susceptibility-based quantification of Y_v . A two-way non-rebreathing T-valve (2700 Series, Hans Rudolph, Inc., Kansas City, MO, USA) was used to deliver 5% CO_2 in room air for five minutes via a 100 L Douglas bag. Room air was delivered five minutes before and after hypercapnia, and MRI data were collected continuously for the entire 15 minutes. Y_a and heart rate (HR) were monitored with pulse oximetry, and end-tidal CO_2 ($EtCO_2$) and respiratory rate (RR) with capnography (Expression, Invivo Research Inc., Orlando, FL, USA).

tCBF, Y_v -SBO, and SBO-based $CMRO_2$ ($CMRO_2$ -SBO) parameter values were determined from the OxFlow data at three-second temporal resolution, and Y_a values were sampled at three-second intervals to match the MRI data. Y_v - T_2 values were quantified every six seconds from the EPI data with sliding-window reconstruction. tCBF and Y_a values were interpolated to the corresponding Y_v - T_2 time points to determine T_2 -based $CMRO_2$ ($CMRO_2$ - T_2) values every six seconds. For each parameter, means and standard deviations were quantified across the baseline (0-5 minutes) and steady-state hypercapnia (7.5-10 minutes) periods, and used to determine percent changes in response to hypercapnia. Changes in $CMRO_2$ - T_2 and $CMRO_2$ -SBO in response to hypercapnia were evaluated with one-sample Student's t-tests.

3.4.6. Image Analysis

All image reconstruction was performed with in-house-written MATLAB (Mathworks, Natick, MA) scripts. BRISK-sampled raw OxFlow data, whether acquired alone or as part of an iTRUST sequence, were first reordered to create full k-space images corresponding to each three-second time point. To determine tCBF, the phase difference between positive gradient-moment flow-encoded and flow-compensated images acquired at TE_1 were used to generate velocity maps, and SSSBF was obtained by integrating velocity across the vessel cross-sectional area. Data from the two-slice-interleaved PC-MRI sequence used to determine the SSSBF:tCBF ratio were

processed analogously. This ratio was then used to upscale the dynamically acquired SSSBF data to determine tCBF.

For Y_v -SBO determination, a raw phase difference map was generated from images acquired at TE_1 and TE_2 of the flow-compensated OxFlo interleave. Low spatial frequency bulk susceptibility effects were removed via second-order polynomial fitting of the induced field in the surrounding brain tissue (126). The average phase difference, $\Delta\phi$, was determined between pixels entirely within the SSS (i.e., without any tissue partial voluming) and pixels in a reference region of brain tissue surrounding the SSS approximately one vessel-radius in width and located one vessel-radius from the SSS border, allowing determination of Y_v -SBO from **Equations 3.2-3.4**.

TRUST or iTRUST EPI data for T_2 -determination were first reconstructed and corrected for N/2 ghosting. Difference images were produced for each eTE via tag-control subtraction. As previously described (61), the four brightest pixels in the SSS were selected for T_2 fitting, using a weighted least-squares fit calculated by the MATLAB function `lsqnonlin`.

3.5. Results

Across the three subjects scanned at baseline, quantified Y_v and tCBF values were consistent with previous reports (66,101), and mean absolute bias between TRUST and iTRUST Y_v -T₂ (**Figure 3.4a**) and between OxFlow and iTRUST Y_v -SBO (**Figure 3.4b**) and tCBF (**Figure 3.4c**) values were small. These values likely represent an upper bound on any true bias, as they also include contributions from measurement noise and true physiologic variation over the scan duration. Standard deviations of the parameter values varied across subjects, but were similar between techniques, suggesting precision of the combined iTRUST sequence to be comparable to the separate TRUST and OxFlow sequences.

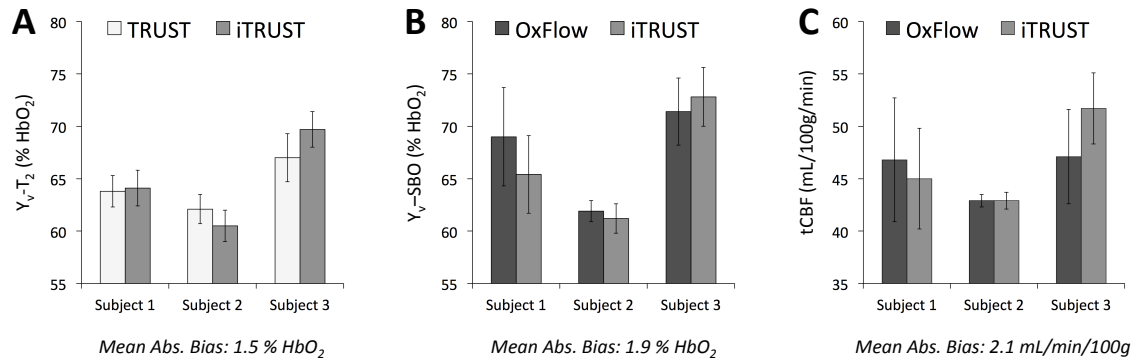


Figure 3.4: TRUST, OxFlow, and iTRUST parameter values acquired sequentially for four minutes each in three resting subjects. (A) TRUST vs. iTRUST Y_v -T₂ values. (B) OxFlow vs. iTRUST Y_v -SBO values. (C) OxFlow vs. iTRUST tCBF values. Mean absolute bias is the absolute value of the bias between techniques, averaged across all time points and subjects. Error bars indicate ± 1 SD across the N = 10 (A) or N = 80 (B and C) data points collected in each four-minute acquisition. Figure from (86).

In **Figure 3.5**, iTRUST Y_v-T_2 values are shown based on T_2 fitting using all four (0, 40, 80, and 160 ms) or just two (0 and 80 ms) eTE difference signals. The mean \pm SD difference between the two sets of values was small at 0.2 ± 1.8 %HbO₂ ($P = 0.65$). The 95% confidence interval for the linear least-squares regression line includes the line of identity, further indicating that no significant bias is introduced by using two instead of four eTEs. Y_v-T_2 variability was slightly larger when using two versus four eTEs (subject-averaged SDs of 2.6 and 1.6 %HbO₂, respectively). However, this difference is largely eliminated if RMSEs are scan-time normalized, that is, after multiplying by $\sqrt{\text{number eTEs}}$ used for fitting. These data support the use of two eTEs in subsequent iTRUST experiments.

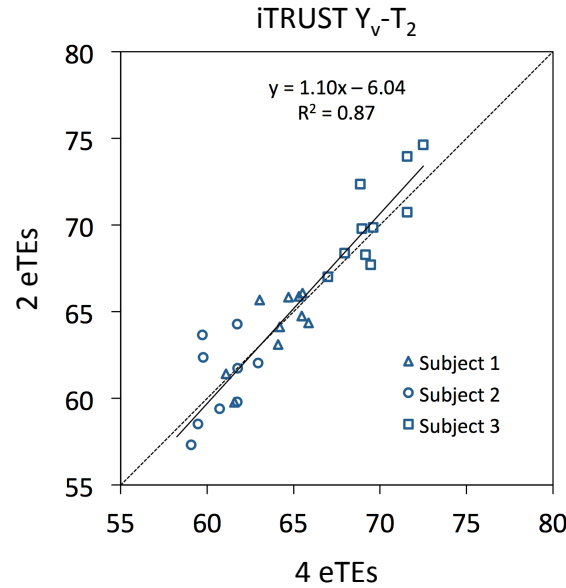


Figure 3.5: Scatter plot of iTRUST Y_v-T_2 values fitted using all four (0, 40, 80, and 160 ms) vs. only two (0 and 80 ms) eTEs from the same data. The 30 data points represent 10 repeat measures from each of three subjects. The linear least-squares regression line for all data points (solid line) is shown alongside the line of identity (dotted line). 95% confidence intervals for the slope [0.93,1.25] and intercept [-16.4, 4.3] of the linear fit contain 1 and 0, respectively, indicating no statistically significant bias between the four and two eTE Y_v-T_2 values. Figure from (86).

Figure 3.6 shows RMSEs for Y_v-T_2 values across the typical TRUST SNR range, both absolute (6a) and scan-time normalized (6b). Even before normalization, three and two eTEs result in less error than four eTEs. Normalized for scan time, both three and two eTEs perform significantly better than four eTEs, with ≈ 30 -45% reduction in RMSE across the SNR range.

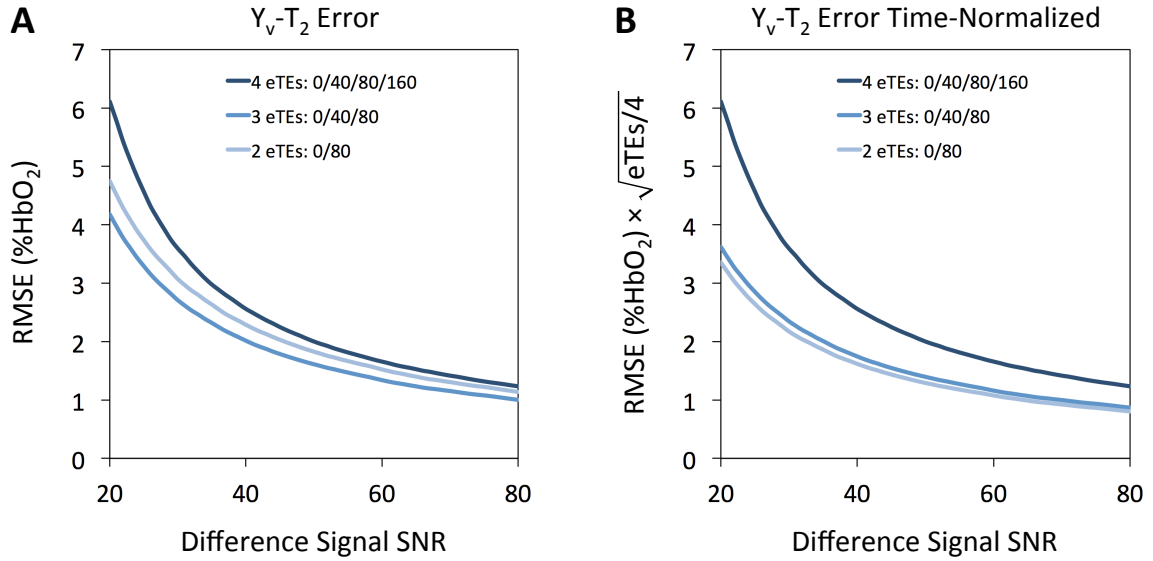


Figure 3.6: Simulation of expected Y_v-T_2 error vs. the number of eTEs used for T_2 fitting. (A) RMSE in Y_v-T_2 vs. TRUST difference signal SNR for four, three, or two eTEs. (B) RMSE normalized to acquisition time. Simulations were performed for $N = 1000$ virtual images for each SNR value, incremented by an SNR value of 1. Figure from (86).

iTRUST with two eTEs was evaluated in response to breath-hold apnea to test the ability of the technique to detect dynamic physiologic processes. A time-course plot of the extracted parameter values (**Figure 3.7**) demonstrates the expected apneic response of increased Y_v and tCBF (135). Y_v -SBO and Y_v - T_2 values match closely, with Y_v -SBO values higher by an average of 1.5 ± 3.0 %HbO₂ ($P < 0.01$).

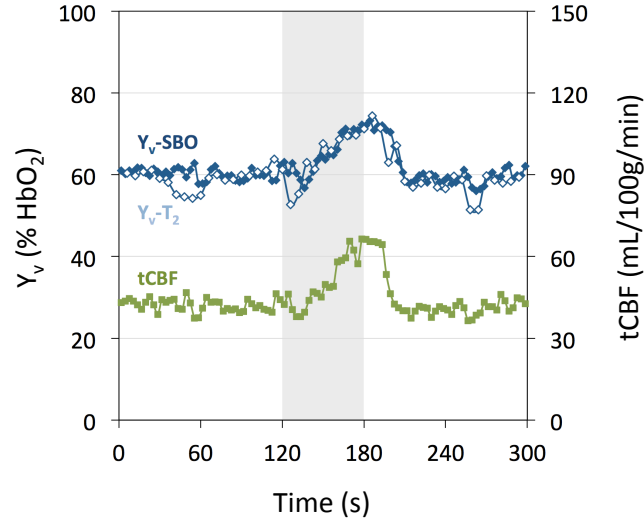


Figure 3.7: iTRUST parameter values in response to a 60-second breath-hold in a single subject. T_2 fitting with two eTEs and application of sliding window reconstruction yields Y_v - T_2 temporal resolution of six seconds. Y_v -SBO and tCBF temporal resolution is three seconds. Gray shading indicates the apnea period. Figure from (86).

All 10 subjects were able to successfully complete the hypercapnia paradigm. Average brain volume, Hct, and SSS angle (θ) were 1468 ± 77 mL, 0.43 ± 0.04 , and $15.2 \pm 5.0^\circ$. On average, the SSSBF:tCBF ratio was 0.48 ± 0.03 , in line with previous studies (135). Subject-averaged time-course plots of physiologic parameters measured via pulse oximetry (Y_a , HR) and capnography (EtCO₂, RR) are displayed in **Figure 3.8**.

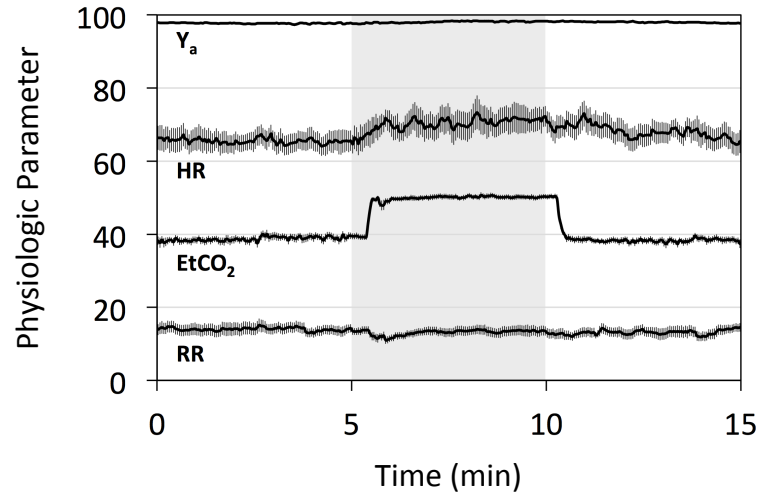


Figure 3.8: Subject-averaged time-course plots of physiologic parameters measured via pulse oximetry (Y_a , HR) and capnography (EtCO₂, RR). Gray shading indicates the hypercapnia period. Error bars indicate standard errors (N = 10). Comparing average baseline (0-5 minutes) and steady-state hypercapnia (7.5-10 minutes) values across subjects, significant increases were observed in EtCO₂ ($P < 0.0001$), Y_a ($P < 0.01$), and HR ($P < 0.05$). RR did not show a significant change ($P = 0.64$). Figure from (86).

Figure 3.9 displays a representative subject time-course plot of all MRI-derived parameters (and Y_a) in absolute physiologic units (9a), subject-averaged plots of both absolute parameter values (9b) and baseline-normalized parameter values (9c), and a scatter plot comparing Y_v -SBO and Y_v -T₂ values across all subjects and time points (9d).

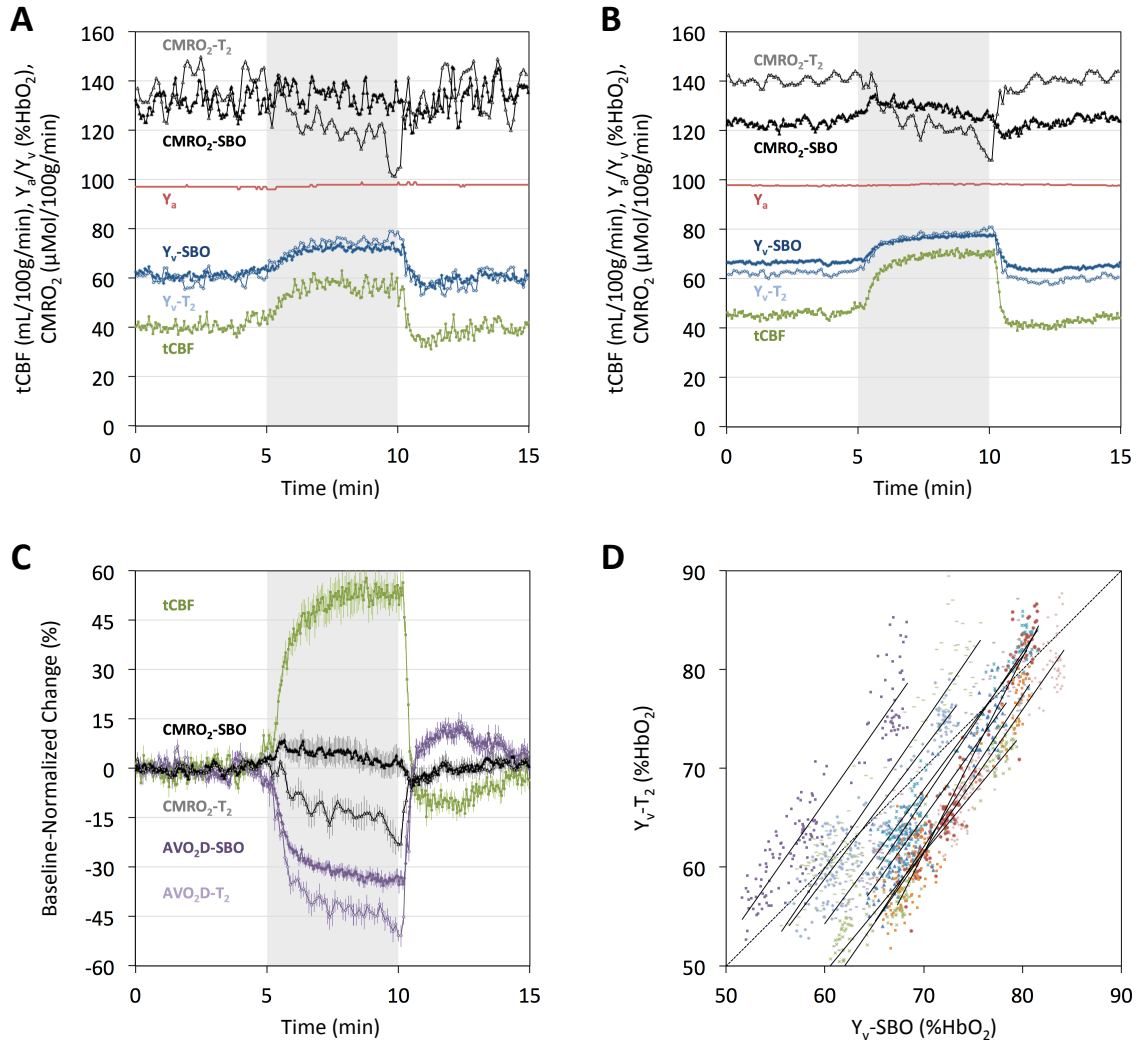


Figure 3.9: iTRUST-derived parameter values in response to five minutes of 5% CO₂ gas-mixture breathing. (A) Time-course plots of absolute parameter values from (A) a representative subject and (B) averaged across all 10 subjects. (C) Subject-averaged parameter values normalized to average baseline values, with error bars indicating standard errors (N = 10) at each time point. In all time-course plots, tCBF, Y_a , Y_v -SBO, AVO₂D-SBO, and CMRO₂-SBO temporal resolution is three seconds, and Y_v -T₂, AVO₂D-T₂, and CMRO₂-T₂ temporal resolution is six seconds. Gray shading indicates the hypercapnia period. (D) Scatter plot of time-matched Y_v -SBO and Y_v -T₂ values across all subjects and time points (N = 1490), with different symbols/colors denoting individual subjects. Linear least-squares regression lines are plotted for each subject (solid lines), as well as the line of identity (dotted line). Mean slope and r^2 values of the regression lines across subjects are $\beta = 1.47 \pm 0.20$ and $r^2 = 0.90 \pm 0.02$. Figure from (86).

Parameter values were observed to reach a steady state after approximately 2.5 minutes of hypercapnia. Average baseline (0-5 minutes) and steady-state hypercapnia (7.5-10 minutes) values are displayed in **Table 3.1**. EtCO₂, tCBF, Y_v-SBO, and Y_v-T₂ all increased significantly in response to hypercapnia ($P < 0.0001$). Subject-averaged CVR was $4.6 \pm 0.9\%$ tCBF/mmHg EtCO₂, in line with previous results (66,141).

Parameter	Baseline (0-5 min)	CO ₂ (7.5-10 min)	Change (%)	P-value
EtCO ₂ (mmHg)	38.5 ± 2.9	50.1 ± 2.1	30.5 ± 5.5	< 0.0001
Y _a (%HbO ₂)	97.7 ± 0.6	98.3 ± 0.7	0.6 ± 0.6	< 0.01
tCBF (mL/100g/min)	45.7 ± 6.0	70.1 ± 11.4	53.0 ± 12.7	< 0.0001
Y _v -SBO (%HbO ₂)	66.7 ± 5.1	77.2 ± 4.8	15.9 ± 2.8	< 0.0001
Y _v -T ₂ (%HbO ₂)	62.3 ± 3.1	78.4 ± 3.5	25.8 ± 3.7	< 0.0001
AVO ₂ D-SBO (%HbO ₂)	31.1 ± 4.8	21.1 ± 4.4	-32.5 ± 4.7	< 0.0001
AVO ₂ D-T ₂ (%HbO ₂)	35.4 ± 2.9	19.9 ± 3.0	-43.8 ± 5.9	< 0.0001
CMRO ₂ -SBO (μmol/100g/min)	123.4 ± 18.7	127.9 ± 25.7	3.3 ± 9.7	0.31
CMRO ₂ -T ₂ (μmol/100g/min)	140.4 ± 9.7	120.0 ± 9.5	-14.6 ± 3.6	< 0.0001

Table 3.1: Summary of hypercapnia paradigm parameter values derived from pulse oximetry, capnography, and iTRUST MRI in 10 subjects. Parentheses indicate the standard deviations of parameter values across subjects. P-values are based on one-sample Student's t-tests of the percent changes from baseline to hypercapnia. Table adapted from (86).

Y_v-T₂, although lower than Y_v-SBO at baseline, increased more during hypercapnia. As a result, in response to hypercapnia CMRO₂-SBO did not change significantly ($3.3 \pm 9.7\%$, $P = 0.31$), whereas CMRO₂-T₂ decreased substantially ($-14.6 \pm 3.6\%$, $P < 0.0001$). Following cessation of apnea, tCBF and Y_v undershot before gradually returning to baseline. CMRO₂ values during the end-recovery period (12.5-15 minutes) were not significantly different from baseline values ($P = 0.36$ and $P = 0.33$ for CMRO₂-SBO and CMRO₂-T₂, respectively).

3.6. Discussion

3.6.1. Validation of iTRUST

Because changes in flow and Y_v tend to oppose each other both at baseline and in response to stimuli, it is critical to measure these two quantities simultaneously to most accurately determine CMRO₂. This is especially important during physiologic stimuli, where temporal mismatch between Y_v and flow quantification could lead to significant errors. iTRUST makes such

simultaneous measurement, previously achievable only with susceptibility-based CMRO₂ approaches, possible for T₂-based CMRO₂ quantification as well.

Combination of the TRUST and OxFlo techniques in iTRUST did not significantly impact the accuracy or precision of the quantified parameters (**Figure 3.4**). This is expected, as the OxFlo and T₂-quantification portions of the pulse sequence are separated in such a way that they should not affect one another's spin histories. While less time is available for OxFlo measurement in iTRUST than OxFlo alone for a given temporal resolution (1420 ms versus 3000 ms in this study), this did not appear to impact the precision of the OxFlo data as evidenced by similar standard deviations for iTRUST and OxFlo derived parameters (**Figures 3.4b-c**).

3.6.2. T₂-Based CMRO₂ Temporal Resolution

Previous implementations of TRUST had a temporal resolution for CMRO₂ quantification of several minutes (103), compared to as little as three seconds for OxFlo (135). This is partially due to the usual acquisition of three TRUST averages (requiring $3 \times 24 = 72$ seconds) and measurement of each arterial inflow vessel with a separate 30-second PC-MRI measurement, which has been demonstrated to produce accurate and reproducible CMRO₂ measurements (103). While this approach is optimal when a single CMRO₂ measure of baseline physiology is the objective, it does not allow for quantification of dynamic changes in T₂-based Y_v/CMRO₂.

iTRUST increases CMRO₂-T₂ temporal resolution to as little as six seconds via insertion of flow quantification within the T₁ recovery period and use of two eTEs with sliding window reconstruction. These modifications may also improve measurement precision. For instance, rapid measurement of SSSBF is achieved more easily than quantification of tCBF in the neck arteries, due to the sagittal sinus' larger size, less pulsatile flow, and fixed position in the scanner even during swallowing, breath-hold, or gas-mixture breathing manipulations that can complicate flow quantification in the neck arteries. Upscaling this dynamically acquired SSSBF to tCBF only requires a single high-quality PC-MRI acquisition before or after accelerated SSSBF-only

measurement, since the SSSBF:tCBF ratio has been observed to remain fixed in response to blood flow changes (135).

Simulation results (**Figure 3.6**) suggest that inclusion of a 160 ms eTE difference image actually reduces T_2 estimation precision due to its relatively low SNR. For iTRUST at 3T, T_2 measurement based on two eTEs performs slightly better than three eTEs after normalization for scan time differences. This is because an eTE of 80 ms most closely matches the physiologic T_2 range (60-100 ms). In vivo measurements at baseline suggest a slightly greater Y_v variation when retrospectively using two vs. four eTEs for T_2 fitting (SDs of 2.6 vs. 1.6 %HbO₂, respectively). However, this greater variation likely reflects some degree of sensitivity to true physiologic fluctuations – absent in the simulation data – which is more significantly removed through averaging when using all four eTEs for fitting. One limitation of using only two eTEs is that confidence intervals for the exponential fitting (and therefore Y_v) cannot be derived based on the regression of the exponential fit.

3.6.3. Hypercapnia Study

Parameter values quantified from the hypercapnia data were in good agreement with previous studies using TRUST or OxFlow independently, both in terms of resting state values (66,101) and changes in response to hypercapnia (87,124). Specifically, hypercapnia caused significant reduction in CMRO₂- T_2 ($-14.6 \pm 3.6\%$, mean \pm SD), similar to the original TRUST study (87) ($-13.4 \pm 8.6\%$, mean \pm SD, calculated from the reported standard error with $N = 14$), and also a non-significant change in CMRO₂-SBO ($3.3 \pm 9.7\%$, mean \pm SD), similar to the original OxFlow study (124). It was suggested (124) that the negative hypercapnic response observed with TRUST could have been biased due to flow measurement in the SSS, rather than in the neck arteries as was done with OxFlow. However, the present study used only SSS-based flow quantification, yet achieved results consistent with both previous studies (87,124). This consistency lends additional support to the use of SSS-based quantification of tCBF, a critical requirement for obtaining high temporal resolution CMRO₂ quantification with OxFlow and iTRUST. It also strengthens confidence that the modifications involved in the combined iTRUST

sequence (including the use of 2 eTEs for T_2 fitting) does not bias Y_v - T_2 quantification relative to the parent TRUST sequence. Most strikingly, it implies that the observed bias between Y_v - T_2 and Y_v -SBO values – both in terms of the baseline offset and relative changes in response to hypercapnia – is not due to random error, differences in experimental protocols, or differences in subject populations, but rather a systematic bias between the techniques.

Average baseline Y_v - T_2 values were observed to be significantly lower than Y_v -SBO values (62.3 ± 3.1 vs. 66.7 ± 5.1 %HbO₂, respectively, $P < 0.05$), consistent with another recent study (153). Longer TRUST EPI readouts have been shown to cause a systematic underestimation of T_2 (and therefore Y_v), especially at lower SNR. This effect was hypothesized to be caused by variations in blood flow, and led the authors to recommend use of a shorter (3 ms) EPI TE via application of parallel imaging (46). While the present study used a longer TE (8 ms), the slice-select gradient was first moment-compensated. This should prevent signal differences due to varying degrees of intravoxel dephasing in tag/control images acquired at different blood flow velocities. Furthermore, if a flow velocity-dependent bias did exist, the proposed Y_v - T_2 underestimation would be expected to get worse at higher Y_v values due to the accompanying CBF and heart rate increase during hypercapnia. In fact, the opposite trend was observed, with Y_v - T_2 values rising significantly more than Y_v -SBO values during the hypercapnic stimulus, regardless of the baseline offset between Y_v - T_2 and Y_v -SBO. This is illustrated by the subject specific regression lines in **Figure 3.9d**, all of which had slopes significantly greater than unity ($\beta = 1.47 \pm 0.20$, $P < 0.0001$ for $H_0: \beta = 1$).

As recently described by Xu et al. (160), a flow-dependent error in Y_v -SBO values could potentially arise due to phase accumulation as venous blood travels through an inhomogeneous B_0 field. This flow-dependent phase accumulation will increase quadratically with echo time and linearly with the dot product between the flow velocity and the background field gradient. Were the background field gradient direction similar in each subject, it could cause a systematic bias toward flow-dependent over- or under-estimation of Y_v -SBO. However, this effect alone cannot explain the observed bias between Y_v - T_2 and Y_v -SBO values, as it would predict the bias to

increase in magnitude with increasing flow velocity, whereas the observed bias reverses direction between the low flow (baseline) and high flow (hypercapnia) states. Furthermore, for the pulse sequence parameters used, quantitative evaluation suggests the maximum possible error due to flow-dependent phase accumulation is small (see Appendix, **Section 3.8**).

In addition to the aforementioned flow effects, another likely source of the observed discrepancy is an error in the calibration of one or both techniques – that is, the values of the constants in the model equations. However, the susceptibility model (**Equation 3.2**) is considerably simpler, with only two calibration constants – $\Delta\chi_{\text{do}}$ and $\Delta\chi_{\text{oxy}}$ – defining a linear relationship between measured phase, Hct, and Y_v . The values of these constants have been validated theoretically (116) and experimentally (116,118) with excellent agreement. In contrast, TRUST requires calibration of a quadratic equation (**Equation 3.5**) with six linear coefficients (100). This calibration equation is based on a two-compartment exchange model, which may be less appropriate than an alternative diffusion-based model (161). Furthermore, unlike SBO, T_2 -based Y_v quantification has a complex dependence on field strength and pulse sequence parameters (RF inversion pulse, t_{CPMG}).

3.6.4. Applications of iTRUST

In this work, we were interested in directly comparing T_2 - and susceptometry-based Y_v/CMRO_2 values; however, iTRUST could also be used specifically as a high temporal resolution T_2 -based CMRO_2 quantification technique. In this case, a single rather than dual-echo PC-MRI sequence module could be used, allowing for an increase in TR or reduction in the required view-sharing factor. Such a technique could be applied to CMRO_2 quantification in the jugular vein, which is less well suited to SBO because of trachea-induced susceptibility artifacts.

A potential clinical application of iTRUST is the assessment of CVR, the ability of the brain to dynamically increase flow in response to a vasodilatory challenge such as hypercapnia or breath-hold apnea. Reduced CVR is strongly correlated with increased stroke risk (162) and associated with lower cognitive performance in subjects with mild cognitive impairment and Alzheimer's disease (163). While CVR has typically been assessed in terms of blood flow changes only,

iTRUST and similar techniques for rapid CMRO_2 quantification (135) allow multi-parametric assessment of the brain's response to stimuli. Because CMRO_2 is a more direct reflection of oxygen supply and demand, CVR assessed in terms of CMRO_2 may provide a more meaningful index of neurovascular dysfunction than traditional flow-based CVR.

The described approach of inserting a fast imaging sequence within a longitudinal signal recovery period has applications beyond iTRUST. T_2 -relaxation-under-phase-contrast (TRU-PC), which uses phase-contrast rather than tag-control isolation of venous blood (62), and which can probe vessels with diameters as small as one mm, contains an equivalent signal waiting period as in TRUST. Addition of flow quantification within TRU-PC would provide a means of quantifying oxygen flux rather than simply oxygen saturation in small regional vessels not suitable to SBO. An interleaved approach similar to iTRUST has been used to quantify perfusion, Y_v , and T_2^* (termed PIVOT) via insertion of a multi-echo GRE within the post-label delay (PLD) of a pulsed ASL sequence (164). The technique allowed simultaneous measurement of all three parameters with two-second temporal resolution during a reactive hyperemia paradigm in the leg. Such combination of perfusion and Y_v quantification may also provide a method for improved BOLD fMRI calibration, as suggested in recent work by Driver et al. (165).

3.7. Conclusions

We presented a novel technique, iTRUST, for combined susceptibility- and T_2 -based quantification of CMRO_2 at high temporal resolution. Simulations and in vivo evaluations demonstrate that iTRUST has comparable precision and accuracy relative to the traditional uncombined methods. In addition, iTRUST provides significantly improved temporal resolution for T_2 -based CMRO_2 quantification. In summary, iTRUST is a promising method for dynamic assessment of CMRO_2 , and offers a unique approach for evaluating and comparing susceptibility- and T_2 -based CMRO_2 quantification techniques.

3.8. Appendix: Analysis of Flow-Dependent Error in SBO

Following Equation 2 in (160), $\Delta\phi$ in **Equation 3.3** can be written as:

$$\phi = \psi + \gamma\Delta B(\mathbf{r})TE - \frac{1}{2}\gamma\mathbf{v}(\mathbf{r}) \cdot \nabla(\Delta B(\mathbf{r}))TE^2 \quad [3.7]$$

where ψ is the initial phase after RF excitation, and \mathbf{r} and \mathbf{v} are the position and velocity, respectively, of a spin isochromat. **Equation 3.7** assumes that from spin excitation until the largest TE, the isochromat moves with constant velocity along a path with a linear field gradient, a reasonable assumption given the small distance traveled by a spin in time TE. Thus, the measured phase difference between TE_1 and TE_2 will be:

$$\Delta\phi = \gamma\Delta B(\mathbf{r})(TE_2 - TE_1) - \frac{1}{2}\gamma(\mathbf{v}(\mathbf{r}) \cdot \nabla B(\mathbf{r}))(TE_2^2 - TE_1^2) \quad [3.8]$$

The infinite cylinder model used in SBO requires isolating the first (linear) phase term from the second (quadratic) phase term. In (160), this is accomplished through a quadratic fitting procedure, the “adaptive quadratic fit”. However, such fitting is not possible when only two echoes are acquired as in SBO. Instead, we consider the fractional error (ε) in the derived $\Delta\phi$ resulting from the quadratic term, which is approximately the same as the resultant fractional error in the derived OEF ($1-Y_v$):

$$\varepsilon = (\Delta\phi_{\text{measured}} - \Delta\phi_{\text{linear}}) / \Delta\phi_{\text{linear}} = -\frac{(\mathbf{v}(\mathbf{r}) \cdot \nabla B(\mathbf{r}))}{\Delta B(\mathbf{r})} \cdot \frac{TE_1 + TE_2}{2} \quad [3.9]$$

where $\Delta\phi_{\text{measured}}$ is the measured phase difference and $\Delta\phi_{\text{linear}}$ is the phase difference due to only the linear term (what would ideally be measured to generate the correct value for Y_v). **Equation 3.9** demonstrates that the fractional error will be linear with the spin velocity, the gradient of the field along the path of the spin, and average echo time. Considering the echo times used for SBO

in this study (6.5 and 11.5 ms) and a “worst case scenario” of a flow velocity equal to the VENC (40 cm/s), the error is:

$$\varepsilon = 0.36 \frac{-\mathbf{v}(\mathbf{r}) \cdot \nabla B(\mathbf{r})}{\Delta B(\mathbf{r})} \quad [3.10]$$

where the field gradient is in units of Tesla/cm. Thus, if the field gradient along a 1 cm path of the spin is equal to the field difference between the vessel and surrounding tissue, $1-Y_v$ will be underestimated by 36%, a significant error. Fortunately, for properly chosen SBO slice locations in the SSS, field maps generated at sequential slices along the path of the SSS suggest field gradients approximately an order of magnitude smaller than this. Thus, a value of several percent is a reasonable upper bound for error due to the quadratic phase term. However, this analysis highlights the critical need to select an ideal slice location for SBO, and the importance of shimming prior to SBO. It also provides motivation for minimizing the TE values as much as possible while maintaining sufficient phase contrast. Detailed investigation of this potential source of error should be explored in future work by applying a quadratic phase model – the “adaptive-quadratic fit” as described in (160) – to an SBO sequence with several rephased echoes and longer echo times.

Chapter 4: BOLD Calibration with Interleaved Susceptometry-Based Oximetry and Phase-Contrast Flow Quantification

4.1. Abstract

BOLD calibration is a promising approach for improving the interpretability and reproducibility of fMRI. However, current calibration methods based on hypercapnia and hyperoxia gas-mixture breathing have significant limitations. Here, we present a new 'Y_v-based' BOLD calibration model and accompanying Ox-BOLD pulse sequence. This Y_v-based model requires measurement of whole-brain Y_v and tCBF in addition to voxel-wise mapping of CBF and BOLD signal. These various parameters are measured simultaneously with Ox-BOLD, which interleaves the rapid, GRE-based OxFlow method for global Y_v and tCBF quantification with a BOLD-calibration-optimized dual-echo pseudo-continuous ASL (pCASL) sequence for mapping CBF and BOLD signal. Both single and multi-slice versions of the sequence are applied to hypercapnia and hyperoxia gas-mixture breathing in healthy subjects. The resulting calibration M-maps compare favorably to those produced from the traditional Davis model using the same data, with considerably fewer non-physiologic M-values and more plausible anatomic contrast.

4.2. Introduction

In BOLD fMRI experiments, it is assumed that BOLD signal changes reflect neuronal activation spatially and temporally. This correspondence has been demonstrated by animal experiments involving simultaneous BOLD fMRI and intracortical EEG recordings (26). However, as discussed in **Chapter 1**, because BOLD signal changes are primarily driven by vascular processes (i.e., CBF changes), BOLD signal is temporally delayed and dispersed, and spatially broadened relative to underlying neuronal activity (27,28). Furthermore, BOLD signal changes have been shown to exhibit large intra- and inter-subject variability in response to the same task repeated across different days (22,23). Thus, despite the wide application of BOLD fMRI in studies of

normal physiology and disease, the technique is limited in its ability to detect group differences and longitudinal effects.

In recent years, there has been much focus on developing techniques for direct quantification of CMRO₂ (see **Table 1.1** and citations). However, none of these techniques achieve both the high temporal resolution and whole-brain coverage of BOLD fMRI. Because the brain is a spatially heterogeneous and temporally dynamic organ, spatial and temporal resolution are both of critical importance in functional neuroimaging. Therefore, an attractive approach to CMRO₂ quantification is conversion of BOLD signal changes to relative changes in CMRO₂, known as BOLD calibration.

The relationship between neuronal activity and BOLD signal reflects a complex interplay between multiple factors (see **Figure 1.5**), including CBF, CBV, and CMRO₂, as well as tissue properties such as blood vessel diameter, and field strength. BOLD calibration first requires modeling these various contributions to BOLD signal. This has typically been accomplished using the Davis model (59), which relates relative changes in BOLD, CBF, and CMRO₂ in response to a stimulus:

$$\frac{\Delta BOLD}{BOLD_0} = M \cdot \left(1 - \left(\frac{CMRO_2}{CMRO_{2|0}} \right)^\beta \left(\frac{CBF}{CBF_0} \right)^{\alpha-\beta} \right) \quad [4.1]$$

where subscript 0 designates the baseline state, Δ denotes the change from baseline to activation, and M is the BOLD calibration constant, equal to the maximum possible BOLD signal change that would occur if all dHb were removed. The exponent α , the Grubb constant, reflects the relationship between CBF and CBV changes (75), while β reflects the relative contributions of large and small vessel dephasing effects (69,70). Exponents α and β are typically treated as constants. Although the Davis model has important theoretical limitations, including the fact that it excludes intravascular signal contributions, simulations based on a more complete multi-compartment BOLD signal model suggest that the general form of **Equation 4.1** is remarkably

accurate (82). A more detailed description and derivation of the Davis model is given in **Section 1.2.4.2**.

In BOLD calibration experiments, CBF and BOLD signal are typically measured simultaneously using an ASL pulse sequence (56,57), ideally with a double echo or double excitation scheme to achieve optimal contrast for both ASL and BOLD signals (166). This leaves only M and CMRO₂ as unknowns; thus, BOLD calibration is synonymous with determining M, which is expected to vary between subjects and across brain regions, and, therefore, should ideally be spatially mapped (83,84). Accurate M mapping is crucial for successful BOLD calibration as errors in M can heavily influence subsequently quantified CMRO₂ changes (84).

Davis et al. first demonstrated an approach to M calibration based on measuring hypercapnia-induced changes in BOLD and CBF via CO₂ gas-mixture breathing (59). If CO₂ is assumed to have a negligible effect on CMRO₂, **Equation 4.1** can be simplified as:

$$\frac{\Delta BOLD}{BOLD_0} = M \cdot \left(1 - \left(\frac{CBF}{CBF_0} \right)^{\alpha-\beta} \right) \quad [4.2]$$

Measurement of CBF and BOLD during baseline and hypercapnia are then used to determine M, which is subsequently applied to the full Davis model (**Equation 4.1**) to determine CMRO₂ changes associated with subsequent functional experiments. Early application of this approach was used to demonstrate large and stimulus-intensity-dependent CMRO₂ changes in the primary visual cortex in response to a graded visual stimulus (42), supporting the notion that elevated energy demands in response to brain activation are met largely through oxidative metabolism. Hypercapnia-calibrated fMRI has demonstrated improved intra- and inter-subject reproducibility compared to BOLD signal alone (85).

The major limitation of hypercapnia-based calibration is the need to assume a specific CMRO₂ response to hypercapnia. Despite numerous studies, CO₂ effects on cerebral metabolism remain a topic of controversy (117), with disparate results from recent studies using similar experimental

paradigms and study populations (86,87,124,141). M-values derived from CO₂-based calibration are also highly sensitive to errors from noise-prone ASL-derived CBF values due to the large negative exponent ($\alpha-\beta$) on the CBF term in **Equation 4.2**. Finally, because it induces a sensation of breathlessness, CO₂ is not well tolerated by some subjects, limiting its application.

To address these challenges, Chiarelli et al. (88) proposed an alternative BOLD calibration approach based on hyperoxia (88). Unlike hypercapnia, which is used to isolate the effects of CBF on BOLD signal, hyperoxia causes BOLD signal changes based on changes in [dHb]_v with only small effects due to blood flow (89). Following the deoxyhemoglobin dilution model proposed by Hoge et al. (81) and assuming CBF changes minimally in response to hyperoxia (89), one obtains an alternative form of the calibration equation:

$$\frac{\Delta BOLD}{BOLD_0} = M \cdot \left(1 - \left(\frac{[dHb]_v}{[dHb]_{v_0}} \right)^\beta \right) \quad [4.3]$$

Hyperoxia gas-mixture breathing has the advantages of better subject tolerability and a lack of sensitivity to noisy ASL-derived CBF measurements. However, hyperoxia may cause a small change in CBF, which can be incorporated into the calibration model (88) but are not easily measured due to the low sensitivity of ASL to small flow changes and its dependence on O₂-induced changes in blood T₁. Furthermore, current implementations of the approach quantify [dHb]_v changes from EtO₂. This requires normal lung physiology and an assumed baseline OEF and CMRO₂ response to O₂. This is problematic because while OEF is relatively uniform across the brain (167), it varies significantly between even healthy subjects (61,66). Furthermore, CMRO₂ may decrease slightly in response to hyperoxia (105).

Recent approaches have attempted to combine hypercapnia and hyperoxia for improved calibration accuracy (90,91). These methods also allow determination of baseline Y_v and CMRO₂ in addition to M. However, multiple gas manipulations add further time and complexity to the protocol, while still requiring many of the aforementioned assumptions.

Improved BOLD calibration requires: 1) removing problematic model assumptions, 2) reducing calibration model dependence on noise-sensitive parameters (i.e., ASL-derived CBF), and 3) increasing the accuracy of the measurements applied to the model. To accomplish this, we propose a novel pulse sequence and modified BOLD calibration model. The technique combines rapid, MR-based quantification of whole-brain Y_v and tCBF with the usual ASL-based BOLD calibration pulse sequence for voxel-wise mapping of CBF and BOLD signal. Data from either hypercapnia or hyperoxia gas-mixture breathing are applied to a generalized Y_v -based calibration model, which assumes only that changes in $1-Y_v$ are spatially uniform across the brain.

4.3. Methods

4.3.1. Y_v -Based Model

Following a similar derivation as the hyperoxia-calibration model (88), but without assuming small changes in CBF, one obtains the following calibration equation:

$$\frac{\Delta BOLD}{BOLD_0} = M \cdot \left(1 - \left(\frac{[dHb]_v}{[dHb]_{v_0}} \right)^\beta \left(\frac{CBF}{CBF_0} \right)^\alpha \right) \quad [4.4]$$

Because $[dHb]_v$ is linearly proportional to $1-Y_v$, **Equation 4.4** can be modified to:

$$\frac{\Delta BOLD}{BOLD_0} = M \cdot \left(1 - \left(\frac{1-Y_v}{1-Y_{v_0}} \right)^\beta \left(\frac{CBF}{CBF_0} \right)^\alpha \right) \quad [4.5]$$

In traditional calibrated BOLD approaches, an optimized ASL pulse sequence is used to measure CBF and BOLD simultaneously to maximize temporal correspondence between the measures and improve overall temporal resolution. In applying the Y_v -based model, one would ideally quantify Y_v simultaneously alongside CBF and BOLD. Although there are a number of recently proposed MR-based techniques for Y_v quantification (60-67,90-92,98,99,121,122,128,141,151),

most have poor temporal resolution compared to ASL. However, several recent studies (described in **Chapters 2-3** of this dissertation) have demonstrated rapid quantification of whole-brain Y_v using SBO applied to the SSS (86,135). In the present work, a BOLD-calibration-optimized ASL pulse sequence was combined with SBO to simultaneously generate voxel-wise CBF and BOLD maps as well as a global measure of Y_v . Addition of flow-encoding to the SBO sequence – i.e., OxFow – provides a robust, global measure of CBF as well. To avoid confusion, voxel-wise CBF from ASL data will be denoted ‘CBF’, whereas OxFow PC-MRI-derived blood flow will be denoted ‘tCBF’.

This combined Ox-BOLD sequence generates the necessary data for application to the Y_v -based model and has several advantages over previous calibration approaches. Unlike traditional hypercapnia calibration, no assumed $CMRO_2$ response is necessary, and sensitivity to noise-prone ASL-derived CBF values is reduced due to the small (α) exponent on the CBF term. The simultaneously acquired tCBF can be used to correct the voxel-wise ASL-derived CBF for pCASL labeling efficiency reduction which occurs at higher flow rates, such as during hypercapnia (168). Unlike traditional hyperoxia calibration, the Y_v -based model places no assumptions on the CBF response, which can be measured globally from the PC-MRI data with high precision and no T_1 sensitivity. Baseline Y_v does not need to be assumed, as it is measured from SBO, and thus capnography is not required. The Y_v -based model can be equally well applied to any global BOLD stimulus – including hypercapnia and hyperoxia – so long as the stimulus produces relative changes in $1-Y_v$ that are spatially uniform across the brain, as SBO measures Y_v globally. The traditional calibration approaches and the Y_v -based approach are compared schematically in **Figure 4.1**.

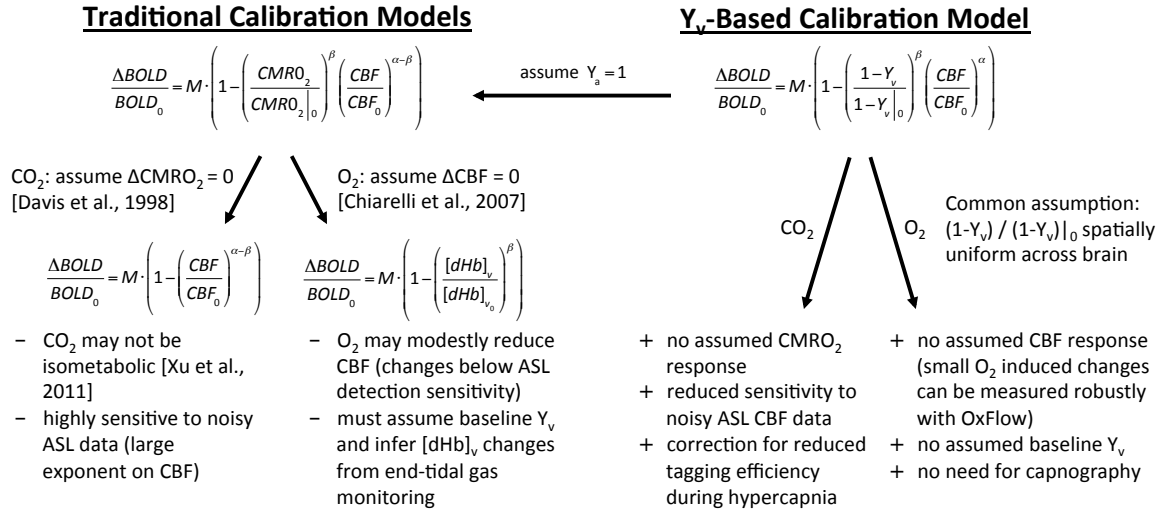


Figure 4.1: Schematic diagram comparing the traditional calibration models to the Y_v-based calibration model. Model equations, assumptions, and relative advantages and disadvantages are compared.

4.3.2. Ox-BOLD Pulse Sequence

The Ox-BOLD pulse sequence (**Figures 4.2 and 4.3**) involves interleaving an OxFlow module with a BOLD-calibration-optimized, dual-echo pCASL (169) ASL pulse sequence. Since its initial demonstration for whole-brain CMRO₂ quantification (66), various iterations of the OxFlow method have been demonstrated with sufficient temporal resolution to allow integration with other pulse sequences (86,135,155). The OxFlow module applied in Ox-BOLD is similar to that in the recently described iTRUST method (86) for combined T₂- and SBO-based CMRO₂ quantification (see **Chapter 3**). The OxFlow module used in Ox-BOLD (see inset in **Figures 4.2 and 4.3**) involves a single-slice, flow-encoded, dual-echo GRE with BRISK Cartesian view-sharing to achieve simultaneous SBO-based Y_v quantification and PC-MRI-based flow quantification. A detailed description of the OxFlow pulse sequence is given in **Chapter 2**. The pulse sequence parameters for the OxFlow module used in this work are virtually identical to those used in iTRUST (as described in **Chapter 3**).

Two versions of the Ox-BOLD pulse sequence were designed with single-slice (**Figure 4.2**) and multi-slice (**Figure 4.3**) EPI readouts, respectively. In single-slice Ox-BOLD, the OxFlow module

is interleaved within the PLD to maximize temporal efficiency; no additional scan time is needed for acquisition of global Y_v and tCBF. The pCASL labeling / control location is selected to intersect both internal carotid arteries and both vertebral arteries. The OxFow slice is positioned 20 mm superior to the EPI slice to prevent it from impacting blood that will later flow into the pCASL slice, potentially affecting the EPI-derived BOLD or CBF measurement. Successful application of a similar GRE module within the PLD of an ASL sequence has been demonstrated in the PIVOT technique, used to quantify perfusion and Y_v during post-ischemia reperfusion in the leg (164).

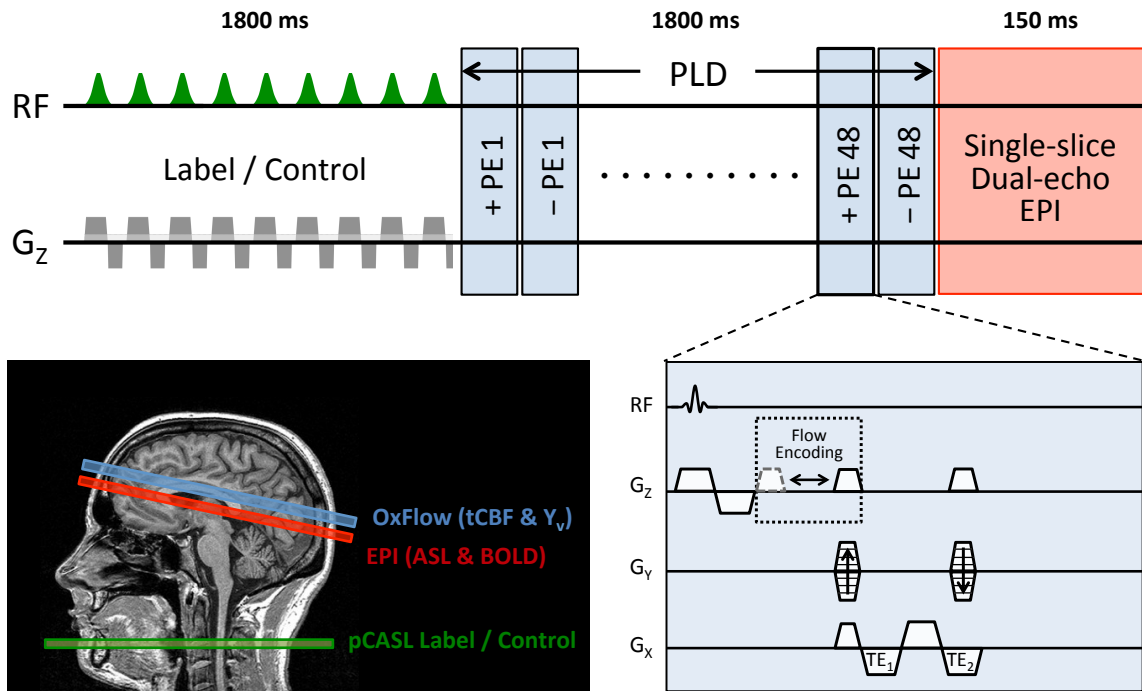


Figure 4.2: Single-slice Ox-BOLD pulse sequence diagram. The OxFow module is shown in the inset and relative slice locations are indicated on the sagittal magnitude image. Following pCASL labeling in the feeding arteries, OxFow global tCBF and Y_v data are acquired during the PLD, followed by a dual-echo EPI readout to generate voxel-wise CBF and BOLD maps. Sequence parameters include: pCASL – matrix = 80×80 (5/8th partial Fourier), FOV = 250×250 mm, slice thickness = 5 mm, TR/TE₁/TE₂ = 3650/8.1/52.9 ms, label duration = 1.8 s, PLD = 1.8 s, Hanning window average B1 = 1.7 μ T, pulse interval = 1 ms, G_{\max}/G_{avg} = 9/1 mT/m. OxFow – matrix = 192×48 (BRISK reconstructed to 192×192), FOV = 176×176 mm, slice thickness = 5 mm, TR/TE₁/ΔTE = 17.5/7.2/6.65 ms, VENC = 40 cm/s.

In multi-slice Ox-BOLD (**Figure 4.3**), the OxFlow module is interleaved outside the pCASL sequence, with slab-selective saturation pulses used to prevent interaction between OxFlow and pCASL. The OxFlow readout is initiated 350 ms following saturation in order to capture the tissue signal approximately at its steady-state longitudinal magnetization (86). The post-OxFlow slab-saturation resets spin history in the imaging slices, and also serves as a pre-saturation pulse for pCASL. The multi-slice sequence allows full brain coverage at the cost of the temporal efficiency afforded by the single-slice approach, resulting in prolongation of the TR from 3.75 to 6 seconds.

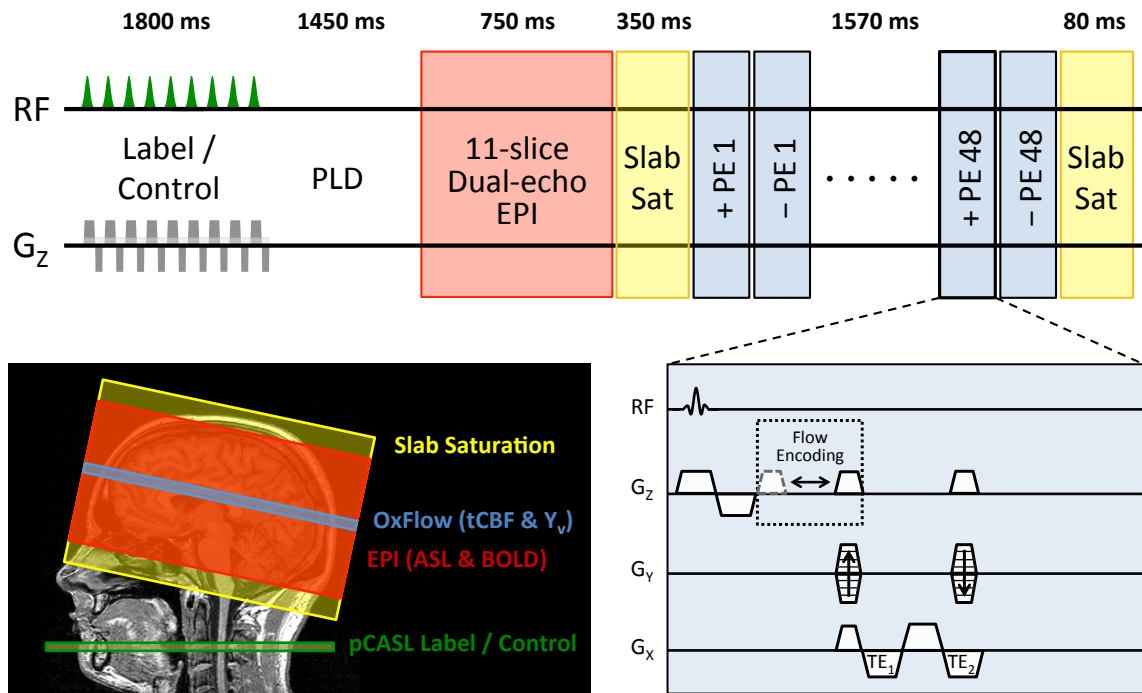


Figure 4.3: Multi-slice Ox-BOLD pulse sequence diagram. The OxFlow module is shown in the inset and relative slice/slab locations are indicated on the sagittal magnitude image. pCASL labeling in the feeding arteries and PLD is followed by a 2D, 11-slice, dual-echo EPI readout to generate voxel-wise CBF and BOLD maps. After a slab-selective saturation pulse to remove spin history and a 350 ms waiting period for signal recovery, OxFlow global tCBF and Y_v data are acquired, followed by a second slab-selective saturation for ASL pre-saturation. Sequence parameters include: pCASL – matrix = 64x64 (5/8th partial Fourier echo 1, 6/8th partial Fourier echo 2), FOV = 220x220 mm, slice thickness = 7 mm, slice gap = 1 mm, TR/TE₁/TE₂ = 6000/7.64/35.26 ms, label duration = 1.8 s, PLD = 1.8 s, Hanning window average B1 = 1.7 μ T, pulse interval = 1 ms, G_{\max}/G_{avg} = 9/1 mT/m. OxFlow – matrix = 192x48 (BRISK reconstructed to 192x192), FOV = 176x176 mm, slice thickness = 5 mm, TR/TE₁/ΔTE = 15.7/6.5/5.76 ms, VENC = 40 cm/s.

In both sequence versions, pCASL labeling parameters were adopted from Alsop et al. (170). An M_0 image was acquired at the beginning of each Ox-BOLD sequence to correct for proton density weighting.

4.3.3. In Vivo Imaging Experiments

All imaging was performed on a 3T Siemens Tim Trio system (Siemens Medical Solutions, Erlangen, Germany) using a vendor-supplied 32-channel receive-only head coil. Before each Ox-BOLD acquisition, a vendor-provided time-of-flight axial localizer scan was used for slice selection, and retrospectively to determine the vessel tilt angle (θ) in **Equation 1.22** for Y_v quantification. Furthermore, a two-slice-interleaved PC-MRI pulse sequence was run at the level of the internal carotid and vertebral arteries in the neck and the SSS in the head in order to determine the subject's SSSBF:tCBF ratio (135).

4.3.3.1. Single-Slice Ox-BOLD Validation

Single-slice Ox-BOLD uses the PLD to acquire OxFLOW data, which may cause inadvertent spin tagging effects. To test this possibility, single-slice Ox-BOLD was run in a single healthy volunteer at rest with five sequence versions: one with the OxFLOW module removed and four with the OxFLOW slice location varied relative to the EPI slice (which was kept constant) with $\Delta z = 20, 30, 60, \text{ or } 100 \text{ mm}$. 30 tag/control pairs (3:45 minutes) of data were collected for each of the five sequences, repeated a second time with acquisition order reversed to control for physiologic drift. Average gray matter CBF and T_2^* for each of the five sequences was quantified.

4.3.3.2. Gas-Mixture Breathing Experiments

A two-way non-rebreathing T-valve (2700 Series, Hans Rudolph, Inc., Kansas City, MO, USA) was used to deliver 5% CO_2 in room air (hypercapnia) or 100% O_2 (hyperoxia) for five minutes via a 100 L Douglas bag. For all gas stimuli, room air was delivered five minutes before and after the gas-mixture, and MRI data were collected continuously for the entire 15 minutes. Using this protocol, three healthy subjects were scanned with single-slice Ox-BOLD during hypercapnia.

One subject was subsequently scanned during hyperoxia. On a separate day, this same subject was scanned with multi-slice Ox-BOLD during hypercapnia followed by hyperoxia.

4.3.4. Data Analysis

OxFlow data analysis was analogous to that described previously (86,135). In brief, following BRISK data reordering to create full k-space images, time-resolved SSSBF was determined from the phase difference between images acquired at TE_1 with flow-encoding and flow-compensation. SSSBF was upscaled to tCBF based on the SSSBF:tCBF ratio quantified from the two-slice-interleaved PC-MRI scan. Time-resolved Y_v values were determined from the phase difference between flow-compensated data acquired at TE_1 and TE_2 , with quadratic fitting used to remove static field inhomogeneities (126).

EPI images were pre-processed using a standard pipeline involving homodyne reconstruction, N/2 ghost correction, brain extraction, motion correction, and 5mm Gaussian kernel smoothing. CBF was quantified using a general kinetic model (171) as described in (170). Average maps for baseline (CBF_0 , $BOLD_0$) and stimulus (CBF, BOLD) conditions were generated after excluding data in the transition periods (minutes 0-1 and 10-11 for baseline, 5-6 for stimulus). For single-slice Ox-Flow, this results in 32 and 64 tag/control pairs for stimulus and baseline conditions, respectively, and for multi-slice Ox-Flow, 20 and 40 tag/control pairs (due to the longer TR). OxFlow-derived, time-resolved Y_v and tCBF values were averaged over equivalent time periods.

For hypercapnia experiments, M-maps were generated using **Equation 4.5** (Y_v -based model) and **Equation 4.2** (Davis model). For hyperoxia experiments, only the Y_v -based model was applied, as the Davis model is unreliable for stimuli producing only small flow changes, and the traditional hyperoxia approach (**Equation 4.3**) requires capnography. For hyperoxia Y_v -based calibration, OxFlow-derived tCBF values were used in place of ASL-derived CBF values. Values of $\alpha = 0.18$ and $\beta = 1.5$ were used throughout (76,91). M-values from the single-slice sequence were normalized to a TE of 35.26 ms (the multi-slice sequence BOLD TE) to facilitate comparison between the sequence versions.

Whole-brain average values for ASL-derived CBF, BOLD, and M were generated based on manual segmentation of gray matter (single-slice Ox-BOLD) or application of exclusion criteria on a per-voxel basis (multi-slice Ox-BOLD). Inclusion criteria were as follows: Hypercapnia – $0\% < \Delta\text{BOLD} < 15\%$, $0\% < \Delta\text{CBF} < 200\%$, and $0\% < M < 20\%$; Hyperoxia – $0\% < \Delta\text{BOLD} < 15\%$, $50\% < \Delta\text{CBF} < 50\%$, and $0\% < M < 20\%$.

4.4. Results

4.4.1. Interleaved Sequence Assessment

Presence or location of the OxFlow module had no significant effect on CBF or T_2^* values. For the four sequences with the OxFlow module present, the mean and SD percent difference relative to the sequence with OxFlow module off were $0.9 \pm 3.0\%$ and $-0.4 \pm 0.5\%$, for CBF and T_2^* values, respectively. These small differences were not correlated with Δz ($P = 0.40$ and $P = 0.24$ for CBF and T_2^* , respectively, based on Pearson's correlation coefficients). Thus, no measurable error is introduced by acquiring OxFlow data in the pCASL PLD for single-slice Ox-BOLD. Similar validation experiments applied to the PIVOT sequence in the leg (164) also found no confounding effect due to GRE data acquired in an ASL PLD.

4.4.2. Single-Slice Ox-BOLD M-Quantification

Figure 4.4 displays parameter time courses and parametric maps derived for single-slice Ox-BOLD data from subject 3. CBF increases substantially in response to hypercapnia but decreases slightly in response to hyperoxia, whereas BOLD signal and Y_v increase in response to both stimuli. Temporal correspondence between ASL-derived CBF and OxFlow derived tCBF is observed for both stimuli. Hypercapnia M-maps and average M-values using the Davis and Y_v -based model show similar values and anatomic contrast. Hyperoxia results in a slightly higher average M-value, also with similar anatomic contrast. Average gray-matter M for the three subjects who underwent hypercapnia was $9 \pm 1\%$ using the Davis model, and $8 \pm 1\%$ using the Y_v -based model, in good agreement with recent literature (90,91,150).

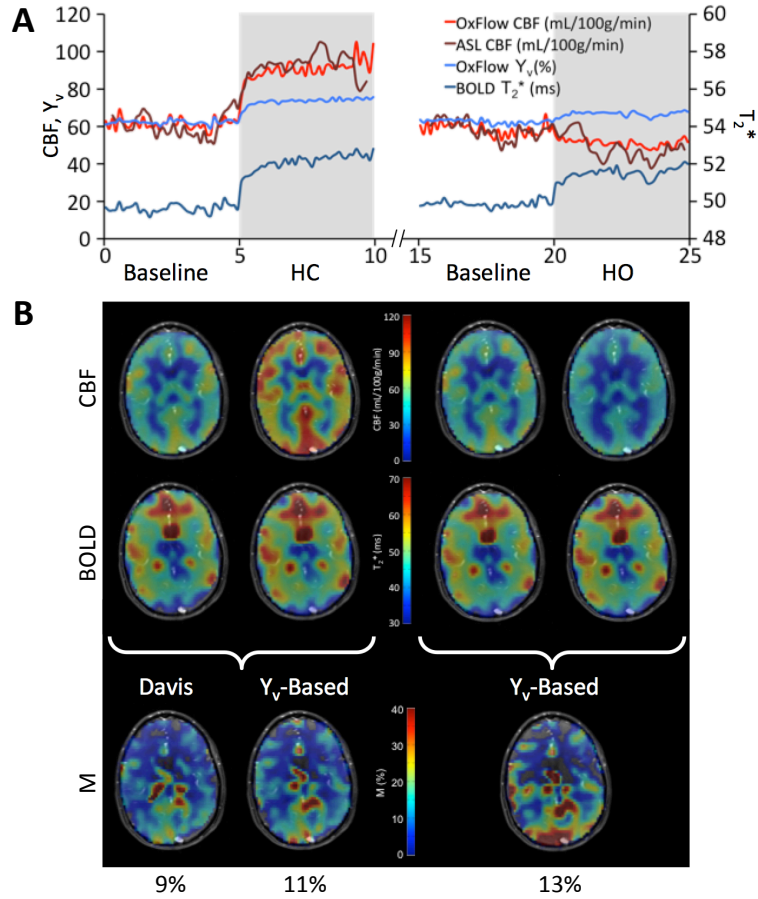


Figure 4.4: Single-slice Ox-BOLD data from an example subject. (A) Time-course plot of OxFlow-derived tCBF and Y_v and ASL-derived CBF and T_2^* during baseline, hypercapnia (HC), and hyperoxia (HO). (B) Parametric maps of time-averaged ASL-derived parameters (T_2^* , CBF) are placed below the corresponding time-course data, with gray matter voxel-wise averaged M-values at bottom. All parametric maps are overlaid on GRE magnitude images. Note: although gray matter masking was applied to generate the time-course values and average M values, parametric maps include all voxels to illustrate gray/white anatomic contrast and retain outliers to facilitate comparison of model performance.

4.4.3. Multi-Slice Ox-BOLD M-Quantification

Figure 4.5 displays magnitude images and parametric maps at each of the 11 slices from both the hypercapnia and hyperoxia calibration experiments in subject 3. CBF maps are not displayed for hyperoxia as OxFlow-derived tCBF was instead used in the Y_v -based model. As mentioned, without capnography, only the Y_v -based model can generate M-maps for hyperoxia. Contrast between gray and white matter is apparent in all parametric maps, with M-values greater in gray

than white matter as expected. Image quality is generally lower in the inferior slices due to susceptibility artifacts from air spaces. This is especially apparent in the hyperoxia images, as paramagnetic O_2 gas enhances susceptibility artifacts, causing intra-voxel dephasing and signal voids near the frontal sinuses (172).

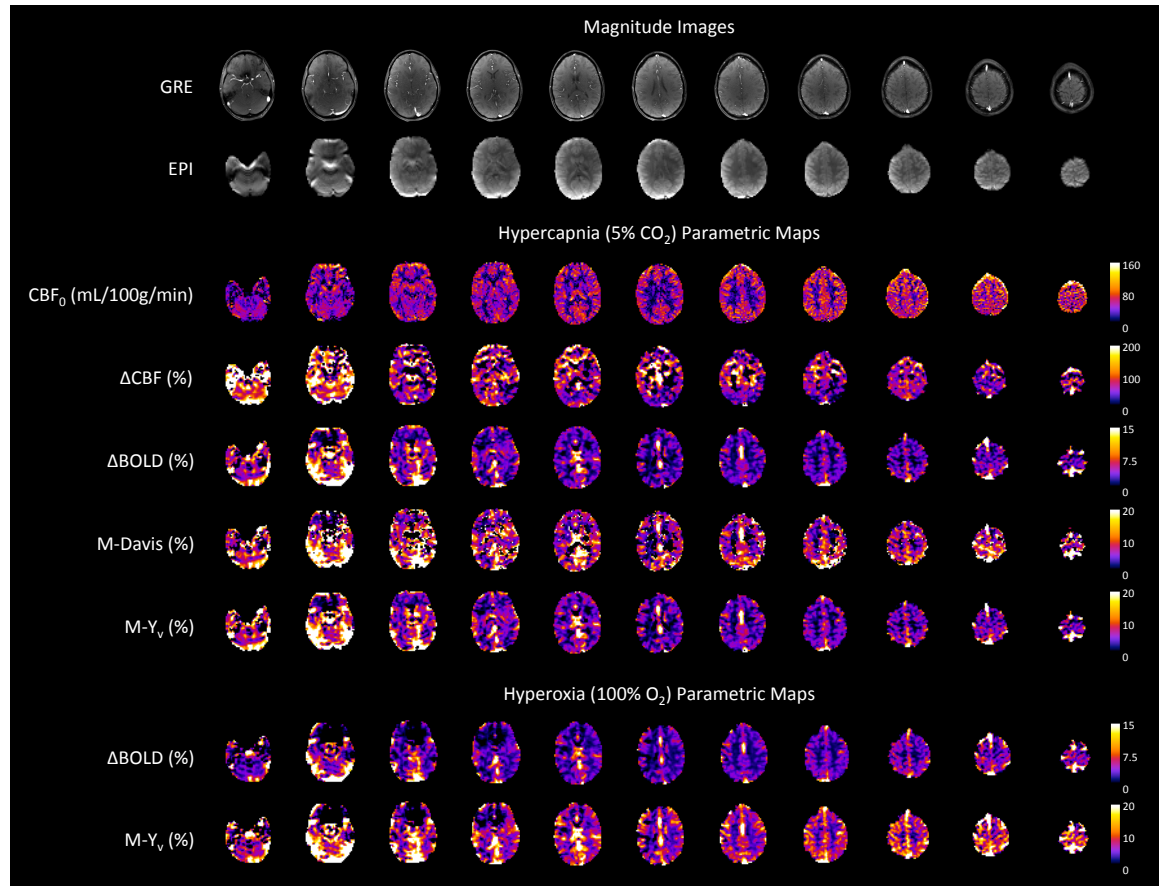


Figure 4.5: Multi-slice Ox-BOLD data from an example subject. The scale bars for each parameter value are shown at right. For ΔCBF , $\Delta BOLD$, and M , the scale bar ranges correspond to the outlier exclusion thresholds. Note: parametric maps include outlier voxels to illustrate gray/white anatomic contrast and retain outliers to facilitate comparison of model performance.

Figure 4.6 displays only the three middle slices for each of the three M-maps, highlighting the superior anatomic contrast present in the Y_v -based model M-maps, as well as the presence of more significant outliers (bright spots) in the Davis model M-map.

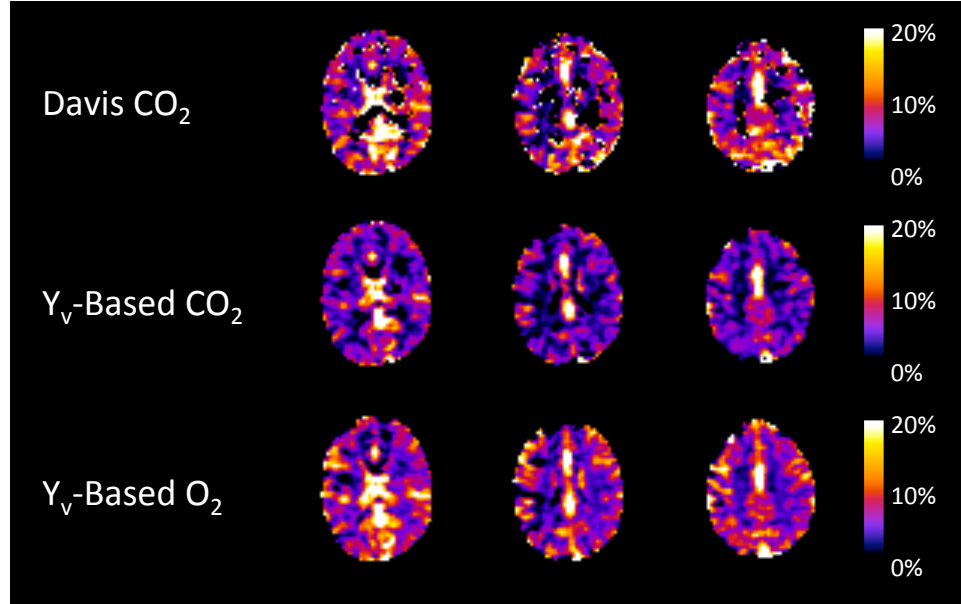


Figure 4.6: Zoomed-in parametric M-maps from each of the three methods (slices 5-7 only). Bright spots in the Davis model CO₂ calibration M-map represent outlier voxels, which are not apparent in the Y_v-based M-maps.

Table 4.1 lists whole-brain mean \pm SD parameter values, and the number of voxels used for averaging (i.e., excluding outliers) out of the total $N=12443$ voxels included in the initial brain extraction. Hypercapnia ASL-derived CBF and OxFLOW-derived tCBF correspond well. Average M-values for all three calibrations are similar, with Y_v-based model hyperoxia calibration lowest. Both Y_v-based model calibrations retained approximately 10% more voxels than the Davis model calibration.

Parameter	Hypercapnia	Hyperoxia
CBF ₀ (mL/100g/min)	46.3 \pm 31.1	-----
CBF / CBF ₀ (%)	69.2 \pm 44.0 (N = 9367)	-----
BOLD / BOLD ₀ (%)	3.9 \pm 2.9 (N = 10713)	3.5 \pm 2.7 (N = 10703)
(1-Y _v) / (1-Y _v) ₀ (%)	-54.1	-30.0
tCBF / tCBF ₀ (%)	68.6	2.6
M-Davis (%)	7.6 \pm 4.3 (N = 7779)	-----
M-Y _v (%)	5.5 \pm 3.8 (N = 8510)	7.0 \pm 4.1 (N = 8409)

Table 4.1: Whole-brain-averaged parameter values from hypercapnia and hyperoxia M-calibration experiments. N corresponds to the number of voxels remaining after outlier exclusion out of a possible 12443.

The distribution of M-values for each of the three maps is shown in **Figure 4.7**, with outliers included. As suggested by the data in **Table 4.1** and **Figure 4.6**, Y_v -based M-maps show a tighter distribution of M-values, and many fewer non-physiologic (i.e., very high or negative) M-values. The Davis model demonstrates a tendency to produce extreme outlier values not seen in the Y_v -based models; without outlier exclusion the average M-value for the Davis model is significantly greater whereas the average Y_v -based M-values are minimally affected (data not shown). Time-course plots (not shown) were similar to those from the single-slice data (**Figure 4.4a**).

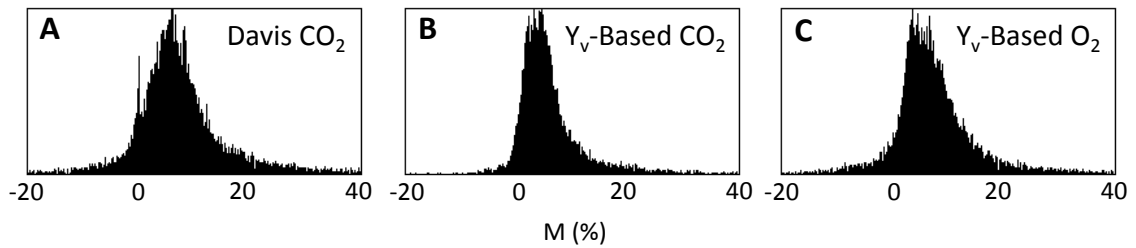


Figure 4.7: M-value histograms for each calibration. Outliers are not excluded. Note that all voxels with M values below 0 or above 20, as well as others excluded based on ΔCBF and $\Delta BOLD$ cutoffs, were not included in generating the whole-brain averaged values in **Table 4.1**.

4.5. Discussion

In a recent review of calibrated BOLD techniques (150), Blockley et al. suggested that current BOLD calibration approaches could benefit from additional measurement of Y_v , either to remove $CMRO_2$ assumptions from hypercapnia calibration or baseline Y_v assumptions from hyperoxia calibration. The proposed Y_v -based model and Ox-BOLD sequence incorporate these ideas into a comprehensive BOLD-calibration approach. Using this approach, hypercapnia and hyperoxia gas-mixture breathing calibration was successfully demonstrated with fewer assumptions compared to traditional methods, resulting in visually improved M-maps compared to traditional hypercapnia calibration using the Davis model. These proof-of-principle results should be replicated in additional subjects, with the calibration results applied in subsequent task-based fMRI experiments to assess the performance of the method in deriving fractional $CMRO_2$ response maps.

4.5.1. Prior Applications of Y_v to BOLD Calibration

Using TRUST MRI, Lu et al. (173) found a negative correlation between baseline Y_v and BOLD signal changes in response to a visual task, and suggested that Y_v could be used as a regressor to reduce intersubject variability in the BOLD response, potentially improving reproducibility of fMRI studies. However, such an approach does not provide a means of determining CMRO₂ from BOLD signal, and could potentially remove variability due to differences in the CMRO₂ response itself.

In a recent study, Driver et al. (165) demonstrated that Y_v can be used to remove the need for an assumed CBF/CBV coupling constant (α). Y_v was obtained by applying SBO to the phase data of the same EPI images used for BOLD signal quantitation. Because SBO is highly sensitive to partial voluming errors, EPI phase images do not provide an optimal approach given their relatively low spatial resolution. Furthermore, the Driver et al. method requires performing the functional task of interest during both baseline and hyperoxia. Though removing model dependence on α is a notable achievement, recent works suggest that errors due to inaccuracies in α can be minimized by relaxing the physical interpretation of α and β and instead treating them as fitting constants (82).

4.5.2. Assessment of Calibration Results

Both a single- and multi-slice version of the Ox-BOLD sequence was assessed. Single-slice Ox-BOLD has better temporal resolution for M-calibration, and thus may be useful for calibration during short-term stimuli (such as breath-hold). However, lack of whole-brain coverage is a major limitation. While the multi-slice Ox-BOLD sequence has a longer TR, the OxFlow module is only needed during calibration, but not in subsequent application of the sequence for CMRO₂ mapping during functional tasks. This is possible because M-values are minimally affected by pulse sequence parameters other than the EPI readout TE. Furthermore, the slab-saturation pulses isolate effects of the OxFlow module, such that the BOLD/ASL portion of the sequence should be unaffected by removal of the OxFlow module so long as the pre-saturation pulse remains.

Y_v -based calibration M-maps from the multi-slice data were visually superior to the Davis calibration M-maps (**Figure 4.6**). However, single-slice Ox-BOLD data showed little difference between models (**Figure 4.4**). The reason for these differences is unclear. Multi-slice Ox-BOLD M-maps also had lower average M-values compared to the equivalent single-slice maps from the same subject. This is likely a result of the different exclusion criteria used (i.e., gray matter thresholding for single-slice vs. stimulus-response-based outlier exclusion for multi-slice), which can have a significant effect on quantified M-values (174).

M-values tended to be higher in the most inferior slices, secondary to both higher ΔCBF and higher $\Delta BOLD$. These trends seem unlikely to be entirely physiologic, and are also not confined to the frontal regions of the brain, arguing against susceptibility-induced intravoxel-dephasing effects as a sole explanation (172). Investigation of these slice-dependent effects would be aided by additional data sets in more subjects.

4.5.3. Y_v -Based Model Assumptions

Despite removing various physiologic assumptions inherent in traditional calibration approaches, the Y_v -based model equation (**Equation 4.5**) assumes that fractional changes in $1-Y_v$ are spatially uniform across the brain. Although Y_v is quite uniform across the brain at baseline (16), limited data is available regarding the spatial heterogeneity of its fractional changes in response to gas-mixture breathing challenges. This critical assumption requires further validation, and may be more appropriate for hyperoxia than hypercapnia given the spatially heterogeneous CVR response to hypercapnia. An alternative approach to Ox-BOLD hypercapnia-based calibration would be to use the original Davis model equation, but with OxFLOW-derived fractional $CMRO_2$ changes in place of an assumed $CMRO_2$ response (i.e., isometabolism). However, this would sacrifice the reduced ASL noise sensitivity of the Y_v -based model. More work is needed to investigate the validity of these various approaches.

It is important to note that the Y_v -based model is specific to calibration, and the Davis model equation (**Equation 4.1**) must still be applied for subsequent determination of task-induced

CMRO₂ changes. The accuracy of CMRO₂ changes derived from **Equation 4.1** will be influenced by both measurement errors as well as inaccuracies in model assumptions. For parameters that appear in both equations, for instance, the α and β constants, these errors may be propagated or partially canceled. While **Figures 4.6 and 4.7** suggest that the Y_v -based model has improved stability against outliers, detailed modeling of error propagation (82,175) would provide insight into the expected performance of the various calibration approaches.

The SBO technique used to derive Y_v assumes that tissue susceptibility does not change. This may not be strictly true in hyperoxia, as a significant amount of paramagnetic O₂ becomes dissolved in tissue water and arterial blood (CBV_a). The potential effect of dissolved O₂ on SBO-measured Y_v should be further explored to determine whether the susceptibility model described by **Equation 1.16** is appropriate, and, if not, what corrections must be made.

4.5.4. Calibration Stimulus Considerations

Although simultaneous acquisition of all MR-derived model parameters is an attractive feature of Ox-BOLD, and ensures temporal correspondence of the various physiologic parameters, it is not critical when measurements are made over long periods of steady state stimuli, as is usually the case in gas-mixture calibration studies. In this case, serial measurements of ASL, BOLD, PC-MRI, and field mapping during both baseline and stimulus could provide similar information, and, furthermore, could be accomplished on most human scanning systems using only vendor-supplied product sequences. However, the fully interleaved approach offered by Ox-BOLD could allow calibration with shorter stimulus epochs, non-steady-state stimuli such as breath-hold (176), or graded/stepped stimuli (81,177), which could improve M-map accuracy by fitting **Equation 4.5** over a range of measured values.

The use of shorter stimulus periods or graded/stepped stimuli may be better suited to hyperoxia than hypercapnia calibration, as ASL SNR is often the limiting factor determining the number of averages needed (and ASL data is not needed for hyperoxia calibration). On the other hand, improving ASL SNR is desirable no matter what calibration method is used, as ASL data are

needed for subsequent derivation of task-induced CMRO_2 changes with **Equation 4.1**. To this end, use of a double-excitation rather than double-echo approach (166) could permit use of state-of-the-art 3D background-suppressed ASL readouts, which have long pulse trains precluding double-echo readouts. A feature of Ox-BOLD not explored here is the ability to correct for reduced ASL tagging efficiency during hypercapnia with OxFlow derived tCBF. Such correction is often estimated or determined from a separate PC-MRI acquisition (168).

4.6. Conclusions

This work demonstrates the potential for improved BOLD calibration using a new Y_v -based calibration model and hybrid Ox-BOLD pulse sequence for simultaneous BOLD and CBF mapping alongside whole-brain Y_v and tCBF quantification. The model requires fewer assumptions than traditional BOLD calibration approaches, and can be equally applied to hypercapnia and hyperoxia gas-mixture breathing. Preliminary data suggest the approach performs better than standard Davis model hypercapnia calibration, producing M-maps with more plausible contrast and many fewer non-physiologic outliers.

Chapter 5: Cerebral Metabolic Rate of Oxygen in Obstructive Sleep Apnea at Rest and In Response to Breath-Hold Challenge

5.1. Abstract

Obstructive sleep apnea (OSA) is associated with extensive neurologic comorbidities. It is hypothesized that the repeated nocturnal apneas experienced in patients with OSA may inhibit the normal apneic response, resulting in hypoxic brain injury and subsequent neurologic dysfunction. In this study, we applied the recently developed OxFlow MRI method for rapid quantification of CMRO₂ during a volitional apnea paradigm. MRI data were analyzed in 11 OSA subjects and 10 controls (mean \pm SD apnea-hypopnea index (AHI): 43.9 ± 18.1 vs. 2.9 ± 1.6 events/hour, $P < 0.0001$; age: 53.8 ± 8.2 vs. 45.3 ± 8.5 years, $P = 0.027$; body mass index (BMI): 36.6 ± 4.4 vs. 31.9 ± 2.2 kg/m², $P = 0.0064$). Although total cerebral blood flow and arteriovenous oxygen difference were not significantly different between apneics and controls ($P > 0.05$), apneics displayed reduced baseline CMRO₂ (117.4 ± 37.5 vs. 151.6 ± 29.4 μ mol/100g/min, $P = 0.013$). In response to apnea, CMRO₂ decreased more in apneics than controls (-10.9 ± 8.8 % vs. -4.0 ± 6.7 %, $P = 0.036$). In contrast, group differences in flow-based CVR were not significant. Results should be interpreted with caution given the small sample size and future studies with larger independent samples should examine the observed associations, including potential independent effects of age or BMI. Overall, these data suggest that dysregulation of the apneic response may be a mechanism for OSA-associated neuropathology.

5.2. Introduction

OSA is defined by structural and functional failure of the upper airway to maintain patency during sleep, resulting in periodic cessations or reductions in breathing and subsequent arterial desaturations. One in five adults in the Western world is believed to have at least mild OSA (178), a figure that is rapidly increasing as obesity, the main risk factor for OSA, becomes more prevalent. In addition to the typical symptoms of daytime sleepiness, snoring, and disturbed

sleep, OSA is also associated with significant systemic comorbidities, including hypertension, myocardial infarction and congestive heart failure, stroke, and type 2 diabetes (179). Of particular relevance to this study, patients with OSA have a high prevalence of central nervous system dysfunction, including depression, dementia, and diminished cognitive performance (180), MRI studies of OSA patients have detected neurologic lesions suggestive of hypoxic damage, including focal loss of gray matter (36) and white matter (181).

The etiology of OSA-associated neurologic comorbidities is not well understood. Brain tissue is particularly sensitive to hypoxic damage and rapid reperfusion (182), and brain regions known to be more acutely affected by hypoxia, such as the hippocampus, are among those identified as having gray matter loss in OSA (36). In normal physiology, apnea-induced hypercapnia and hypoxia cause chemoreceptor-mediated central vasodilation and concurrent peripheral vasoconstriction, preferentially conserving oxygen delivery to the brain to prevent hypoxic brain injury (183). In fact, recent work by our group has demonstrated that $CMRO_2$ is not just maintained, but slightly increased in young healthy subjects in response to 30-second volitional apnea (135). This may represent a mechanism for increasing energy stores in anticipation of prolonged apnea, and is consistent with gas-mixture breathing studies demonstrating increased $CMRO_2$ in response to steady-state hypoxia (105). However, it is possible that patients with OSA do not possess a normal apneic response, allowing hypoxic damage to occur during OSA-associated nocturnal apneas.

In support of this hypothesis are studies associating OSA with blunted CVR (37-39), typically defined as the CBF change in response to a vasoactive stimulus, such as hypercapnia (39) or apnea (37,38), the latter of which is particularly pertinent to OSA pathophysiology. In one study, CVR assessed in response to breath-hold by Doppler ultrasound was found to be significantly lower in OSA subjects, and more so in the morning, indicating that their diminished vasodilatory response is worsened by more recent exposure to nocturnal apneas (37). Recently, BOLD fMRI was used to detect reduced CVR in select brain regions of apneics, including the hippocampus (38). Blunted cerebrovascular responses to autonomic challenges (184,185) (e.g., orthostatic

hypotension, cold pressor challenge, etc.) suggest a mechanism of brain injury even during wakefulness, whereby day-to-day activities (e.g., standing) may not be met with an adequate cerebrovascular response to preserve central oxygen delivery. Finally, studies in both animals (186) and healthy humans (187) exposed to chronic intermittent hypoxia paradigms indicate a causal link between exposure to cyclic hypoxia and impaired vascular reactivity. If initial hypoxic injury itself leads to further blunting of the apneic response, a negative feedback cycle of worsening hypoxic damage could ensue.

Though supporting a mechanism for hypoxic brain injury in OSA, these previous studies all measure surrogate markers of brain oxygen metabolism (i.e., blood flow, perfusion, or BOLD fMRI signal), reductions of which do not necessarily correlate with decreased oxygen delivery and consumption. Of more central interest is whether oxygen consumption itself is maintained. Direct quantification of CMRO₂ requires quantification of both cerebral blood flow and oxygen extraction, the latter posing the greater technical challenge. CMRO₂ is less variable than blood flow or oxygen extraction in healthy subjects at baseline (66,101), and relatively conserved in response to physiologic challenges such as hypercapnia (87,124) and hypoxia (105), suggesting that CMRO₂ may be a more significant index for assessing neurovascular dysfunction than either blood flow or oxygenation alone. CMRO₂ reduction has been associated with many of the most common neurologic disorders, including mild cognitive impairment (112) and Alzheimer's disease (34), Parkinson's disease (127), and multiple sclerosis (111).

Quantifying CMRO₂ in response to apnea requires temporal resolution on the order of several seconds. Although this temporal resolution can be achieved with BOLD fMRI, attempts to 'calibrate' the BOLD signal (i.e., convert fractional BOLD signal change to fractional change in CMRO₂), rely on models with many physiologic assumptions and complex experimental setups involving gas-mixture breathing (150). Moreover, such calibration techniques still provide only relative changes in CMRO₂, with additional calibration needed to quantify baseline values in absolute physiologic units.

Recently, we have introduced an MRI technique for rapid whole-brain CMRO₂ quantification based on simultaneous SBO and PC-MRI blood flow quantification – termed OxFloW (66). Subsequent iterations of the technique have employed view-sharing to achieve temporal resolution as low as three seconds for whole brain CMRO₂ quantification (86,135). Unlike all previous CMRO₂ measurement techniques, this method has sufficient temporal resolution to detect CMRO₂ changes in response to apnea, allowing direct evaluation of the relationship between apnea, CVR, and brain oxygen delivery and consumption.

In this study, OxFloW was applied to compare the CMRO₂ response to apnea in OSA subjects and healthy controls. We hypothesized that OSA would be associated with reduced baseline CMRO₂, as well as a blunted CMRO₂ response to volitional apnea, and that this blunting would correlate with disease severity as measured by the apnea hypopnea index (AHI).

5.3. Methods

5.3.1. Susceptometry-Based Quantification of Y_v (SBO)

SBO exploits the relative paramagnetism of hemoglobin in the deoxygenated state, which results in a linear relationship between Y_v and venous blood magnetic susceptibility relative to surrounding tissue ($\Delta\chi$):

$$\Delta\chi = Hct \left(\Delta\chi_{do} (1 - Y_v) + \Delta\chi_{oxy} \right) \quad [5.1]$$

where Hct is the hematocrit and $\Delta\chi_{do}$ and $\Delta\chi_{oxy}$ are the volume susceptibility differences between fully oxygenated and deoxygenated packed red blood cells and between fully oxygenated packed red blood cells and water, respectively. Values of $4\pi \times 0.273$ and $4\pi \times 0.008$ p.p.m. (SI units) are used for $\Delta\chi_{do}$ and $\Delta\chi_{oxy}$, based on ex vivo calibration experiments (118). The susceptibility offset ($\Delta\chi$) induces a field shift (ΔB), which causes an increase in MR signal phase ($\Delta\phi$) between blood and surrounding ‘reference’ tissue as a function of echo spacing (ΔTE) in a multi-echo gradient echo imaging sequence:

$$\Delta B = \Delta\phi / \gamma\Delta TE \quad [5.2]$$

where γ is the proton gyromagnetic ratio.

Solving for Y_v thus hinges on determining $\Delta\chi$ from the measured ΔB , an inversion problem that is mathematically ill-posed in the general case. However, by modeling the blood vessel of interest as a pseudo-infinite straight cylinder (121) with defined tilt angle (θ) relative to the main magnetic field (B_0), an expression relating the susceptibility and field offsets can be derived analytically:

$$\Delta B = \frac{1}{6} \Delta\chi B_0 (3\cos^2\theta - 1) \quad [5.3]$$

To quantify global Y_v , this infinite cylinder model is applied to the SSS, the largest cerebral vein, which drains about 50% of total cerebral outflow. Y_v in the SSS is nearly identical to global cerebral venous oxygenation measured in the internal jugular veins as shown by T_2 -based oximetry methods (63,101). However, while trachea-induced susceptibility artifacts complicate SBO in the jugular veins, the field adjacent to the SSS is relatively homogeneous, making it the ideal candidate for global Y_v quantification via SBO.

5.3.2. Combination of SBO and PC-MRI for CMRO₂ Quantification (OxFlow)

SBO and PC-MRI can be readily combined as a single gradient echo sequence by applying flow-encoding before a multi-echo GRE readout, achieving simultaneous quantification of blood oxygenation and flow (**Figure 5.1**) (66,135). In this study, OxFlow was implemented with BRISK Cartesian view-sharing (154), with one-quarter k-space acquired at each time point and a resulting temporal resolution of two seconds for each simultaneously acquired pair of field- and velocity-maps. BRISK is more robust against subject motion compared to previous implementations of OxFlow using Keyhole view-sharing (135,136). Other OxFlow pulse sequence parameters used in this study were: reconstructed matrix = 208×208 , resolution = $0.85 \times 0.85 \times 5.00$ mm, TR/TE₁/ΔTE = 19.23/5.73/7.04 ms, bandwidth = 321 Hz/pixel, and VENC = 50 cm/s.

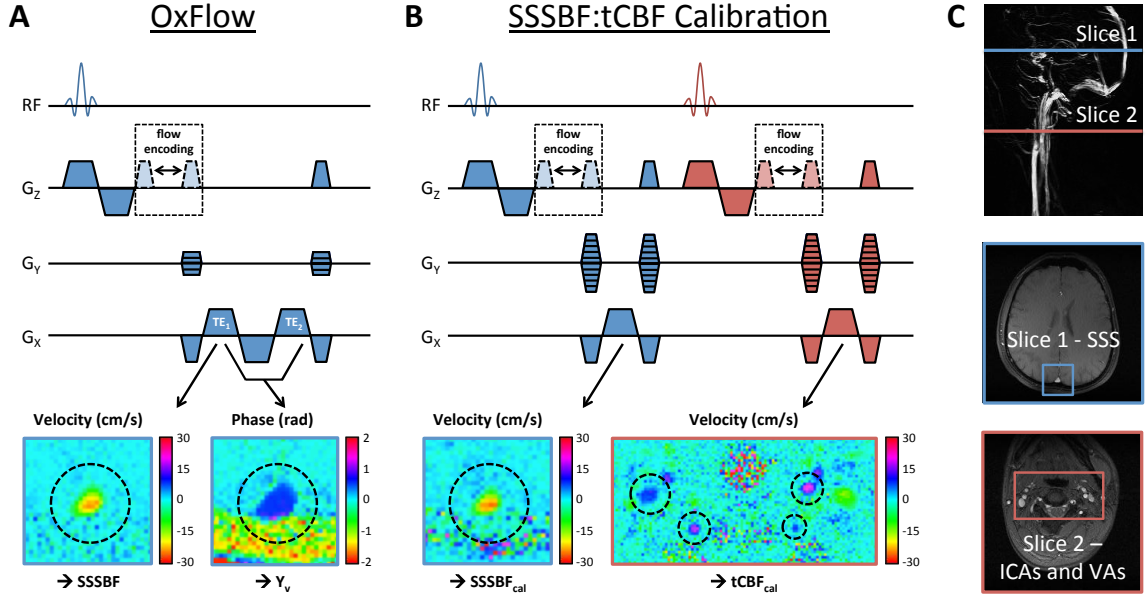


Figure 5.1: MRI pulse sequences for high temporal resolution quantification of global CMRO₂. (A) Single-slice OxFlow pulse sequence with BRISK k-space sampling produces a velocity- and field-map at two-second temporal resolution to quantify SSSBF and Y_v, respectively. (B) Dual-slice PC-MRI pulse sequence run prior to the OxFlow experiment allows quantification of the tCBF_{cal}/SSSBF_{cal} calibration factor used to upscale OxFlow-derived SSSBF to tCBF in **Equation 5.4**. Arrows indicate the echoes used to generate each image. Circles indicate the vessels of interest (superior sagittal sinus in the head, internal carotid arteries (ICAs) and vertebral arteries (VAs) in the neck). (C) Sagittal maximum intensity projection showing the head (blue) and neck (red) slice locations and corresponding axial magnitude images. Boxes in the axial images correspond to the parametric map ROIs in (A) and (B). All images are from a representative OSA subject (male, 63 years old). Figure from (40).

SSS blood flow (SSSBF) can be converted to total CBF (tCBF) via multiplication by a calibration factor determined through a separate two-slice-interleaved PC-MRI acquisition toggled between the internal carotid and vertebral arteries in the neck (which comprise tCBF) and the SSS in the head (**Figure 5.1b**) (135). This calibration step can be run before subsequent OxFlow experiments, allowing tCBF to be quantified as:

$$tCBF = \left(tCBF_{cal} / SSSBF_{cal} \right) \cdot SSSBF \quad [5.4]$$

CMRO₂ can then be quantified via the Fick Principle (10-12):

$$CMRO_2 = C_a \cdot tCBF \cdot (Y_a - Y_v) \quad [5.5]$$

where C_a is the hematocrit-dependent arterial oxygen content of blood in $\mu\text{mol O}_2/100\text{mL}$ and Y_a is the arterial oxygen saturation in $\%\text{HbO}_2$, which can be measured by digital pulse oximetry. The SSSBF:tCBF calibration pulse sequence parameters used in this study were: reconstructed matrix = 208×208 , resolution = $0.85 \times 0.85 \times 5.00 \text{ mm}$, TR/TE = 12.02/5.73 ms, bandwidth = 321 Hz/pixel, VENC = 50 cm/s (head slice) / 80 cm/s (neck slice), temporal resolution = 10 s, and averages = 4.

5.3.3. Subjects

Subjects were recruited based on results of a clinically indicated sleep study (in-lab attended polysomnography) performed at the University of Pennsylvania Sleep Center. The AHI was calculated as the mean number of apnea and hypopnea events per hour of sleep. Obstructive apneas were defined as at least a 90% drop in the thermal sensor excursion of baseline lasting at least 10 seconds; hypopneas were defined as a 50% reduction in airflow for greater than 10 seconds and associated with greater than 3% decrement in oxyhemoglobin saturation and/or an arousal. Nasal pressure monitors were used in all subjects to measure airflow.

Thirteen newly diagnosed apneics (AHI > 15 events/hour) and 10 non-apneic controls (AHI < 10 events/hour) were selected after screening for standard MRI exclusion criteria (claustrophobia, metal implants, pregnancy, etc.) and excluding diseases expected to affect cerebral metabolism and/or CVR, including congestive heart failure, chronic obstructive pulmonary disease, stroke, head trauma, and other significant neurological diseases. Cigarette smokers or users of other nicotine products were excluded as smoking can affect vasodilation. Subjects had no prior history of OSA diagnosis or continuous positive airway pressure (CPAP) use. Subject demographics are displayed in **Table 5.1**.

Parameter	OSA (N = 11)	Control (N = 10)	P-value
Age (years)	53.8 ± 8.2	45.3 ± 8.5	0.027*
Gender (Male / Female)	7 / 4	4 / 6	0.39
Race (CA / AA)	2 / 9	6 / 4	0.081
BMI (kg/m ²)	36.6 ± 4.4	31.9 ± 2.2	0.0064*
AHI (events/hour)	43.9 ± 18.1	2.9 ± 1.6	< 0.0001*
Y _a Nadir (%HbO ₂)	77.5 ± 8.5	89.0 ± 3.7	0.0001*

Table 5.1: Group demographics and polysomnography data. Parameter values are reported as mean ± SD across subjects. P-values are based on Wilcoxon two-sample exact tests (Age, BMI, AHI, Y_a Nadir) or Fisher's exact tests (Gender, Race). Abbreviations: CA, Caucasian; AA, African American. * denotes P < 0.05. Table from (40).

5.3.4. Experimental Procedures

All imaging protocols were approved by the Institutional Review Board of the University of Pennsylvania according to the ethical standards of the Belmont Report, and subjects provided written informed consent. Prior to scanning, a capillary blood sample was obtained and analyzed using an Hb 201⁺ (HemoCue, Brea, CA, USA) portable hemoglobin measurement device for determination of Hct in **Equation 5.1** and C_a in **Equation 5.5**.

5.3.4.1. Volitional Apnea Paradigm

The apnea paradigm consisted of thirty-second breath-holds at end-expiratory volume to mimic nocturnal apneas experienced in OSA. Coaching was used to maximize intra- and inter-subject repeatability and consistency of the apneas. Prior to scanning, breathing at normal end-expiratory volume was explained and demonstrated. During all breath-holds, subjects were verbally instructed to “breathe in”, “breathe out”, and “stop breathing” at six, three, and zero seconds, respectively, before the designated start of each apnea period, and instructed to “breathe normally” at the end of the apnea period. Each subject performed two practice apneas in the MRI scanner prior to OxFlow scanning and three during OxFlow scanning. Verbal instructions were given via MRI-compatible headphones. Breath-hold compliance was monitored by respiratory bellows.

5.3.4.2. MR Imaging Protocol

To minimize biological confounds and normal variations that might occur during the diurnal cycle, all subjects were scanned in the afternoon and instructed to abstain from caffeine (which promotes vasoconstriction) on the day of the study. All MR-imaging studies were performed on a 1.5 T wide-bore (70 cm) Siemens Espree system (Siemens Medical Solutions, Erlangen, Germany) using vendor-supplied 12-channel head and 2-channel neck receive coils. Subjects were fitted with pulse oximetry (Expression, Invivo Research Inc., Orlando, FL, USA) and respiratory bellows before performing the first practice breath-hold. A vendor-provided axial localizer scan was run for subsequent slice planning, followed by a second practice breath-hold. To allow tCBF normalization to brain mass, a 1-mm-isotropic 3D T₁-weighted MPRAGE data set was acquired. Next, the SSSBF:tCBF calibration scan was run, followed by second-order shimming over the brain volume. Finally, the OxFlow sequence was run continuously for nine minutes, during which the subjects completed three coached 30-second apneas, each followed by two minutes of normal breathing recovery. The entire MRI protocol lasted approximately 20 minutes (**Figure 5.2**).

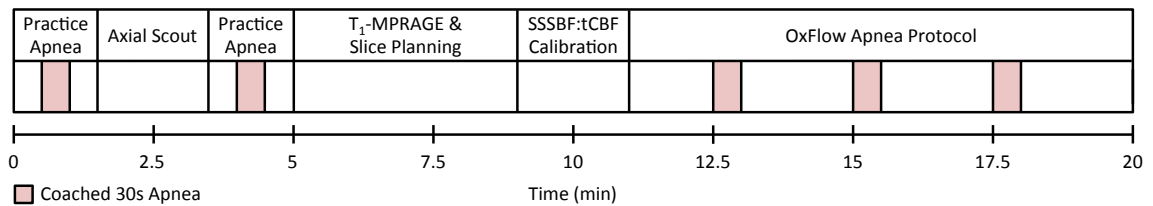


Figure 5.2: MRI protocol for quantifying CMRO₂ at rest and in response to apnea. Red boxes indicate 30-second coached volitional apneas. Two practice apneas are performed during protocol setup. During continuous CMRO₂ quantification with OxFlow, three apneas are performed, each followed by two minutes of normal breathing recovery. Figure from (40).

All subjects were able to successfully complete each breath-hold. However, two subjects (both apneics) failed to remain awake and experienced obstructive apneas during the recovery portions of the OxFlow acquisition, resulting in periodic desaturations throughout the paradigm. Their data were excluded from further analysis.

5.3.5. Data Processing

All image reconstruction was performed with in-house-written MATLAB (Mathworks, Natick, MA) scripts. BRISK-sampled raw OxFow data were first reordered to create full k-space data sets corresponding to each echo at two-second temporal resolution. Velocity-maps were obtained from the phase difference between flow-encoded and flow-compensated images reconstructed from data acquired at TE_1 . Field-maps were generated from the phase difference between flow-compensated images reconstructed from data acquired at TE_1 and TE_2 . Magnitude images at each time point were used to motion-correct the time series velocity- and field-maps using the StackReg plugin for ImageJ (188).

OxFow-derived SSSBF was determined by integration of the velocity-map over an ROI fully containing the SSS. Data from the two-slice-interleaved calibration sequence was processed analogously – with $tCBF_{cal}$ quantified by integration over the internal carotid and vertebral arteries – to calculate the $tCBF_{cal}/SSSBF_{cal}$ calibration factor to upscale OxFow-derived SSSBF and determine tCBF in **Equation 5.4**. Total brain volume was determined from the T_1 -MPRAGE data using the BET tool in FSL (157), and converted to mass based on an average brain density of 1.05 g/mL (158).

For Y_v quantification, bulk susceptibility effects were removed from the field-maps via second-order polynomial fitting of the field in brain tissue surrounding the SSS. Average phase was measured in two ROIs, one entirely within the SSS and another in a small reference region of brain tissue immediately surrounding the SSS approximately one vessel radius in width and located one vessel radius anterior to the SSS border. The difference in phase between these regions provides $\Delta\phi$ in **Equation 5.2**.

Y_a values obtained via pulse oximetry were recorded at two-second intervals matching each OxFow time point. To correct for the temporal delay between central and peripheral blood arrival from the lungs, the pulse oximetry data was time-shifted for each subject such that the initial resaturation following apnea occurred 7 seconds after apnea cessation. This timing corresponds

to the known circulatory transport delay between the lungs and brain (138) to within the temporal resolution of the pulse sequence. AVO_2D was quantified as $Y_a - Y_v$. Combination of **Equations 5.1-5.5** was used to determine temporally resolved $CMRO_2$.

5.3.6. Statistical Analysis

For each subject, time-course data were averaged over the three repeated blocks of the paradigm to improve signal-to-noise (SNR) and remove physiologic variation unrelated to apnea. For all parameters, average baseline values were quantified over the 24 seconds (12 data points) immediately preceding the “breathe in” command. For parameters that change monotonically in response to apnea, maximum ($tCBF$, Y_v) or minimum (Y_a , AVO_2D) percent changes relative to the average baseline values were quantified. To characterize the $CMRO_2$ apneic response, data were averaged over the second half (final 14 seconds, seven data points) of the apnea period to generate average end-apnea parameter values. The second half of the apnea period was used to eliminate residual breathing effects and because physiologic changes from apnea are not expected to occur instantaneously. The $CMRO_2$ apneic response was quantified as the percent change from the average baseline to the average end-apnea period.

Continuous outcomes were summarized using means and standard deviations (SDs) and categorical outcomes using frequencies and percentages. Given the relatively small number of apneics ($N = 11$) and controls ($N = 10$) in this study, summary measures were compared between groups using Wilcoxon two-sample exact tests (for continuous variables) and Fisher’s exact tests (for categorical variables). Baseline $CMRO_2$ and the $CMRO_2$ apneic response values were correlated with AHI using Spearman’s rank correlations. Statistical significance was defined as $P < 0.05$. Throughout the manuscript, parameter values are reported as mean \pm SD and all P-values are two-sided.

Given the limited overlap in age and BMI between OSA subjects and controls, it was not possible to model the independent effect of these variables on $CMRO_2$ or the $CMRO_2$ apneic response within the entire sample. Instead, the potential effect of between-group differences in these

variables was assessed in a secondary analysis within a small sample of apneics and controls (N = 4 pairs), matched for age (within 2.5 years) and BMI (within 2.5 kg/m²). Differences in traits of interest were calculated within each pair, as the value in the apneic subject minus that in the control. Observed differences were tested for significance using an exact P-value from the non-parametric signed rank test on the difference. The calculated differences in the matched sample were compared to that in the overall population. If a similar magnitude was observed, it was concluded that results in the overall population were unlikely to be primarily driven by differences in age and BMI. As a further step toward understanding potential confounding effects, age and BMI were associated with CMRO₂ and the CMRO₂ apneic response using Spearman's rank correlations. These tests were performed across all subjects (N = 21), apneics only (N = 11), and controls only (N = 10).

5.4. Results

5.4.1. Subject Demographic and Polysomnography Group Characteristics

AHI was significantly higher (43.9 ± 18.1 vs. 2.9 ± 1.6 events/hour, $P < 0.0001$) and Y_a nadir lower (77.5 ± 8.5 vs. 89.0 ± 3.7 %HbO₂, $P = 0.0001$) in apneics relative to controls. Subjects in the OSA group (AHI > 15 events/hour) were of greater age (53.8 ± 8.2 vs. 45.3 ± 8.5 years, $P = 0.027$) and BMI (36.6 ± 4.4 vs. 31.9 ± 2.2 kg/m², $P = 0.0064$), and had slightly though non-significantly larger brain mass (1437 ± 208 vs. 1376 ± 177 g, $P = 0.39$).

5.4.2. Baseline Differences Between OSA Subjects and Controls

Time-course plots of the MR- and pulse oximetry-measured parameters in a single OSA subject (male, 63 years old) (**Figure 5.3a**) demonstrate the expected increase in Y_v and tCBF and decrease in Y_a in response to apnea (red shading), as previously observed in young healthy subjects (135). The resulting CMRO₂ time-course in the same OSA subject (**Figure 5.3b**) shows a CMRO₂ reduction from baseline (denoted 'Base') to end-apnea (denoted 'EA') of 12.1%.

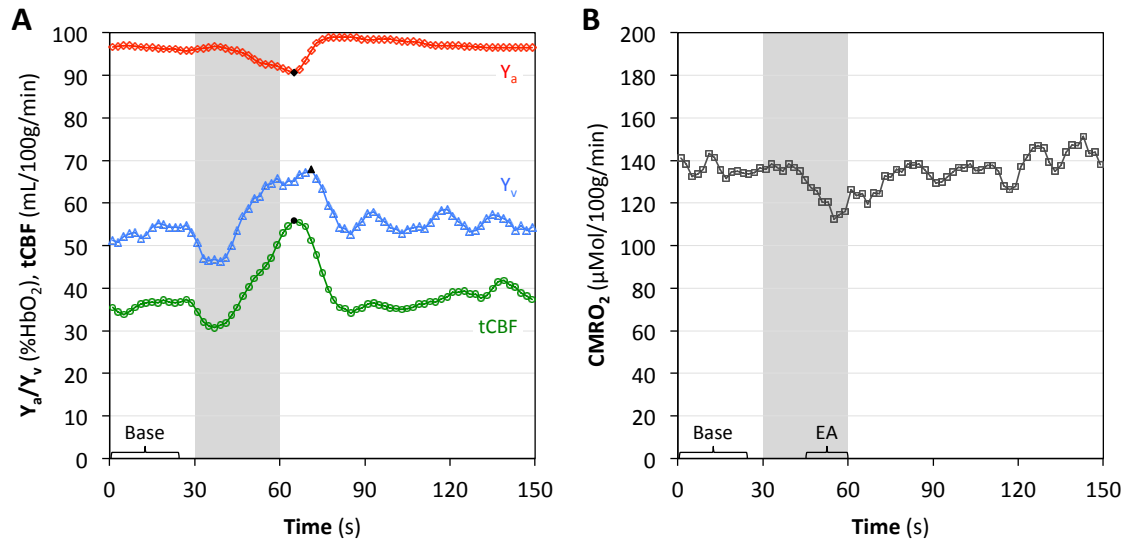
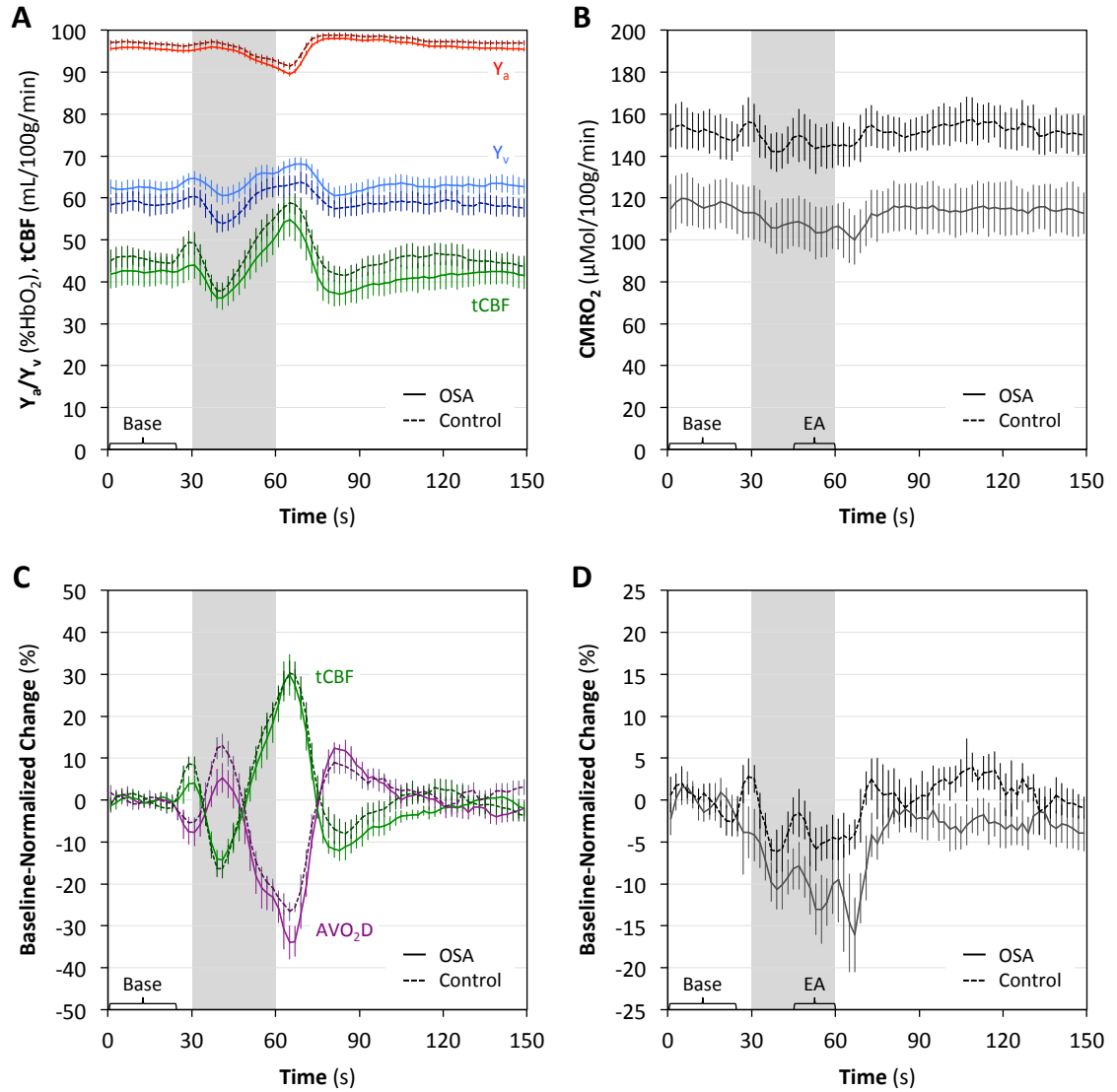


Figure 5.3: Apnea paradigm data in a representative OSA subject (male, 63 years old). (A) Single subject time-course plot of measured parameters (MRI-derived tCBF and Y_v and pulse-oximetry-derived Y_a) and (B) quantified CMRO₂ in absolute physiologic units. In all plots, data has been averaged over the three repeated blocks of the apnea paradigm and the gray shading indicates the apnea period. Black symbols correspond to the maximum (tCBF, Y_v) or minimum (Y_a) parameter values used to quantify the peak apneic response. 'Base' indicates the data averaged to quantify the baseline parameter values. 'EA' indicates the CMRO₂ data averaged to quantify the end-apnea CMRO₂ for determination of the CMRO₂ apneic response. Figure from (40).

Group time-course plots of measured parameters (**Figure 5.4a**) demonstrate a lower tCBF and Y_a and higher Y_v in apneics versus controls, as well as a considerably lower CMRO₂ in apneics (**Figure 5.4b**) throughout the paradigm. Although tCBF, Y_a , and Y_v baseline-averaged parameters values were not statistically different between groups (**Table 5.2**), they synergistically resulted in a significantly lower CMRO₂ in apneics versus controls (117.4 ± 37.5 vs. 151.6 ± 29.4 $\mu\text{mol}/100\text{g}/\text{min}$, $P = 0.013$). The initial rise and fall in tCBF and Y_v observed at the beginning of the apneic period is attributable to breath-hold-induced intrathoracic pressure changes causing modulations in cerebral venous return, as previously observed (135).



Parameter		OSA (N = 11)	Control (N = 10)	P-value
tCBF	Ave. Baseline (mL/100g/min)	42.4 ± 11.3	45.4 ± 7.1	0.20
	Peak Apneic Response (%)	35.6 ± 17.1	35.7 ± 8.8	0.56
Y _a	Ave. Baseline (%HbO ₂)	95.6 ± 1.8	96.9 ± 1.9	0.13
	Peak Apneic Response (%)	-6.8 ± 0.5	-6.1 ± 1.4	0.036*
Y _v	Ave. Baseline (%HbO ₂)	62.2 ± 6.2	58.7 ± 7.2	0.25
	Peak Apneic Response (%)	15.5 ± 10.6	13.4 ± 4.7	0.86
AVO ₂ D	Ave. Baseline (%HbO ₂)	33.4 ± 6.5	38.2 ± 7.5	0.17
	Peak Apneic Response (%)	-40.9 ± 14.0	-32.0 ± 6.4	0.099
CMRO ₂	Ave. Baseline (μmol/100g/min)	117.4 ± 37.5	151.6 ± 29.4	0.013*
	Ave. Baseline to End-Apnea Change (%)	-10.9 ± 8.8, P = 0.0049*	-4.0 ± 6.7, P = 0.13	0.036*

Table 5.2: Summary of baseline and apneic response parameters in OSA subjects and controls. Parameter values are reported as mean ± SD across subjects. P-values are based on Wilcoxon two-sample exact tests. * denotes P < 0.05. Table from (40).

5.4.3. Apneic Response in OSA Subjects and Controls

To better illustrate the apneic response, measured parameters (**Figure 5.4c**) and CMRO₂ (**Figure 5.4d**) are displayed in terms of percent changes relative to average baseline values. CVR – the change in tCBF in response to apnea – was not different between groups. However, there was a trend toward a larger decrease in oxygen extraction (AVO₂D) in apneics (-40.9 ± 14.0 vs. 32.0 ± 6.4 %, P = 0.099). CMRO₂ decreased significantly in apneics (-10.9 ± 8.8 %, P = 0.0049) but not in controls (-4.0 ± 6.7 %, P = 0.13), with a significant group difference (P = 0.036). Y_a reduction in response to apnea was greater in apneics (-6.8 ± 0.5 vs. -6.1 ± 1.4 %, P = 0.036), although it should be noted that the magnitude of this difference was quite small, and thus had little impact on the observed differences in the CMRO₂ apneic response.

5.4.4. Relationship Between CMRO₂ and AHI

To examine the sensitivity of CMRO₂ to OSA disease severity, AHI was correlated with both baseline CMRO₂ (**Figure 5.5a**) and the CMRO₂ apneic response (**Figure 5.5b**). When including all subjects (N = 21), AHI correlated significantly with baseline CMRO₂ (Spearman's ρ = -0.65, P = 0.0014) and the CMRO₂ apneic response (Spearman's ρ = -0.53, P = 0.013). When restricted to apneics only, AHI correlation with baseline CMRO₂ was only marginally significant

(Spearman's $\rho = -0.61$, $P = 0.047$), and AHI correlation with the CMRO_2 apneic response (Spearman's $\rho = -0.47$, $P = 0.14$) was only a trend.

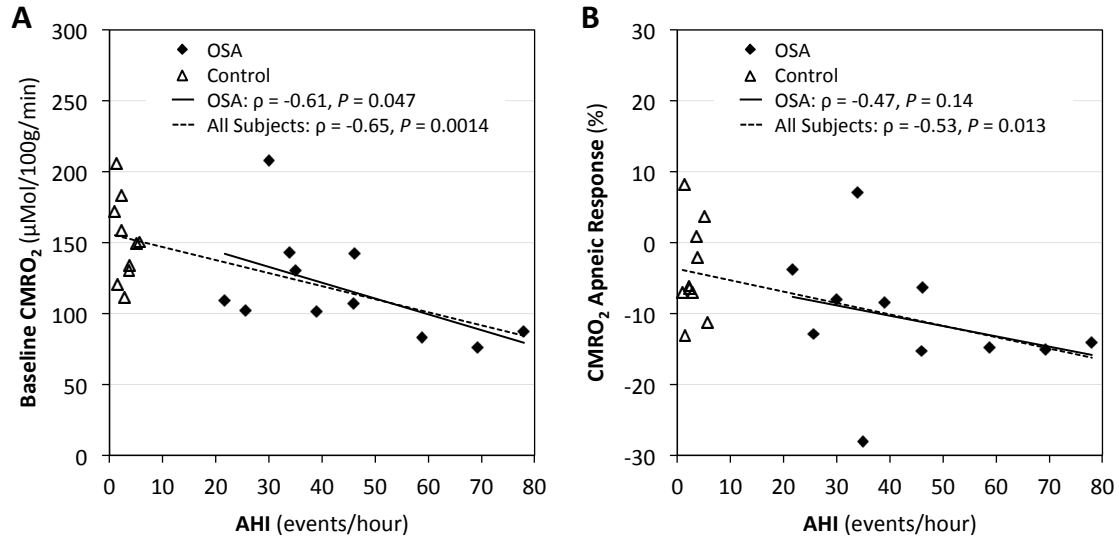


Figure 5.5: Relationship between CMRO_2 and AHI. (A) Correlation plots of baseline CMRO_2 vs. AHI and (B) CMRO_2 apneic response vs. AHI. OSA subjects (solid diamonds) and controls (empty triangles) are clearly separated by AHI. Least squares regression lines are plotted for OSA-subjects only (solid lines) and for all subjects (dotted lines) with corresponding Spearman's rank correlations and P-values indicated. Figure from (40).

5.4.5. Age and BMI Effects Analysis

Examination of a sub-sample of age- and BMI-matched subjects provided insight into possible confounding effects of the slight mismatch in these group characteristics. As expected given matching, pairs were similar with respect to age (mean \pm SD difference: -0.25 ± 1.26 years, $P > 0.99$) and BMI (1.2 ± 1.5 kg/m^2 , $P = 0.375$). Within the matched sample, apneics had a baseline CMRO_2 45.9 $\mu\text{mol}/100\text{g}/\text{min}$ lower on average compared to matched controls ($P = 0.125$) and a CMRO_2 apneic response 10.4% lower ($P = 0.375$). These differences are greater than those observed between apneics and controls in the overall sample, supporting the effect size seen in that population. This suggests that although statistical significance was not achieved in this small matched sample, associations in the overall sample were not completely driven by imbalances in age and BMI.

Though not reaching significance, the data were suggestive of a negative correlation between CMRO₂ and BMI ($\rho = -0.40$, $P = 0.070$) across the entire sample. In contrast, correlation between CMRO₂ and BMI in apneics only ($\rho = -0.38$, $P = 0.25$) or controls only ($\rho = 0.25$, $P = 0.49$) was not significant, and correlations between BMI and the CMRO₂ apneic response were not significant in any group. Across all subjects, correlations between age and both baseline CMRO₂ and CMRO₂ apneic response were small and non-significant. Age correlated significantly only with the CMRO₂ apneic response in control subjects ($\rho = 0.73$, $P = 0.016$), and approached significance when correlated with baseline CMRO₂ in control subjects ($\rho = 0.54$, $P = 0.105$).

5.5. Discussion

5.5.1. Interpretation of Apnea Paradigm Data

While a range of technologies have been used to study the pathophysiology of OSA, to the best of our knowledge, this is the first study to directly measure CMRO₂ and its change in response to apnea in OSA subjects. We highlight two main findings: 1) baseline CMRO₂ is lower in OSA subjects relative to controls and 2) there is a larger CMRO₂ decrease in response to apnea in OSA subjects. Given the small sample size of the study, and that confounding by age and/or BMI cannot entirely be excluded given that groups were not fully matched, these preliminary findings should be interpreted with caution and replicated in larger samples. However, the results are consistent with growing evidence that blunted autoregulatory mechanisms in OSA may contribute to OSA-associated neuropathology (37-39,184,185,189), and suggest a potential role for CMRO₂ in studying these mechanisms.

The observed reduction in baseline CMRO₂ in OSA subjects is a consequence of both oxygen delivery (tCBF) and oxygen extraction (AVO₂D) reduction. Although OSA subjects had lower values in both tCBF and AVO₂D on average, results did not reach statistical significance. As mentioned, these negative results must be interpreted with caution given the limited sample size. Nevertheless, they suggest that CMRO₂ may provide a more sensitive marker of baseline metabolic dysfunction than blood flow or oxygen extraction alone. Recently, a similar study of

OSA subjects and controls also found no group differences in baseline blood flow and no change in baseline blood flow in apneics treated with CPAP (38). We emphasize that our observed CMRO₂ reduction in OSA subjects cannot be explained by brain atrophy, as the CMRO₂ is normalized to brain volume, and, furthermore, brain mass was not significantly different between groups.

In addition to lower baseline CMRO₂, OSA subjects had a significantly larger decrease in CMRO₂ in response to apnea compared to controls. In contrast, the increase in flow in response to apnea (CVR) was nearly identical between groups, with the reduced CMRO₂ apneic response largely driven by a greater reduction in AVO₂D in apneics. Just as CMRO₂ has been proposed as a better measure of baseline neuronal function than blood flow, our results suggest that the CMRO₂ response to vasoactive challenges may provide a more sensitive marker of regulatory dysfunction than flow-based CVR. While some studies have associated OSA with reduced CVR (37-39), others, including the present study, have not (185,187). More so than CVR reduction alone, inability to maintain CMRO₂ during apnea provides a potential mechanism to explain the development of hypoxic brain damage in OSA.

Although not reaching statistical significance, the control group in this study also displayed a negative CMRO₂ response to apnea. This contrasts with previous data in 10 young, non-obese healthy subjects with no major underlying medical conditions, where a small but significant (6.0 ± 3.5 %, $P = 0.0004$) increase in CMRO₂ was observed during apnea using the same imaging protocol (135). One likely explanation for the different CMRO₂ apneic response in these two control groups is the differences in their clinical characteristics. Controls in the present study were recruited among older, relatively obese subjects from a Sleep Clinic. These subjects likely have a higher prevalence of obesity, high blood pressure, and metabolic syndrome compared to the previously studied young healthy cohort.

AHI correlated significantly with baseline CMRO₂ across all subjects as well as in apneics only, demonstrating that baseline CMRO₂ may be sensitive not just to apnea status but also apnea

disease severity. In contrast, AHI correlation with the CMRO₂ apneic response was significant among all subjects, but only a trend when restricted to apneics. Thus, studies with more subjects are needed to determine the relative sensitivity of baseline vs. apneic response CMRO₂ to OSA disease state.

5.5.2. Study Limitations and Future Directions

Our study has several limitations. First, it was performed in a relatively small sample of apneics and controls. A larger sample size would increase power to detect group differences, some of which were marginally significant. Thus, negative results ($P > 0.05$) should be interpreted with caution. However, our study did observe significant differences in our primary outcomes of interest, and, in general, power was approximately 75% to observe a mean difference between apneics and controls of 1.25 standard deviations.

In this study, OSA subjects were significantly older and more obese than controls. While these differences reflect differences between OSA and non-OSA patients in the general population, the small sample and limited covariate overlap restricted our ability to control for potential confounders which could affect CMRO₂ – such as age and BMI – in statistical models.

While some recent work suggests that baseline CMRO₂ may increase slightly with age (110), such a trend would have biased our results towards the null. In our data, there was a lack of association between CMRO₂ measures and age in the overall sample, further suggesting that age did not confound the relationship between OSA and CMRO₂ measures in our study. While a significant positive correlation was observed between age and the CMRO₂ apneic response in controls only ($\rho = 0.73$, $P = 0.016$), it is unclear why this effect would exist only in controls, and, therefore, this result should be interpreted with caution.

The relationship between BMI and CMRO₂ has not been specifically investigated previously, and presents an added complication in our study, as obesity may affect the subjects' ability to hold their breath. For instance, obesity lowers functional residual capacity, which could potentially cause more significant hypoxia or hypercapnia to develop during volitional apnea, impacting the

apneic response. While we observed a negative correlation between CMRO_2 and BMI across the entire sample ($\rho = -0.40$, $P = 0.070$), this does not necessarily demonstrate confounding by BMI, as such a trend would in fact be expected if CMRO_2 were independently associated with OSA, given the BMI mismatch between apneics and controls. Furthermore, the fact that the same trend was not observed among control subjects only ($\rho = 0.25$, $P = 0.49$) suggests that in the absence of OSA pathology, CMRO_2 is not independently associated with lower BMI, thus arguing against BMI effects driving our observed group differences. Finally, the observed correlation between BMI and CMRO_2 was only 62% as strong as the correlation between AHI and CMRO_2 ($\rho = -0.65$, $P = 0.0014$). Thus, it is possible that the observed CMRO_2 correlation with BMI is due to an independent CMRO_2 association with AHI, rather than BMI. Future, larger studies including subjects and controls with a similar range of BMIs could better assess whether BMI independently affects CMRO_2 , and whether any such effects exist across the general population or are restricted to apneics alone.

CMRO_2 group differences observed in the overall study sample were similar to those in the subset of age and BMI matched subjects, again arguing in favor of OSA independently lowering baseline CMRO_2 and the CMRO_2 apneic response. However, it will be essential for larger independent studies to confirm the observed associations. Furthermore, future studies should examine the possible effects of additional OSA-associated co-morbidities, including type 2 diabetes.

Two subjects (both apneics) were excluded from data analysis due to inability to stay awake between breath-holds. Compliance could be improved in future studies via modification of the breath-hold protocol to include more frequent, shorter apneas, or by introducing visual cuing of the breath-holds, which in addition to sustaining subject attention, has been shown to improve breath-hold reproducibility (190). However, even with perfect subject compliance, volitional apnea may not elicit the same neurovascular response as true sleep-associated nocturnal apneas. To address this, our methodology could be applied during sleep to capture true apneic events in

OSA subjects. The feasibility of high temporal resolution MR imaging during sleep has been demonstrated in previous studies examining airway closure in OSA (191).

A limitation of the OxFlow technique is that it is confined to quantification of global blood flow, oxygenation, and CMRO₂. Though apnea, like hypercapnia and hypoxia, can be thought of as a global cerebrovascular challenge, OSA has been associated with focal brain lesions (36,181), and a recent study employing BOLD fMRI detected regional differences in CVR in OSA subjects (38). Unfortunately, CMRO₂ mapping techniques are still at a developmental stage, with temporal resolutions on the order of many minutes and image noise levels often requiring whole-brain averaging to achieve physiologically plausible parameter values. While mapping of BOLD fMRI signal is possible at high temporal resolution, it does not provide a direct measure of either brain oxygen metabolism or blood flow, but rather reflects a complex interplay between blood flow, tissue properties, and CMRO₂. A combination of both quantitative global measures, such as OxFlow, and qualitative but spatially resolved measures such as BOLD fMRI, could offer an ideal approach for future studies of vascular and metabolic dysfunction in OSA.

Interpreting changes in baseline and apneic tCBF and CMRO₂ is challenging, as such alterations could be viewed as either a cause or effect of underlying neuropathology. In a study of baseline CMRO₂ and hypercapnic CVR in subjects with mild cognitive impairment (192), reduced CMRO₂ in the setting of maintained CVR was interpreted as suggesting less demand for oxygen due to primary cerebral dysfunction, as opposed to failure to meet demand due to vascular dysfunction. In our study, reduced baseline CMRO₂ and maintained CVR were also observed, though the CMRO₂ apneic response was reduced, suggesting that there may be a component of supply-side deficiency in OSA not accounted for by CVR. Longitudinal monitoring of CMRO₂ in OSA could help to discriminate between these various interpretations, for instance, by determining whether changes in baseline CMRO₂ and CMRO₂ apneic response occur concurrently or serially in OSA disease progression, and the extent to which CPAP therapy and resulting neurocognitive improvements are reflected by CMRO₂ metrics. The simplicity, speed, and robustness of the OxFlow technique make it well suited for such applications.

5.6. Conclusions

In summary, our results suggest that baseline CMRO₂ is reduced in OSA subjects relative to controls, and, furthermore, that OSA subjects may fail to maintain normal CMRO₂ during apnea. These findings add to the growing evidence that OSA-associated neuropathology is a consequence of autoregulatory dysfunction. MR-based quantification of CMRO₂ may offer a new method for better understanding the mechanisms of neurologic impairment in patients with sleep apnea.

Chapter 6: Conclusions and Future Directions

6.1. Conclusions

MRI has facilitated major advancements in our understanding of brain energy use. This began with the advent of BOLD fMRI over 20 years ago, and has continued more recently with attempts to quantitatively measure CMRO₂. Although much effort has been focused toward spatially mapping CMRO₂, the brain is both spatially heterogeneous and temporally dynamic. This dissertation has outlined the development and application of a series of methods for dynamic quantification of CMRO₂. The major results of this work are summarized as follows:

In **Chapter 2**, we presented the OxFLOW method for high temporal resolution quantification of whole-brain CMRO₂. By applying temporal view-sharing and combining SBO-based Y_v and PC-MR-based tCBF quantification in the same slice, OxFLOW achieves the highest reported temporal resolution for absolute quantification of whole-brain CMRO₂: three seconds. This allows quantification of CMRO₂ during dynamic stimuli, demonstrated in application to breath-hold apnea, where a small but significant increase in CMRO₂ ($6.0 \pm 3.5\%$, $P = 0.00044$) was measured in ten young healthy subjects. This result highlights the utility of dynamic CMRO₂ quantification, and argues against treating breath-hold apnea as an isometabolic stimulus, as has been done previously in some BOLD fMRI calibration studies.

Unlike OxFLOW, the T₂-based TRUST technique is not limited by vessel geometry or background field effects; however, it is comparatively quite slow. In **Chapter 3**, we combined OxFLOW and TRUST, producing an interleaved iTRUST sequence capable of six-second temporal resolution, T₂-based, whole-brain CMRO₂ quantification. iTRUST was used to directly compare SBO and T₂-based CMRO₂ in response to hypercapnia, a topic of controversy in the functional imaging community as the two methods have produced conflicting results in recent literature. In striking agreement with these previous results, we found no significant change in iTRUST measured Y_v -based CMRO₂ ($P = 0.31$), but a substantial reduction in T₂-based CMRO₂ ($-14.6 \pm 3.6\%$, $P <$

0.0001). These results suggest a true bias exists between these widely applied techniques for CMRO₂ quantification, demanding further investigation.

Calibrated BOLD fMRI provides a unique opportunity for both high spatial and high temporal resolution CMRO₂ mapping, though current techniques lack the robustness of OxFow and TRUST. Thus, in **Chapter 4** we explored improved BOLD calibration through a combined Ox-BOLD approach, where direct quantification of whole-brain Y_v permits use of a generalized calibration model. Ox-BOLD calibration was demonstrated in a small group of healthy volunteers using both hypercapnia and hyperoxia gas-mixture breathing. Results suggest improved calibration with Ox-BOLD compared to the traditional Davis hypercapnia model, with significantly fewer non-physiologic outlier voxels and a more anatomically plausible gray/white matter contrast in calibration M-maps.

Finally, in **Chapter 5** we explored clinical application of dynamic CMRO₂ quantification in patients with OSA. The original OxFow method and breath-hold paradigm presented in **Chapter 2** were applied in a clinical pilot study of 11 apneics and 10 controls. Although CBF and CVR were not significantly different between groups ($P > 0.05$), apneics displayed a significantly reduced baseline CMRO₂ (117.4 ± 37.5 vs. 151.6 ± 29.4 $\mu\text{mol}/100\text{g}/\text{min}$, $P = 0.013$) and apneic CMRO₂ response (-10.9 ± 8.8 % vs. -4.0 ± 6.7 %, $P = 0.036$). This suggests that CMRO₂ may be a more sensitive marker of neurologic dysfunction than blood flow alone, and adds to growing evidence that OSA-associated neurologic dysfunction stems from blunting of normal cerebrovascular and cerebrometabolic autoregulation.

In summary, this dissertation has presented a number of promising techniques and applications for dynamic quantification of CMRO₂. Of the four main classes of CMRO₂ quantification techniques presented in **Chapter 1** (T_2^* , T_2' , T_2 , or susceptibility), significantly improved temporal resolution has been achieved for two (susceptibility and T_2), and a promising approach presented for improving a third (T_2^*). These various methods have been successfully applied to physiologic stimuli in healthy subject as well as in a pilot study of patients with OSA.

6.2. Future Directions

6.2.1. OxFlow Technical Improvements

The OxFlow technique pushes the limits of temporal resolution, and would benefit from modifications improving temporal SNR. Because SBO is scalable with field strength, with B_0 explicitly defined in the infinite cylinder model, application at 7T field strength is an attractive option for SNR improvement. Higher field strength would both increase bulk magnetization and result in greater susceptibility and flow-related phase accrual. However, realizing these benefits requires mitigating concomitant increases in background field inhomogeneity and chemical shift artifacts associated with high field strength.

Radial acquisition presents another method for improved temporal SNR. It achieves more optimal sampling of center versus outer k-space than the Cartesian view-sharing approaches (i.e., Keyhole and BRISK) currently applied to OxFlow. Furthermore, golden angle radial trajectories allow retrospective optimization of temporal-view sharing and under-sampling factors, and facilitate application of signal processing techniques such as compressed sensing (193).

A major limitation of the OxFlow technique is that it assumes infinite cylinder geometry, with tilt angle the only vessel feature used to relate measured phase accrual to Y_v . A more general approach suggested by Driver et al. (194) is to first measure a vessel of interest's exact geometry, and then apply a forward field calculation (195) to calibrate the field-susceptibility relationship. Using this approach as a calibration step could improve the accuracy of SBO-derived Y_v and permit its application to vessels with less than ideal geometry. This forward approach would also allow investigation (and mitigation) of the potential effects of adjacent bone, fat, and CSF on the accuracy of SBO.

6.2.2. Technical Investigations

The results of **Chapter 3** raise concerns regarding the relative agreement between, and accuracy of, SBO- and T_2 -based Y_v quantification techniques. As these methods gain wider application,

defining and understanding their potential biases is critically important. Given the relative complexity of the T_2 -based calibration model compared to that of SBO, we hypothesize an error in the former is most likely. However, this should be thoroughly investigated with both in vivo and ex vivo validation studies (100). The iTRUST pulse sequence would provide an ideal technique for such investigations.

Unlike other $CMRO_2$ quantification techniques, BOLD calibration offers both high spatial and high temporal resolution, though current techniques lack the necessary robustness to realize this potential. The Ox-BOLD pulse sequence and Y_v -based model presented in **Chapter 4** may be a step in the right direction, at the same time increasing the number of measured parameters while reducing the number of physiologic assumptions. Initial results are promising, though data in more subjects is needed, and the technique's underlying assumption of spatially uniform changes in $1-Y_v$ should be thoroughly validated. Although assessment of the Ox-BOLD method is challenging given the lack of a true gold standard for $CMRO_2$ quantification in humans, it may be possible in animals via comparison to direct $CMRO_2$ quantification techniques (i.e., ^{17}O MRI or ^{15}O PET).

6.2.3. Clinical Investigations

As discussed in **Chapter 5**, the conclusions regarding $CMRO_2$ reductions in OSA are limited by the small sample size of the study. Ongoing studies will validate these results in a larger cohort of subjects, including age- and weight-matched controls, using a modified radial version of the OxFlow sequence. To complement OxFlow-derived global $CMRO_2$, voxel-wise BOLD-based CVR maps will also be acquired using an identical breath-hold paradigm, and resting state perfusion maps obtained with state-of-the-art background-suppressed 3D ASL (196). Furthermore, it will be investigated whether OSA-associated changes in $CMRO_2$, CVR, and CBF are reversible with CPAP treatment, and whether these measures correlate with makers of neurologic function including cognitive battery performance.

In recent years, CBF and BOLD have been applied extensively to measure CVR in a variety of clinical disorders, including stroke (162) and Alzheimer's disease (163). However, we anticipate that CVR assessed in terms of CMRO₂ changes will provide a more sensitive marker of neurovascular dysfunction than traditional CBF- or BOLD-based measures. This hypothesis is supported by our finding of a significantly reduced CMRO₂ response to apnea in OSA, despite non-significant differences in traditional CBF-based CVR.

Indeed, dynamic assessment of CMRO₂ has many potential applications for both clinical investigations and basic neuroscience. Much work remains in addressing critical challenges and defining new avenues of discovery.

BIBLIOGRAPHY

1. Rolfe DF, Brown GC. Cellular energy utilization and molecular origin of standard metabolic rate in mammals. *Physiological reviews* 1997;77(3):731-758.
2. Safar P. Resuscitation from clinical death: pathophysiologic limits and therapeutic potentials. *Crit Care Med* 1988;16(10):923-941.
3. Attwell D, Laughlin SB. An energy budget for signaling in the grey matter of the brain. *Journal of cerebral blood flow and metabolism : official journal of the International Society of Cerebral Blood Flow and Metabolism* 2001;21(10):1133-1145.
4. Raichle ME, MacLeod AM, Snyder AZ, Powers WJ, Gusnard DA, Shulman GL. A default mode of brain function. *Proc Natl Acad Sci U S A* 2001;98(2):676-682.
5. Canton R. The electric currents of the brain. *British Medical Journal* 1875;2:278.
6. Berger H. Über das Elektrenkephalogramm des Menschen. *Archiv für Psychiatrie und Nervenkrankheiten* 1929;87:527-570.
7. Cohen D. Magnetoencephalography: evidence of magnetic fields produced by alpha-rhythm currents. *Science* 1968;161(3843):784-786.
8. Mosso A. Ueber den Kreislauf des Blutes im Menschlichen Gehirn. von Veit, Leipzig 1881.
9. Roy CS, Sherrington CS. On the Regulation of the Blood-supply of the Brain. *J Physiol* 1890;11(1-2):85-158 117.
10. A. F. Ueber die Messung des Blutquantums in den Herzventrikeln. *Verh Phys Med Ges Wurzburg* 1870;2:16-28.
11. Kety SS, Schmidt C.F. The determination of cerebral blood flow in man by the use of nitrous oxide in low concentrations. *Am J Physio* 1945;143:55-63.
12. Kety SS, Schmidt CF. The Nitrous Oxide Method for the Quantitative Determination of Cerebral Blood Flow in Man: Theory, Procedure and Normal Values. *J Clin Invest* 1948;27(4):476-483.
13. Sokoloff L, Reivich M, Kennedy C, Des Rosiers MH, Patlak CS, Pettigrew KD, Sakurada O, Shinohara M. The [¹⁴C]deoxyglucose method for the measurement of local cerebral glucose utilization: theory, procedure, and normal values in the conscious and anesthetized albino rat. *J Neurochem* 1977;28(5):897-916.
14. Petersen SE, Fox PT, Posner MI, Mintun M, Raichle ME. Positron emission tomographic studies of the cortical anatomy of single-word processing. *Nature* 1988;331(6157):585-589.
15. Fox PT, Raichle ME, Mintun MA, Dence C. Nonoxidative glucose consumption during focal physiologic neural activity. *Science* 1988;241(4864):462-464.
16. Fox PT, Raichle ME. Focal physiological uncoupling of cerebral blood flow and oxidative metabolism during somatosensory stimulation in human subjects. *Proc Natl Acad Sci U S A* 1986;83(4):1140-1144.
17. Ogawa S, Lee TM, Kay AR, Tank DW. Brain magnetic resonance imaging with contrast dependent on blood oxygenation. *Proc Natl Acad Sci U S A* 1990;87(24):9868-9872.
18. Ogawa S, Tank DW, Menon R, Ellermann JM, Kim SG, Merkle H, Ugurbil K. Intrinsic signal changes accompanying sensory stimulation: functional brain mapping with magnetic resonance imaging. *Proc Natl Acad Sci U S A* 1992;89(13):5951-5955.

19. Frahm J, Bruhn H, Merboldt KD, Hanicke W. Dynamic MR imaging of human brain oxygenation during rest and photic stimulation. *J Magn Reson Imaging* 1992;2(5):501-505.
20. Bandettini PA, Wong EC, Hinks RS, Tikofsky RS, Hyde JS. Time course EPI of human brain function during task activation. *Magnetic resonance in medicine : official journal of the Society of Magnetic Resonance in Medicine / Society of Magnetic Resonance in Medicine* 1992;25(2):390-397.
21. Kwong KK, Belliveau JW, Chesler DA, Goldberg IE, Weisskoff RM, Poncelet BP, Kennedy DN, Hoppel BE, Cohen MS, Turner R, et al. Dynamic magnetic resonance imaging of human brain activity during primary sensory stimulation. *Proc Natl Acad Sci U S A* 1992;89(12):5675-5679.
22. Aguirre GK, Zarahn E, D'Esposito M. The variability of human, BOLD hemodynamic responses. *Neuroimage* 1998;8(4):360-369.
23. Handwerker DA, Ollinger JM, D'Esposito M. Variation of BOLD hemodynamic responses across subjects and brain regions and their effects on statistical analyses. *Neuroimage* 2004;21(4):1639-1651.
24. Ances BM, Liang CL, Leontiev O, Perthen JE, Fleisher AS, Lansing AE, Buxton RB. Effects of aging on cerebral blood flow, oxygen metabolism, and blood oxygenation level dependent responses to visual stimulation. *Hum Brain Mapp* 2009;30(4):1120-1132.
25. D'Esposito M, Zarahn E, Aguirre GK, Rypma B. The effect of normal aging on the coupling of neural activity to the bold hemodynamic response. *Neuroimage* 1999;10(1):6-14.
26. Logothetis NK, Pauls J, Augath M, Trinath T, Oeltermann A. Neurophysiological investigation of the basis of the fMRI signal. *Nature* 2001;412(6843):150-157.
27. Malonek D, Grinvald A. Interactions between electrical activity and cortical microcirculation revealed by imaging spectroscopy: implications for functional brain mapping. *Science* 1996;272(5261):551-554.
28. Menon RS, Ogawa S, Hu X, Strupp JP, Anderson P, Ugurbil K. BOLD based functional MRI at 4 Tesla includes a capillary bed contribution: echo-planar imaging correlates with previous optical imaging using intrinsic signals. *Magnetic resonance in medicine : official journal of the Society of Magnetic Resonance in Medicine / Society of Magnetic Resonance in Medicine* 1995;33(3):453-459.
29. Baron JC, Bousser MG, Rey A, Guillard A, Comar D, Castaigne P. Reversal of focal "misery-perfusion syndrome" by extra-intracranial arterial bypass in hemodynamic cerebral ischemia. A case study with ¹⁵O positron emission tomography. *Stroke; a journal of cerebral circulation* 1981;12(4):454-459.
30. Sobesky J, Zaro Weber O, Lehnhardt FG, Hesselmann V, Neveling M, Jacobs A, Heiss WD. Does the mismatch match the penumbra? Magnetic resonance imaging and positron emission tomography in early ischemic stroke. *Stroke; a journal of cerebral circulation* 2005;36(5):980-985.
31. Warburg O. On the origin of cancer cells. *Science* 1956;123(3191):309-314.
32. Miles KA, Williams RE. Warburg revisited: imaging tumour blood flow and metabolism. *Cancer Imaging* 2008;8:81-86.
33. Zlokovic BV. Neurovascular pathways to neurodegeneration in Alzheimer's disease and other disorders. *Nature reviews Neuroscience* 2011;12(12):723-738.
34. Ishii K, Kitagaki H, Kono M, Mori E. Decreased medial temporal oxygen metabolism in Alzheimer's disease shown by PET. *J Nucl Med* 1996;37(7):1159-1165.

35. Silvestrini M, Pasqualetti P, Baruffaldi R, Bartolini M, Handouk Y, Matteis M, Moffa F, Provinciali L, Vernieri F. Cerebrovascular reactivity and cognitive decline in patients with Alzheimer disease. *Stroke; a journal of cerebral circulation* 2006;37(4):1010-1015.
36. Macey PM, Henderson LA, Macey KE, Alger JR, Frysinger RC, Woo MA, Harper RK, Yan-Go FL, Harper RM. Brain morphology associated with obstructive sleep apnea. *American journal of respiratory and critical care medicine* 2002;166(10):1382-1387.
37. Placidi F, Diomedi M, Cupini LM, Bernardi G, Silvestrini M. Impairment of daytime cerebrovascular reactivity in patients with obstructive sleep apnoea syndrome. *Journal of sleep research* 1998;7(4):288-292.
38. Prilipko O, Huynh N, Thomason ME, Kushida CA, Guilleminault C. An fMRI study of cerebrovascular reactivity and perfusion in obstructive sleep apnea patients before and after CPAP treatment. *Sleep medicine* 2014;15(8):892-898.
39. Reichmuth KJ, Dopp JM, Barczi SR, Skatrud JB, Wojdyla P, Hayes D, Jr., Morgan BJ. Impaired vascular regulation in patients with obstructive sleep apnea: effects of continuous positive airway pressure treatment. *Am J Respir Crit Care Med* 2009;180(11):1143-1150.
40. Rodgers ZB, Leinwand SL, Keenan BT, Kini LG, Schwab RJ, Wehrli FW. Cerebral metabolic rate of oxygen (CMRO₂) in obstructive sleep apnea at rest and in response to breath-hold challenge. *JCBFM* 2015;(in press).
41. Vaishnavi SN, Vlassenko AG, Rundle MM, Snyder AZ, Mintun MA, Raichle ME. Regional aerobic glycolysis in the human brain. *Proc Natl Acad Sci U S A* 2010;107(41):17757-17762.
42. Hoge RD, Atkinson J, Gill B, Crelier GR, Marrett S, Pike GB. Linear coupling between cerebral blood flow and oxygen consumption in activated human cortex. *Proc Natl Acad Sci U S A* 1999;96(16):9403-9408.
43. Toffaletti J, Zijlstra WG. Misconceptions in reporting oxygen saturation. *Anesth Analg* 2007;105(6 Suppl):S5-9.
44. Aaslid R, Markwalder TM, Nornes H. Noninvasive transcranial Doppler ultrasound recording of flow velocity in basal cerebral arteries. *J Neurosurg* 1982;57(6):769-774.
45. Coplin WM, O'Keefe GE, Grady MS, Grant GA, March KS, Winn HR, Lam AM. Thrombotic, infectious, and procedural complications of the jugular bulb catheter in the intensive care unit. *Neurosurgery* 1997;41(1):101-107; discussion 107-109.
46. Sheinberg M, Kanter MJ, Robertson CS, Contant CF, Narayan RK, Grossman RG. Continuous monitoring of jugular venous oxygen saturation in head-injured patients. *J Neurosurg* 1992;76(2):212-217.
47. Jobsis FF. Noninvasive, infrared monitoring of cerebral and myocardial oxygen sufficiency and circulatory parameters. *Science* 1977;198(4323):1264-1267.
48. Boas DA, Campbell LE, Yodh AG. Scattering and Imaging with Diffusing Temporal Field Correlations. *Phys Rev Lett* 1995;75(9):1855-1858.
49. Verdecchia K, Diop M, Lee TY, St Lawrence K. Quantifying the cerebral metabolic rate of oxygen by combining diffuse correlation spectroscopy and time-resolved near-infrared spectroscopy. *J Biomed Opt* 2013;18(2):27007.
50. Durduran T, Zhou C, Buckley EM, Kim MN, Yu G, Choe R, Gaynor JW, Spray TL, Durning SM, Mason SE, Montenegro LM, Nicolson SC, Zimmerman RA, Putt ME, Wang J, Greenberg JH, Detre JA, Yodh AG, Licht DJ. Optical measurement

- of cerebral hemodynamics and oxygen metabolism in neonates with congenital heart defects. *J Biomed Opt* 2010;15(3):037004.
51. Frackowiak RS, Lenzi GL, Jones T, Heather JD. Quantitative measurement of regional cerebral blood flow and oxygen metabolism in man using ¹⁵O and positron emission tomography: theory, procedure, and normal values. *J Comput Assist Tomogr* 1980;4(6):727-736.
 52. Mintun MA, Raichle ME, Martin WR, Herscovitch P. Brain oxygen utilization measured with O-15 radiotracers and positron emission tomography. *J Nucl Med* 1984;25(2):177-187.
 53. Ito H, Ibaraki M, Kanno I, Fukuda H, Miura S. Changes in cerebral blood flow and cerebral oxygen metabolism during neural activation measured by positron emission tomography: comparison with blood oxygenation level-dependent contrast measured by functional magnetic resonance imaging. *Journal of cerebral blood flow and metabolism : official journal of the International Society of Cerebral Blood Flow and Metabolism* 2005;25(3):371-377.
 54. Lauterbur PC. Image formation by induced local interactions. Examples employing nuclear magnetic resonance. 1973. *Clin Orthop Relat Res* 1989(244):3-6.
 55. Moran PR. A flow velocity zeugmatographic interlace for NMR imaging in humans. *Magn Reson Imaging* 1982;1(4):197-203.
 56. Detre JA, Leigh JS, Williams DS, Koretsky AP. Perfusion imaging. *Magnetic resonance in medicine : official journal of the Society of Magnetic Resonance in Medicine / Society of Magnetic Resonance in Medicine* 1992;23(1):37-45.
 57. Williams DS, Detre JA, Leigh JS, Koretsky AP. Magnetic resonance imaging of perfusion using spin inversion of arterial water. *Proc Natl Acad Sci U S A* 1992;89(1):212-216.
 58. Pauling L, Coryell CD. The Magnetic Properties and Structure of Hemoglobin, Oxyhemoglobin and Carbonmonoxyhemoglobin. *Proc Natl Acad Sci U S A* 1936;22(4):210-216.
 59. Davis TL, Kwong KK, Weisskoff RM, Rosen BR. Calibrated functional MRI: Mapping the dynamics of oxidative metabolism. *Proceedings of the National Academy of Sciences* 1998;95(4):1834-1839.
 60. He X, Yablonskiy DA. Quantitative BOLD: mapping of human cerebral deoxygenated blood volume and oxygen extraction fraction: default state. *Magnetic resonance in medicine : official journal of the Society of Magnetic Resonance in Medicine / Society of Magnetic Resonance in Medicine* 2007;57(1):115-126.
 61. Lu H, Ge Y. Quantitative evaluation of oxygenation in venous vessels using T2-Relaxation-Under-Spin-Tagging MRI. *Magnetic resonance in medicine : official journal of the Society of Magnetic Resonance in Medicine / Society of Magnetic Resonance in Medicine* 2008;60(2):357-363.
 62. Krishnamurthy LC, Liu P, Ge Y, Lu H. Vessel-specific quantification of blood oxygenation with T2-relaxation-under-phase-contrast MRI. *Magnetic resonance in medicine : official journal of the Society of Magnetic Resonance in Medicine / Society of Magnetic Resonance in Medicine* 2014;71(3):978-989.
 63. Jain V, Magland J, Langham M, Wehrli FW. High temporal resolution in vivo blood oximetry via projection-based T2 measurement. *Magnetic resonance in medicine : official journal of the Society of Magnetic Resonance in Medicine / Society of Magnetic Resonance in Medicine* 2013;70(3):785-790.

64. Bolar DS, Rosen BR, Sorensen AG, Adalsteinsson E. QUantitative Imaging of eXtraction of oxygen and Tissue consumption (QUIXOTIC) using venular-targeted velocity-selective spin labeling. *Magnetic resonance in medicine : official journal of the Society of Magnetic Resonance in Medicine / Society of Magnetic Resonance in Medicine* 2011;66(6):1550-1562.
65. Guo J, Wong EC. Venous oxygenation mapping using velocity-selective excitation and arterial nulling. *Magnetic resonance in medicine : official journal of the Society of Magnetic Resonance in Medicine / Society of Magnetic Resonance in Medicine* 2012;68(5):1458-1471.
66. Jain V, Langham MC, Wehrli FW. MRI estimation of global brain oxygen consumption rate. *Journal of cerebral blood flow and metabolism : official journal of the International Society of Cerebral Blood Flow and Metabolism* 2010;30(9):1598-1607.
67. Fan AP, Bilgic B, Gagnon L, Witzel T, Bhat H, Rosen BR, Adalsteinsson E. Quantitative oxygenation venography from MRI phase. *Magnetic resonance in medicine : official journal of the Society of Magnetic Resonance in Medicine / Society of Magnetic Resonance in Medicine* 2014;72(1):149-159.
68. Zhang J, Liu T, Gupta A, Spincemaille P, Nguyen TD, Wang Y. Quantitative mapping of cerebral metabolic rate of oxygen (CMRO₂) using quantitative susceptibility mapping (QSM). *Magnetic resonance in medicine : official journal of the Society of Magnetic Resonance in Medicine / Society of Magnetic Resonance in Medicine* 2014.
69. Ogawa S, Menon RS, Tank DW, Kim SG, Merkle H, Ellermann JM, Ugurbil K. Functional brain mapping by blood oxygenation level-dependent contrast magnetic resonance imaging. A comparison of signal characteristics with a biophysical model. *Biophys J* 1993;64(3):803-812.
70. Boxerman JL, Hamberg LM, Rosen BR, Weisskoff RM. MR contrast due to intravascular magnetic susceptibility perturbations. *Magnetic resonance in medicine : official journal of the Society of Magnetic Resonance in Medicine / Society of Magnetic Resonance in Medicine* 1995;34(4):555-566.
71. Yablonskiy DA, Haacke EM. Theory of NMR signal behavior in magnetically inhomogeneous tissues: the static dephasing regime. *Magnetic resonance in medicine : official journal of the Society of Magnetic Resonance in Medicine / Society of Magnetic Resonance in Medicine* 1994;32(6):749-763.
72. Luz Z, Meiboom S. Nuclear Magnetic Resonance study of the protolysis of trimethylammonium ion in aqueous solution. *The Journal of Chemical Physics* 1963;39:366-370.
73. Mark CI, Fisher JA, Pike GB. Improved fMRI calibration: precisely controlled hyperoxic versus hypercapnic stimuli. *Neuroimage* 2011;54(2):1102-1111.
74. Lu H, Golay X, Pekar JJ, Van Zijl PC. Functional magnetic resonance imaging based on changes in vascular space occupancy. *Magnetic resonance in medicine : official journal of the Society of Magnetic Resonance in Medicine / Society of Magnetic Resonance in Medicine* 2003;50(2):263-274.
75. Grubb RL, Jr., Raichle ME, Eichling JO, Ter-Pogossian MM. The effects of changes in PaCO₂ on cerebral blood volume, blood flow, and vascular mean transit time. *Stroke; a journal of cerebral circulation* 1974;5(5):630-639.
76. Chen JJ, Pike GB. MRI measurement of the BOLD-specific flow-volume relationship during hypercapnia and hypocapnia in humans. *Neuroimage* 2010;53(2):383-391.

77. Chen JJ, Pike GB. BOLD-specific cerebral blood volume and blood flow changes during neuronal activation in humans. *NMR Biomed* 2009;22(10):1054-1062.
78. Rostrup E, Knudsen GM, Law I, Holm S, Larsson HB, Paulson OB. The relationship between cerebral blood flow and volume in humans. *Neuroimage* 2005;24(1):1-11.
79. Ciris PA, Qiu M, Constable RT. Noninvasive MRI measurement of the absolute cerebral blood volume-cerebral blood flow relationship during visual stimulation in healthy humans. *Magnetic resonance in medicine : official journal of the Society of Magnetic Resonance in Medicine / Society of Magnetic Resonance in Medicine* 2014;72(3):864-875.
80. Mark CI, Pike GB. Indication of BOLD-specific venous flow-volume changes from precisely controlled hyperoxic vs. hypercapnic calibration. *Journal of cerebral blood flow and metabolism : official journal of the International Society of Cerebral Blood Flow and Metabolism* 2012;32(4):709-719.
81. Hoge RD, Atkinson J, Gill B, Crelier GR, Marrett S, Pike GB. Investigation of BOLD signal dependence on cerebral blood flow and oxygen consumption: the deoxyhemoglobin dilution model. *Magnetic resonance in medicine : official journal of the Society of Magnetic Resonance in Medicine / Society of Magnetic Resonance in Medicine* 1999;42(5):849-863.
82. Griffeth VE, Buxton RB. A theoretical framework for estimating cerebral oxygen metabolism changes using the calibrated-BOLD method: modeling the effects of blood volume distribution, hematocrit, oxygen extraction fraction, and tissue signal properties on the BOLD signal. *Neuroimage* 2011;58(1):198-212.
83. Ances BM, Leontiev O, Perthen JE, Liang C, Lansing AE, Buxton RB. Regional differences in the coupling of cerebral blood flow and oxygen metabolism changes in response to activation: implications for BOLD-fMRI. *Neuroimage* 2008;39(4):1510-1521.
84. Chiarelli PA, Bulte DP, Piechnik S, Jezzard P. Sources of systematic bias in hypercapnia-calibrated functional MRI estimation of oxygen metabolism. *Neuroimage* 2007;34(1):35-43.
85. Leontiev O, Buxton RB. Reproducibility of BOLD, perfusion, and CMRO₂ measurements with calibrated-BOLD fMRI. *NeuroImage* 2007;35(1):175-184.
86. Rodgers ZB, Englund EK, Langham MC, Magland JF, Wehrli FW. Rapid T₂- and susceptibility-based CMRO₂ quantification with interleaved TRUST (iTRUST). *NeuroImage* 2015;106:441-450.
87. Xu F, Uh J, Brier MR, Hart J, Jr., Yezhuvath US, Gu H, Yang Y, Lu H. The influence of carbon dioxide on brain activity and metabolism in conscious humans. *Journal of cerebral blood flow and metabolism : official journal of the International Society of Cerebral Blood Flow and Metabolism* 2011;31(1):58-67.
88. Chiarelli PA, Bulte DP, Wise R, Gallichan D, Jezzard P. A calibration method for quantitative BOLD fMRI based on hyperoxia. *NeuroImage* 2007;37(3):808-820.
89. Bulte DP, Chiarelli PA, Wise RG, Jezzard P. Cerebral perfusion response to hyperoxia. *Journal of cerebral blood flow and metabolism : official journal of the International Society of Cerebral Blood Flow and Metabolism* 2007;27(1):69-75.
90. Bulte DP, Kelly M, Germuska M, Xie J, Chappell MA, Okell TW, Bright MG, Jezzard P. Quantitative measurement of cerebral physiology using respiratory-calibrated MRI. *NeuroImage* 2012;60(1):582-591.
91. Gauthier CJ, Hoge RD. A generalized procedure for calibrated MRI incorporating hyperoxia and hypercapnia. *Hum Brain Mapp* 2013;34(5):1053-1069.

92. An HY, Lin WL. Quantitative measurements of cerebral blood oxygen saturation using magnetic resonance imaging. *J Cerebr Blood F Met* 2000;20(8):1225-1236.
93. Lee JM, Vo KD, An H, Celik A, Lee Y, Hsu CY, Lin W. Magnetic resonance cerebral metabolic rate of oxygen utilization in hyperacute stroke patients. *Ann Neurol* 2003;53(2):227-232.
94. Christen T, Pannetier NA, Ni WW, Qiu D, Moseley ME, Schuff N, Zaharchuk G. MR vascular fingerprinting: A new approach to compute cerebral blood volume, mean vessel radius, and oxygenation maps in the human brain. *Neuroimage* 2014;89:262-270.
95. Ma D, Gulani V, Seiberlich N, Liu K, Sunshine JL, Duerk JL, Griswold MA. Magnetic resonance fingerprinting. *Nature* 2013;495(7440):187-192.
96. Oja JM, Gillen JS, Kauppinen RA, Kraut M, van Zijl PC. Determination of oxygen extraction ratios by magnetic resonance imaging. *Journal of cerebral blood flow and metabolism : official journal of the International Society of Cerebral Blood Flow and Metabolism* 1999;19(12):1289-1295.
97. van Zijl PC, Eleff SM, Ulatowski JA, Oja JM, Ulug AM, Traystman RJ, Kauppinen RA. Quantitative assessment of blood flow, blood volume and blood oxygenation effects in functional magnetic resonance imaging. *Nat Med* 1998;4(2):159-167.
98. Wright GA, Hu BS, Macovski A. Estimating oxygen saturation of blood in vivo with MR imaging at 1.5 T. *Journal of Magnetic Resonance Imaging* 1991;1(3):275-283.
99. Golay X, Silvennoinen MJ, Zhou J, Clingman CS, Kauppinen RA, Pekar JJ, van Zijl PC. Measurement of tissue oxygen extraction ratios from venous blood T(2): increased precision and validation of principle. *Magnetic resonance in medicine : official journal of the Society of Magnetic Resonance in Medicine / Society of Magnetic Resonance in Medicine* 2001;46(2):282-291.
100. Lu H, Xu F, Grgac K, Liu P, Qin Q, van Zijl P. Calibration and validation of TRUST MRI for the estimation of cerebral blood oxygenation. *Magnetic resonance in medicine : official journal of the Society of Magnetic Resonance in Medicine / Society of Magnetic Resonance in Medicine* 2012;67(1):42-49.
101. Xu F, Ge Y, Lu H. Noninvasive quantification of whole-brain cerebral metabolic rate of oxygen (CMRO₂) by MRI. *Magnetic resonance in medicine : official journal of the Society of Magnetic Resonance in Medicine / Society of Magnetic Resonance in Medicine* 2009;62(1):141-148.
102. Xu F, Uh J, Liu P, Lu H. On improving the speed and reliability of T2-relaxation-under-spin-tagging (TRUST) MRI. *Magnetic resonance in medicine : official journal of the Society of Magnetic Resonance in Medicine / Society of Magnetic Resonance in Medicine* 2012;68(1):198-204.
103. Liu P, Xu F, Lu H. Test-retest reproducibility of a rapid method to measure brain oxygen metabolism. *Magnetic resonance in medicine : official journal of the Society of Magnetic Resonance in Medicine / Society of Magnetic Resonance in Medicine* 2013;69(3):675-681.
104. Liu P, Dimitrov I, Andrews T, Crane DE, Dariotis JK, Desmond J, Dumas J, Gilbert G, Kumar A, MacIntosh BJ, Tucholka A, Yang S, Xiao G, Lu H. Multisite evaluations of a T₂-relaxation-under-spin-tagging (TRUST) MRI technique to measure brain oxygenation. *Magnetic resonance in medicine : official journal of the Society of Magnetic Resonance in Medicine / Society of Magnetic Resonance in Medicine* 2015.

105. Xu F, Liu P, Pascual JM, Xiao G, Lu H. Effect of hypoxia and hyperoxia on cerebral blood flow, blood oxygenation, and oxidative metabolism. *Journal of cerebral blood flow and metabolism : official journal of the International Society of Cerebral Blood Flow and Metabolism* 2012;32(10):1909-1918.
106. Xu F, Liu P, Pekar JJ, Lu H. Does acute caffeine ingestion alter brain metabolism in young adults? *Neuroimage* 2015;110:39-47.
107. Chapman SB, Aslan S, Spence JS, Defina LF, Keebler MW, Didehbani N, Lu H. Shorter term aerobic exercise improves brain, cognition, and cardiovascular fitness in aging. *Front Aging Neurosci* 2013;5:75.
108. Chapman SB, Aslan S, Spence JS, Hart JJ, Jr., Bartz EK, Didehbani N, Keebler MW, Gardner CM, Strain JF, DeFina LF, Lu H. Neural mechanisms of brain plasticity with complex cognitive training in healthy seniors. *Cereb Cortex* 2015;25(2):396-405.
109. Liu P, Huang H, Rollins N, Chalak LF, Jeon T, Halovanic C, Lu H. Quantitative assessment of global cerebral metabolic rate of oxygen (CMRO₂) in neonates using MRI. *NMR Biomed* 2014;27(3):332-340.
110. Peng SL, Dumas JA, Park DC, Liu P, Filbey FM, McAdams CJ, Pinkham AE, Adinoff B, Zhang R, Lu H. Age-related increase of resting metabolic rate in the human brain. *Neuroimage* 2014;98:176-183.
111. Ge Y, Zhang Z, Lu H, Tang L, Jaggi H, Herbert J, Babb JS, Rusinek H, Grossman RI. Characterizing brain oxygen metabolism in patients with multiple sclerosis with T2-relaxation-under-spin-tagging MRI. *Journal of cerebral blood flow and metabolism : official journal of the International Society of Cerebral Blood Flow and Metabolism* 2012;32(3):403-412.
112. Liu J, Zhu YS, Khan MA, Brunk E, Martin-Cook K, Weiner MF, Cullum CM, Lu H, Levine BD, Diaz-Arrastia R, Zhang R. Global brain hypoperfusion and oxygenation in amnesic mild cognitive impairment. *Alzheimer's & dementia : the journal of the Alzheimer's Association* 2014;10(2):162-170.
113. Wong E, Guo J. VENTI: Venous Territory Imaging using Remote Sensing. 2013; Salt Lake City, Utah. ISMRM. p 0103.
114. Wong EC, Cronin M, Wu WC, Inglis B, Frank LR, Liu TT. Velocity-selective arterial spin labeling. *Magnetic resonance in medicine : official journal of the Society of Magnetic Resonance in Medicine / Society of Magnetic Resonance in Medicine* 2006;55(6):1334-1341.
115. Cerdonio M, Morante S, Vitale S. Magnetic susceptibility of hemoglobins. *Methods Enzymol* 1981;76:354-371.
116. Spees WM, Yablonskiy DA, Oswood MC, Ackerman JJ. Water proton MR properties of human blood at 1.5 Tesla: magnetic susceptibility, T(1), T(2), T*(2), and non-Lorentzian signal behavior. *Magnetic resonance in medicine : official journal of the Society of Magnetic Resonance in Medicine / Society of Magnetic Resonance in Medicine* 2001;45(4):533-542.
117. Yablonskiy DA. Cerebral metabolic rate in hypercapnia: controversy continues. *Journal of cerebral blood flow and metabolism : official journal of the International Society of Cerebral Blood Flow and Metabolism* 2011;31(7):1502-1503.
118. Jain V, Abdulmalik O, Probert KJ, Wehrli FW. Investigating the magnetic susceptibility properties of fresh human blood for noninvasive oxygen saturation quantification. *Magnetic resonance in medicine : official journal of the Society of Magnetic Resonance in Medicine / Society of Magnetic Resonance in Medicine* 2012;68(3):863-867.

119. Li L, Leigh JS. Quantifying arbitrary magnetic susceptibility distributions with MR. *Magnetic resonance in medicine : official journal of the Society of Magnetic Resonance in Medicine / Society of Magnetic Resonance in Medicine* 2004;51(5):1077-1082.
120. Wang Y, Liu T. Quantitative susceptibility mapping (QSM): Decoding MRI data for a tissue magnetic biomarker. *Magnetic resonance in medicine : official journal of the Society of Magnetic Resonance in Medicine / Society of Magnetic Resonance in Medicine* 2014.
121. Fernández-Seara MA, Techawiboonwong A, Detre JA, Wehrli FW. MR susceptometry for measuring global brain oxygen extraction. *Magnetic resonance in medicine* 2006;55(5):967-973.
122. Haacke EM, Lai S, Reichenbach JR, Kuppusamy K, Hoogenraad FG, Takeichi H, Lin W. In vivo measurement of blood oxygen saturation using magnetic resonance imaging: a direct validation of the blood oxygen level-dependent concept in functional brain imaging. *Human brain mapping* 1997;5(5):341-346.
123. Li C, Langham MC, Epstein CL, Magland JF, Wu J, Gee J, Wehrli FW. Accuracy of the cylinder approximation for susceptometric measurement of intravascular oxygen saturation. *Magnetic resonance in medicine : official journal of the Society of Magnetic Resonance in Medicine / Society of Magnetic Resonance in Medicine* 2012;67(3):808-813.
124. Jain V, Langham MC, Floyd TF, Jain G, Magland JF, Wehrli FW. Rapid magnetic resonance measurement of global cerebral metabolic rate of oxygen consumption in humans during rest and hypercapnia. *Journal of cerebral blood flow and metabolism : official journal of the International Society of Cerebral Blood Flow and Metabolism* 2011;31(7):1504-1512.
125. Jain V, Buckley EM, Licht DJ, Lynch JM, Schwab PJ, Naim MY, Lavin NA, Nicolson SC, Montenegro LM, Yodh AG, Wehrli FW. Cerebral oxygen metabolism in neonates with congenital heart disease quantified by MRI and optics. *Journal of cerebral blood flow and metabolism : official journal of the International Society of Cerebral Blood Flow and Metabolism* 2014;34(3):380-388.
126. Langham MC, Magland JF, Floyd TF, Wehrli FW. Retrospective correction for induced magnetic field inhomogeneity in measurements of large-vessel hemoglobin oxygen saturation by MR susceptometry. *Magnetic resonance in medicine : official journal of the Society of Magnetic Resonance in Medicine / Society of Magnetic Resonance in Medicine* 2009;61(3):626-633.
127. Borghammer P, Chakravarty M, Jonsdottir KY, Sato N, Matsuda H, Ito K, Arahata Y, Kato T, Gjedde A. Cortical hypometabolism and hypoperfusion in Parkinson's disease is extensive: probably even at early disease stages. *Brain Struct Funct* 2010;214(4):303-317.
128. Fan AP, Benner T, Bolar DS, Rosen BR, Adalsteinsson E. Phase-based regional oxygen metabolism (PROM) using MRI. *Magnetic resonance in medicine : official journal of the Society of Magnetic Resonance in Medicine / Society of Magnetic Resonance in Medicine* 2012;67(3):669-678.
129. Thomason ME, Foland LC, Glover GH. Calibration of BOLD fMRI using breath holding reduces group variance during a cognitive task. *Human brain mapping* 2007;28(1):59-68.
130. Van Zijl PC, Hua J, Lu H. The BOLD post-stimulus undershoot, one of the most debated issues in fMRI. *NeuroImage* 2012;62(2):1092-1102.

131. Ainslie PN, Ogoh S. Regulation of cerebral blood flow in mammals during chronic hypoxia: a matter of balance. *Experimental Physiology* 2010;95(2):251-262.
132. Duchna HW, Guilleminault C, Stoohs RA, Faul JL, Moreno H, Hoffman BB, Blaschke TF. Vascular reactivity in obstructive sleep apnea syndrome. *American journal of respiratory and critical care medicine* 2000;161(1):187-191.
133. Virtanen J, Nojonen T, Salmi T, Toppila J, Meriläinen P. Impaired cerebral vasoreactivity may cause cerebral blood volume dip following obstructive sleep apnea termination. *Sleep and breathing* 2011;16(2):309-312.
134. Mugler JP, Brookeman JR. Three-dimensional magnetization-prepared rapid gradient-echo imaging (3D MP RAGE). *Magnetic Resonance in Medicine* 1990;15(1):152-157.
135. Rodgers ZB, Jain V, Englund EK, Langham MC, Wehrli FW. High temporal resolution MRI quantification of global cerebral metabolic rate of oxygen consumption in response to apneic challenge. *Journal of cerebral blood flow and metabolism : official journal of the International Society of Cerebral Blood Flow and Metabolism* 2013;33(10):1514-1522.
136. Van Vaals JJ, Brummer ME, Thomas Dixon W, Tuithof HH, Engels H, Nelson RC, Gerety BM, Chezmar JL, Den Boer JA. "Keyhole" method for accelerating imaging of contrast agent uptake. *Journal of Magnetic Resonance Imaging* 1993;3(4):671-675.
137. Goode RC, Brown EB, Howson MG, Cunningham DJ. Respiratory effects of breathing down a tube. *Respiration physiology* 1969;6(3):343-359.
138. Denison D. CHAPTER 5 - High Altitudes and Hypoxia. In: Weiner OGES, editor. *The Principles and Practice of Human Physiology*: Academic Press; 1981. p 241-307.
139. Yushkevich PA, Piven J, Hazlett HC, Smith RG, Ho S, Gee JC, Gerig G. User-guided 3D active contour segmentation of anatomical structures: significantly improved efficiency and reliability. *NeuroImage* 2006;31(3):1116-1128.
140. Hua J, Stevens RD, Huang AJ, Pekar JJ, van Zijl PCM. Physiological origin for the BOLD poststimulus undershoot in human brain: vascular compliance versus oxygen metabolism. *J Cerebr Blood F Met* 2011;31(7):1599-1611.
141. Chen JJ, Pike GB. Global cerebral oxidative metabolism during hypercapnia and hypocapnia in humans: implications for BOLD fMRI. *Journal of cerebral blood flow and metabolism : official journal of the International Society of Cerebral Blood Flow and Metabolism* 2010;30(6):1094-1099.
142. Mehta NR, Jones L, Kraut MA, Melhem ER. Physiologic variations in dural venous sinus flow on phase-contrast MR imaging. *AJR American journal of roentgenology* 2000;175(1):221-225.
143. Lee SP, Duong TQ, Yang G, Iadecola C, Kim SG. Relative changes of cerebral arterial and venous blood volumes during increased cerebral blood flow: implications for BOLD fMRI. *Magnetic resonance in medicine : official journal of the Society of Magnetic Resonance in Medicine / Society of Magnetic Resonance in Medicine* 2001;45(5):791-800.
144. Blockley NP, Griffeth VE, Germuska MA, Bulte DP, Buxton RB. An analysis of the use of hyperoxia for measuring venous cerebral blood volume: comparison of the existing method with a new analysis approach. *Neuroimage* 2013;72:33-40.
145. Duong TQ, Iadecola C, Kim SG. Effect of hyperoxia, hypercapnia, and hypoxia on cerebral interstitial oxygen tension and cerebral blood flow. *Magnetic*

- resonance in medicine : official journal of the Society of Magnetic Resonance in Medicine / Society of Magnetic Resonance in Medicine 2001;45(1):61-70.
146. Nicholson C, Phillips JM. Ion diffusion modified by tortuosity and volume fraction in the extracellular microenvironment of the rat cerebellum. *J Physiol* 1981;321:225-257.
 147. Kennealy JA, Karl AA, Kirkland JS. Cerebral blood flow autoregulation: effect of hypercapnia on cerebral tissue gas concentrations. *J Surg Res* 1978;24(3):150-153.
 148. Kim SG, Ogawa S. Biophysical and physiological origins of blood oxygenation level-dependent fMRI signals. *Journal of cerebral blood flow and metabolism : official journal of the International Society of Cerebral Blood Flow and Metabolism* 2012;32(7):1188-1206.
 149. Matthews PM, Honey GD, Bullmore ET. Applications of fMRI in translational medicine and clinical practice. *Nature reviews Neuroscience* 2006;7(9):732-744.
 150. Blockley NP, Griffeth VE, Simon AB, Buxton RB. A review of calibrated blood oxygenation level-dependent (BOLD) methods for the measurement of task-induced changes in brain oxygen metabolism. *NMR Biomed* 2013;26(8):987-1003.
 151. Qin Q, Grgac K, van Zijl PC. Determination of whole-brain oxygen extraction fractions by fast measurement of blood T(2) in the jugular vein. *Magnetic resonance in medicine : official journal of the Society of Magnetic Resonance in Medicine / Society of Magnetic Resonance in Medicine* 2011;65(2):471-479.
 152. Chen JJ, Pike GB. Human whole blood T2 relaxometry at 3 Tesla. *Magnetic resonance in medicine : official journal of the Society of Magnetic Resonance in Medicine / Society of Magnetic Resonance in Medicine* 2009;61(2):249-254.
 153. Barhoum S, Rodgers ZB, Langham M, Magland JF, Li C, Wehrli FW. Comparison of MRI methods for measuring whole-brain venous oxygen saturation. *Magnetic resonance in medicine : official journal of the Society of Magnetic Resonance in Medicine / Society of Magnetic Resonance in Medicine* 2015;73(6):2122-2128.
 154. Doyle M, Walsh EG, Blackwell GG, Pohost GM. Block regional interpolation scheme for k-space (BRISK): a rapid cardiac imaging technique. *Magnetic resonance in medicine : official journal of the Society of Magnetic Resonance in Medicine / Society of Magnetic Resonance in Medicine* 1995;33(2):163-170.
 155. Rodgers Z, Kini L, Jain V, Langham M, Magland JF, Wehrli FW. High temporal resolution, simultaneous quantification of intravascular blood flow and oxygen saturation with BRISK k-space sampling. 2013; Salt Lake City, Utah. ISMRM. p 1351.
 156. Magland JF, Li C, Langham MC, Wehrli FW. Pulse sequence programming in a dynamic visual environment: SequenceTree. *Magnetic resonance in medicine : official journal of the Society of Magnetic Resonance in Medicine / Society of Magnetic Resonance in Medicine* 2015.
 157. Smith SM. Fast robust automated brain extraction. *Hum Brain Mapp* 2002;17(3):143-155.
 158. Herscovitch P, Raichle ME. What is the correct value for the brain--blood partition coefficient for water? *Journal of cerebral blood flow and metabolism : official journal of the International Society of Cerebral Blood Flow and Metabolism* 1985;5(1):65-69.

159. Krishnamurthy LC, Liu P, Xu F, Uh J, Dimitrov I, Lu H. Dependence of blood T(2) on oxygenation at 7 T: in vitro calibration and in vivo application. *Magnetic resonance in medicine : official journal of the Society of Magnetic Resonance in Medicine / Society of Magnetic Resonance in Medicine* 2014;71(6):2035-2042.
160. Xu B, Liu T, Spincemaille P, Prince M, Wang Y. Flow compensated quantitative susceptibility mapping for venous oxygenation imaging. *Magnetic resonance in medicine : official journal of the Society of Magnetic Resonance in Medicine / Society of Magnetic Resonance in Medicine* 2014;72(2):438-445.
161. Gardener AG, Francis ST, Prior M, Peters A, Gowland PA. Dependence of blood R2 relaxivity on CPMG echo-spacing at 2.35 and 7 T. *Magnetic resonance in medicine : official journal of the Society of Magnetic Resonance in Medicine / Society of Magnetic Resonance in Medicine* 2010;64(4):967-974.
162. Gupta A, Chazen JL, Hartman M, Delgado D, Anumula N, Shao H, Mazumdar M, Segal AZ, Kamel H, Leifer D, Sanelli PC. Cerebrovascular reserve and stroke risk in patients with carotid stenosis or occlusion: a systematic review and meta-analysis. *Stroke; a journal of cerebral circulation* 2012;43(11):2884-2891.
163. Richiardi J, Monsch AU, Haas T, Barkhof F, Van de Ville D, Radu EW, Kressig RW, Haller S. Altered cerebrovascular reactivity velocity in mild cognitive impairment and Alzheimer's disease. *Neurobiology of aging* 2015;36(1):33-41.
164. Englund EK, Langham MC, Li C, Rodgers ZB, Floyd TF, Mohler ER, Wehrli FW. Combined measurement of perfusion, venous oxygen saturation, and skeletal muscle T2* during reactive hyperemia in the leg. *J Cardiovasc Magn Reson* 2013;15:70.
165. Driver ID, Hall EL, Wharton SJ, Pritchard SE, Francis ST, Gowland PA. Calibrated BOLD using direct measurement of changes in venous oxygenation. *Neuroimage* 2012;63(3):1178-1187.
166. Schmithorst VJ, Hernandez-Garcia L, Vannest J, Rajagopal A, Lee G, Holland SK. Optimized simultaneous ASL and BOLD functional imaging of the whole brain. *J Magn Reson Imaging* 2014;39(5):1104-1117.
167. Gusnard DA, Raichle ME, Raichle ME. Searching for a baseline: functional imaging and the resting human brain. *Nature reviews Neuroscience* 2001;2(10):685-694.
168. Aslan S, Xu F, Wang PL, Uh J, Yezhuvath US, van Osch M, Lu H. Estimation of labeling efficiency in pseudocontinuous arterial spin labeling. *Magnetic resonance in medicine : official journal of the Society of Magnetic Resonance in Medicine / Society of Magnetic Resonance in Medicine* 2010;63(3):765-771.
169. Dai W, Garcia D, de Bazelaire C, Alsop DC. Continuous flow-driven inversion for arterial spin labeling using pulsed radio frequency and gradient fields. *Magnetic resonance in medicine : official journal of the Society of Magnetic Resonance in Medicine / Society of Magnetic Resonance in Medicine* 2008;60(6):1488-1497.
170. Alsop DC, Detre JA, Golay X, Gunther M, Hendrikse J, Hernandez-Garcia L, Lu H, Macintosh BJ, Parkes LM, Smits M, van Osch MJ, Wang DJ, Wong EC, Zaharchuk G. Recommended implementation of arterial spin-labeled perfusion MRI for clinical applications: A consensus of the ISMRM perfusion study group and the European consortium for ASL in dementia. *Magnetic resonance in medicine : official journal of the Society of Magnetic Resonance in Medicine / Society of Magnetic Resonance in Medicine* 2014.
171. Buxton RB, Frank LR, Wong EC, Siewert B, Warach S, Edelman RR. A general kinetic model for quantitative perfusion imaging with arterial spin labeling.

- Magnetic resonance in medicine : official journal of the Society of Magnetic Resonance in Medicine / Society of Magnetic Resonance in Medicine 1998;40(3):383-396.
172. Pilkinton DT, Gaddam SR, Reddy R. Characterization of paramagnetic effects of molecular oxygen on blood oxygenation level-dependent-modulated hyperoxic contrast studies of the human brain. *Magnetic resonance in medicine : official journal of the Society of Magnetic Resonance in Medicine / Society of Magnetic Resonance in Medicine* 2011;66(3):794-801.
 173. Lu H, Zhao C, Ge Y, Lewis-Amezcu K. Baseline blood oxygenation modulates response amplitude: Physiologic basis for intersubject variations in functional MRI signals. *Magnetic resonance in medicine : official journal of the Society of Magnetic Resonance in Medicine / Society of Magnetic Resonance in Medicine* 2008;60(2):364-372.
 174. Hare HV, Blockley NP, Gardener AG, Clare S, Bulte DP. Investigating the field-dependence of the Davis model: Calibrated fMRI at 1.5, 3 and 7T. *Neuroimage* 2015;112:189-196.
 175. Blockley NP, Griffeth VE, Buxton RB. A general analysis of calibrated BOLD methodology for measuring CMRO₂ responses: comparison of a new approach with existing methods. *Neuroimage* 2012;60(1):279-289.
 176. Kastrup A, Kruger G, Glover GH, Moseley ME. Assessment of cerebral oxidative metabolism with breath holding and fMRI. *Magnetic resonance in medicine : official journal of the Society of Magnetic Resonance in Medicine / Society of Magnetic Resonance in Medicine* 1999;42(3):608-611.
 177. Wise RG, Harris AD, Stone AJ, Murphy K. Measurement of OEF and absolute CMRO₂: MRI-based methods using interleaved and combined hypercapnia and hyperoxia. *Neuroimage* 2013;83:135-147.
 178. Somers VK, White DP, Amin R, Abraham WT, Costa F, Culebras A, Daniels S, Floras JS, Hunt CE, Olson LJ, Pickering TG, Russell R, Woo M, Young T. Sleep apnea and cardiovascular disease: an American Heart Association/American College of Cardiology Foundation Scientific Statement from the American Heart Association Council for High Blood Pressure Research Professional Education Committee, Council on Clinical Cardiology, Stroke Council, and Council on Cardiovascular Nursing. *J Am Coll Cardiol* 2008;52(8):686-717.
 179. Pack AI, Gislason T. Obstructive sleep apnea and cardiovascular disease: a perspective and future directions. *Prog Cardiovasc Dis* 2009;51(5):434-451.
 180. Kushida CA, Nichols DA, Quan SF, Goodwin JL, White DP, Gottlieb DJ, Walsh JK, Schweitzer PK, Guilleminault C, Simon RD, Leary EB, Hyde PR, Holmes TH, Bloch DA, Green S, McEvoy LK, Gevins A, Dement WC. The Apnea Positive Pressure Long-term Efficacy Study (APPLES): rationale, design, methods, and procedures. *J Clin Sleep Med* 2006;2(3):288-300.
 181. Macey PM, Kumar R, Woo MA, Valladares EM, Yan-Go FL, Harper RM. Brain structural changes in obstructive sleep apnea. *Sleep* 2008;31(7):967-977.
 182. Globus MY, Busto R, Martinez E, Valdes I, Dietrich WD, Ginsberg MD. Comparative effect of transient global ischemia on extracellular levels of glutamate, glycine, and gamma-aminobutyric acid in vulnerable and nonvulnerable brain regions in the rat. *J Neurochem* 1991;57(2):470-478.
 183. Gooden BA. Mechanism of the human diving response. *Integr Physiol Behav Sci* 1994;29(1):6-16.

184. Macey PM, Kumar R, Ogren JA, Woo MA, Harper RM. Global brain blood-oxygen level responses to autonomic challenges in obstructive sleep apnea. *PloS one* 2014;9(8):e105261.
185. Urbano F, Roux F, Schindler J, Mohsenin V. Impaired cerebral autoregulation in obstructive sleep apnea. *Journal of Applied Physiology* 2008;105(6):1852-1857.
186. Lefebvre B, Godin-Ribuot D, Joyeux-Faure M, Caron F, Bessard G, Lévy P, Stanke-Labesque F. Functional assessment of vascular reactivity after chronic intermittent hypoxia in the rat. *Respiratory physiology & neurobiology* 2006;150(2-3):278-286.
187. Foster GE, Hanly PJ, Ostrowski M, Poulin MJ. Ventilatory and cerebrovascular responses to hypercapnia in patients with obstructive sleep apnoea: effect of CPAP therapy. *Respiratory physiology & neurobiology* 2009;165(1):73-81.
188. Thevenaz P, Ruttimann UE, Unser M. A pyramid approach to subpixel registration based on intensity. *IEEE transactions on image processing : a publication of the IEEE Signal Processing Society* 1998;7(1):27-41.
189. Foster GE, Brugniaux JV, Pialoux V, Duggan CTC, Hanly PJ, Ahmed SB, Poulin MJ. Cardiovascular and cerebrovascular responses to acute hypoxia following exposure to intermittent hypoxia in healthy humans. *J Physiol (Lond)* 2009;587(Pt 13):3287-3299.
190. Thomason ME, Glover GH. Controlled inspiration depth reduces variance in breath-holding-induced BOLD signal. *Neuroimage* 2008;39(1):206-214.
191. Shin LK, Holbrook AB, Capasso R, Kushida CA, Powell NB, Fischbein NJ, Pauly KB. Improved sleep MRI at 3 tesla in patients with obstructive sleep apnea. *J Magn Reson Imaging* 2013;38(5):1261-1266.
192. Thomas BP, Sheng M, Tseng B, Liu P, Martin-Cook K, Cullum M, Weiner M, Levine B, Zhang R, Lu H. Characterization of CMRO₂, resting CBF, and cerebrovascular reactivity in patients with very early stage of Alzheimer's Disease. 2013; Salt Lake City, Utah. *ISMRM*. p 0619.
193. Lustig M, Donoho D, Pauly JM. Sparse MRI: The application of compressed sensing for rapid MR imaging. *Magnetic resonance in medicine : official journal of the Society of Magnetic Resonance in Medicine / Society of Magnetic Resonance in Medicine* 2007;58(6):1182-1195.
194. Driver ID, Wharton SJ, Croal PL, Bowtell R, Francis ST, Gowland PA. Global intravascular and local hyperoxia contrast phase-based blood oxygenation measurements. *Neuroimage* 2014;101:458-465.
195. Salomir R, de Senneville BD, Moonen CT. A fast calculation method for magnetic field inhomogeneity due to an arbitrary distribution of bulk susceptibility. *Concepts Magn Reson*. Volume 19: Wiley Online Library; 2003. p 26-34.
196. Fernandez-Seara MA, Wang Z, Wang J, Rao HY, Guenther M, Feinberg DA, Detre JA. Continuous arterial spin labeling perfusion measurements using single shot 3D GRASE at 3 T. *Magnetic resonance in medicine : official journal of the Society of Magnetic Resonance in Medicine / Society of Magnetic Resonance in Medicine* 2005;54(5):1241-1247.